UNIVERSITY OF PADOVA

Faculty of Engineering

Master Degree Course in Product Innovation Engineering

Master Thesis

DAMAGE ANALYSIS ON COMPOSITE LAMINATES UNDER FATIGUE LOADING

Supervisor: Ch.mo. Prof. Marino Quaresimin

Co-Supervisor: Prof. Povl Brøndsted

Graduand: Luigi Vivian

Academic Year 2010-2011

SUMMARY

Planar glass-epoxy samples with lay-up $[0/(+60)_2/0/(-60)_2]_s$ were considered for a damage analysis under uniaxial fatigue loading. The attention is given on the off-axis layers where a multiaxial local stress state exists with biaxiality ratio λ_{12} equal to 0.5. The experimental fatigue tests were conducted by varying the strain level applied and monitoring the crack evolution through an automatic system of images acquisition.

The fatigue tests results show that after a certain number of cycles the crack density reaches a saturation condition constant to failure; the values of this saturation raise as the strain level applied increases. At the same time the sample's stiffness decays until a constant value in which the off-axis layers are totally cracked and only the 0° layers carry the load. The off-axis layers (+60° and -60°) have a different behavior in terms of crack density, this means that the thickness has a significant effects. In particular the two layers at +60° have a double crack density value with respect to the four layers at -60° in each strain level. Moreover, the crack propagation rate observed during the experimental tests is different between the off-axis layer and depends on the strain level applied; in fact the -60° layers show in general an instantaneous propagation, instead in the +60° layers cracks need several cycles to propagate through the entire sample's width.

The damage analysis, developed by several ABAQUS simulations and based on the theoretical model of Hutchinson and Suo (1), allowed to find a relation between the normalized crack spacing and the steady-state energy release rate. Through this results the Paris type curve of the off-axis layers was constructed and finding no significant differences between these layers. After, a prediction of the crack density evolution was done in spite the theoretical model (1) was developed for cracks under pure mode I and for isotropic material. Comparing with the experimental results, the prediction works well only for low number of cycles because a more accurate calibration of the model must be done in order to obtain a correct crack density prediction. However, the reliability of the developed prediction model has been verified through a comparison of the crack propagation rate with the experimental results, finding almost a fully agreement.

The crack density trends obtained from the experimental tests were used to do a comparison with results of the project on tubular samples $[0_T/90_{ud,3}]$ (2) that considers a global multiaxial stress state. This comparison could determine if the damage evolution is comparable between a local and a global multiaxial condition with the same biaxialitiy ratio. The results showed how a comparison in terms of crack density is not possible because of there are different constraint conditions on off-axis layers between flat and tubular samples that provide a different material strength and consequently a different damaging mode. These observations allowed asserting that it is not possible to replicate the damage evolution under a global multiaxial condition through a local multiaxial condition considering tubular and flat samples respectively.

PREFACE

This work represents a Master thesis carried out within the ERASMUS project for the Product Innovation Engineering Degree in Padova University (Italy). The research activity has been carried out at the Materials Research Division, Risoe National Laboratory for Sustainable Energy, Technical University of Denmark. The composite material used for tests was supplied by the Department of Management and Engineering (DTG) in Italy thanks to a collaboration between the University of Padova and DTU.

The period of the Master thesis study has been lasting for 6 months, since August 2010 until January 2011.

The study has been supervised by:

Senior Scientist, Ph.D., Povl Brøndsted	Main supervisor
Senior Scientist, Ph.D., Bent F. Sørensen	Co-supervisor
Senior Scientist, Ph.D., Lars Pilgaard Mikkelsen	Co-supervisor

The activity has been also supervised by the Professor Marino Quaresimin at DTG, University of Padova.

I wish to thank my supervisors for the support given during the study period and for the opportunity of using professional equipment in the laboratories.
I would like to acknowledge Tom Løgstrup Andersen for the helping in the samples preparation, the technician Eric Vogeley for the assistance during the fatigue tests and the images analysis and the other technicians Frank Adrian and Vagn Jensen for the support with the mechanical tests.
Furthermore, I want to make a sincere thanks to my parents for the supporting during the whole university study period.

CONTENTS

1 INTRODUCTION

This work is focused on damage analysis of angle-ply composite laminates subjected to uniaxial fatigue load. The attention is given to the local multiaxial stress field (along the fibers direction) which is generated in the material and that is due to the orthotropic behaviour. In composite materials, especially under fatigue loading, is common the presence of a multiple cracking condition; for this reason in order to evaluate the damage evolution it is very useful to consider the crack density as controlling parameter. Generally, in practical applications the presence of cracks can be accepted and doesn't replace the component in operation. In particular, the material stiffness decays with increasing the number of damages, thus in presence of few cracks the material performances may still be sufficient for the component to perform its function. Therefore, it is important to understand how damage evolves and what its effects on the decay material properties are.

Generally speaking, a multiaxial stress state corresponds to a condition where more than one of the all plane stress components is present in the material. This aspect complicates the analysis because it must to consider all the effects generated by all stress components; in fact the fatigue behaviour of composite laminates under uniaxial loading condition is known in technical literature, instead the multiaxial condition is not completely investigated.

The analysis presented in this work is a continuation of a previous thesis project (2) which analysed the fatigue damaging on tubular samples under an external multiaxial loading condition. In particular the geometry of the specimens leads to apply a tension-torsion combined load controlling the ratio between the load components. In a secondary step, after the analysis of flat laminates, what matters is to compare the fatigue damage evolution between the planar samples (local multiaxial stress state) and the tubular samples (global multiaxial stress state), in order to evaluate if there is the same behaviour. If so, it would be possible to know the effects of multiaxial cyclic load studying only the corresponding case with uniaxial cyclic load that is much easier to test and to simulate. This comparison can be done considering the same biaxiality ratios (shear stress over normal stress) and the same material for tubular and planar samples. For this reason, the starting point of this work is to replicate the biaxiality ratios used with the tubular specimens and considering the same material: glass fibres and epoxy matrix. After the complete damage analysis of planar samples the results comparison between flat and tubular samples is presented.

2 BACKGROUND

2.1 GENERALITY

This chapter describes briefly the main parameters used in the present project to analyse the multiaxial fatigue behaviour of composite materials. In particular, the attention is given to the parameters useful to consider a multiaxial stress condition.

Generally, in a composite laminate two systems of reference can be determined, see Figure 2-1. For a plane case the axes X, Y correspond to the structure orientation (global system), instead the axes 1, 2 correspond to the fibers orientation (local system) that is rotated by the off-axis angle θ.

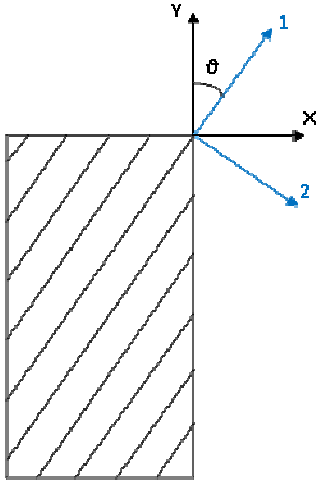

Figure 2-1. Local and global systems reference in a composite lamina

In composite materials with fibers orientated along an off-axis angle θ, a multiaxial stress field is always present regardless the applied external load. In fact the orthotropic behaviour of the materials leads to obtain along the fibres direction a multiaxial stress state even with a uniaxial external load. This is due to the intrinsic behaviour of composite material where the external load is reduced to the local stress state through the rotation matrix T, that is determine with respect to θ; see Equation 2.1. Consequently, even with only an external σ_y applied the corresponding local stress state is in a multiaxial condition. Therefore the off-axis angle, along which the fibers are arranged, has a primary role because with the same external applied load produces a different local stress states depending on the laminate orientation.

$$\sigma_1 = cos^2(\vartheta) \cdot \sigma_x + sin^2(\vartheta) \cdot \sigma_y + 2\cos(\vartheta)\sin(\vartheta) \cdot \tau_{xy}$$

$$\sigma_2 = sin^2(\vartheta) \cdot \sigma_x + cos^2(\vartheta) \cdot \sigma_y - 2\cos(\vartheta)\sin(\vartheta) \cdot \tau_{xy} \qquad 2.1$$

$$\tau_{12} = -\cos(\vartheta)\sin(\vartheta) \cdot \sigma_x + \cos(\vartheta)\sin(\vartheta) \cdot \sigma_y + \left(cos^2(\vartheta) - sin^2(\vartheta)\right) \cdot \tau_{xy}$$

2.2 DEFINITION OF USED PARAMETERS

Firstly, to study the multiaxial fatigue problem in composite material, it is important to give the definitions of the quantities used in the stress analysis. To do this, the sample in Figure 2-2 is considered. Laminate (global) and material (local) references are x, y, z and 1, 2, 3 respectively. In this way it is possible to express a general stress state by the two systems reference, as follows reported in 2.2 and 2.3.

$$\text{Global stress components} \rightarrow \sigma_x(t);\ \sigma_y(t);\ \tau_{xy}(t) \quad (t \in T) \qquad 2.2$$

$$\text{Local stress components} \rightarrow \sigma_1(t);\ \sigma_2(t);\ \tau_{12}(t) \quad (t \in T) \qquad 2.3$$

Where, considering the fatigue case, T is the period of the loading.

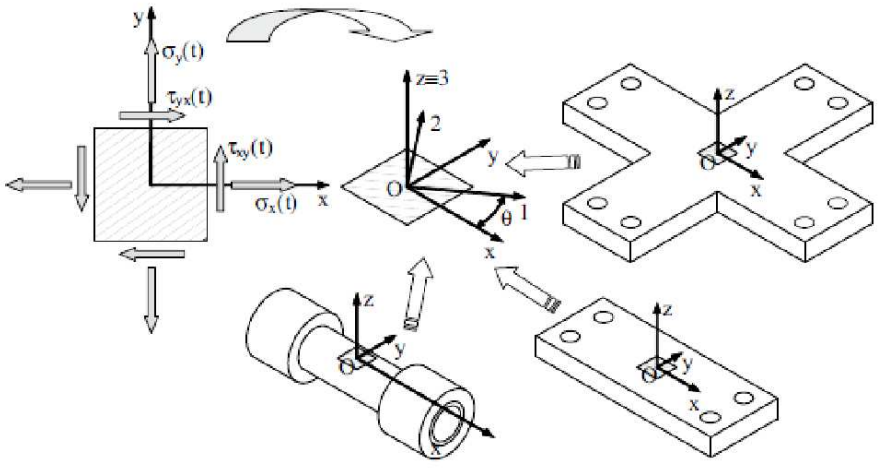

Figure 2-2. Definition of the used system references (3)

Agreeing with what was exposed by *Quaresimin-Susmel-Talreja* in (3), a multiaxial stress field can be assessed through the biaxiality ratios that are firstly determined by the amplitude of the global stress components as subsequently reported.

$$\lambda_C = \frac{\sigma_{y,a}}{\sigma_{x,a}} \qquad 2.4$$

$$\lambda_T = \frac{\tau_{xy,a}}{\sigma_{x,a}} \qquad 2.5$$

The biaxiality ratios can then be also determined by the amplitude of local stress components:

$$\lambda_1 = \frac{\sigma_{2,a}}{\sigma_{1,a}} \qquad 2.6$$

$$\lambda_2 = \frac{\sigma_{6,a}}{\sigma_{1,a}} \qquad 2.7$$

$$\lambda_{12} = \frac{\sigma_{6,a}}{\sigma_{2,a}} \qquad 2.8$$

As is known, the fatigue behavior is controlled through the local stresses; therefore in order to assess the damage evolution the local stress state must be known.

An analysis by *Quaresimin-Susmel-Talreja* in (3) was conducted in order to determine the off-axis angle influence on fatigue behavior in a multiaxial stress state condition. The attention was gave in particular to the local stress field and was found that the biaxiality ratios λ_1, λ_2, λ_{12} are a good tools to express the effects of a multiaxial stress condition; i.e. the local stress field well controls the fatigue strength. Also in Figure 2-3 the authors found that λ_1 has a negligible influence on fatigue behavior, whilst the presence of λ_2 leads a significant reduction in fatigue strength. Therefore, in a damage analysis under fatigue loading and in presence of a multiaxial local stress state, it makes sense considering only λ_2. This conclusion allows to asserting that the local shear stress components has a significant effects on the material fatigue behavior.

Moreover, *Quaresimin-Susmel-Talreja* in (3) suggested that the presence of a shear stress and a transverse stress could be a more heavy condition with respect to a combination of shear stress and longitudinal stress. Thus, it makes sense to investigate the effects of biaxiality ratio λ_{12} on fatigue behavior.

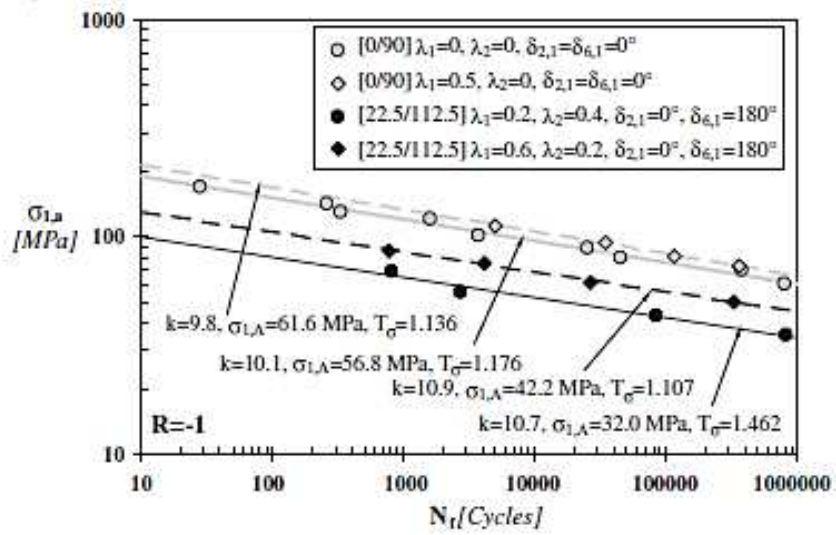

Figure 2-3. Influence of biaxiality ratios on the fatigue strength of glass/epoxy specimens subjected to tension fatigue loading (3)

3 PRELIMINARY ANALYSIS

3.1 GENERALITY

This chapter describes the preliminary analysis conducted in order to determine the correct lay-up to achieve the aims of this work. Choices are: stacking sequence and number of layers of the laminate, the off-axis angle and the material. Subsequently, the chosen laminate was analyzed by a finite elements simulation of the stress field of each layer to control the achievement of desired results.

3.2 CHOICE OF LAY-UP

The first problem considered was to understand what could be the best generic lay-up for this project. The goal is to obtain particular values of biaxiality ratios in an off-axis laminate, considering the orthotropic behavior of the material and the uniaxial cyclic loading. In this way the material is subjected only to a local multiaxial stress state. Furthermore, it must taking into account that final choice of the lay-up should facilitate the damage analysis that will be done during the fatigue tests; for example, giving a good vision of the cracks.

In this connection, a meeting was made to discuss which could be the correct lay-up; the meeting was attended by Prof. P. Brøndsted, Prof. R. Talreja and Prof. B. Soresen. The first decision was that the laminate must be symmetrical and that between the off-axis layers should be an on-axis layer to ensure the appropriate constraint conditions. The function of the on-axis layers is to generate a constant and homogeneous constraint condition on both sides of the off-axis layers, because a prerequisite for a correct analysis is that in every layer the stress state is not modified by a different constraint condition on the sides. Secondly, the symmetrical and orthotropic laminate has more advantages with respect to the no-symmetrical one in terms of decoupling between normal stress, shear sliding and curvatures (considering the Classic Lamination Theory). After a long discussion, the first possible choice of lay-up was: $[0/+\vartheta/0/-\vartheta]_S$.

To conduct a damage analysis means that during the tests cracks initiation and propagation must be observed. For this reason the next step was to increase the thickness of the off-axis layers in order to facilitate the observation of damages, because with greater thickness the cracks are larger and consequently more visible. So the lay-up was changed to: $[(0)_3/(+\vartheta)_6/(0)_3/(-\vartheta)_6]_S$. Another consideration was that with this lay-up in the laminate there are two groups of six off-axis layers and one central group of twelve off-axis layers, in the latter the first cracks propagate at low number of cycles whilst the sextuple layer is

damaged at a higher number of cycles. The reason is because the off-axis layers groups with opposite orientation have different thickness. In this way it is possible to observe two different damage phenomena of the laminate, at low and at higher number of cycles.

Considering the material choice, to be used for this project, it was compulsory the same material used in the work with tubular samples (2). The reason is that fibers and matrix produced by different industrial producer could have different properties and consequently the future comparison with the results of the tubular samples tube could be not precise. This material is the UE400-REM produced by SEAL, it is a unidirectional prepreg with glass fiber and epoxy matrix. The details of the material properties provided by the producer are reported below in Figure 3-1:

UE400 REM GLASS UD PREPREG

PREPREG PROPERTIES

Uncured Prepreg	*Unit*	*Typical Values*	
Glass Fiber	-	E glass	
Outlife @ 23°C	days	30	
Storage life @ -18°C	months	12	
Nominal Area Weight	g/m²	645	
Nominal Resin Content	Wt %	38 (± 3)	
Volatile Content	Wt %	< 1	
Flow after 15 min @125°C, 3 bar	Wt %	7 ± 5	
Cured Material Properties (*)	*Unit*	*Typical Value*	*Standard Method*
Cured ply thickness	mm	0.16	
Tensile Strenght	MPa	750	ASTM D 3039
Tensile Modulus	GPa	40	ASTM D 3039
Flexural Strenght	MPa	765	ASTM D 790
Flexural Modulus	GPa	41	ASTM D 790
I.L.S.S.	MPa	55	ASTM D 2344
Compressive Strength	MPa	t.b.d.	Modified ASTM D 695 (SACMA SRM 1-88)
G_{Ic}	J/m²	t.b.d.	ISO CD 15024

(*) The tests were carried out @ 23°C and 60% R.H. on specimens cured in std conditions (dwell @125° for 1 hour in hot plate press. External pressure applied: 3 MPa). The tests were performed along the fiber direction.

Figure 3-1. Properties of UD glass prepreg UE400 REM

For the subsequent analysis it is important to know what is the real cured ply thickness of UE400-REM. Thus a thickness micrographic of a tubular sample in (2) was done and is reported in Figure 3-2. The sample is made of an inner layer of VV345T fabric and three layers of UE400-REM; what matters are the unidirectional layers and, as is possible to note, the thickness is about 947 µm. Thus a single layer of UE400-REM is about 315 µm.

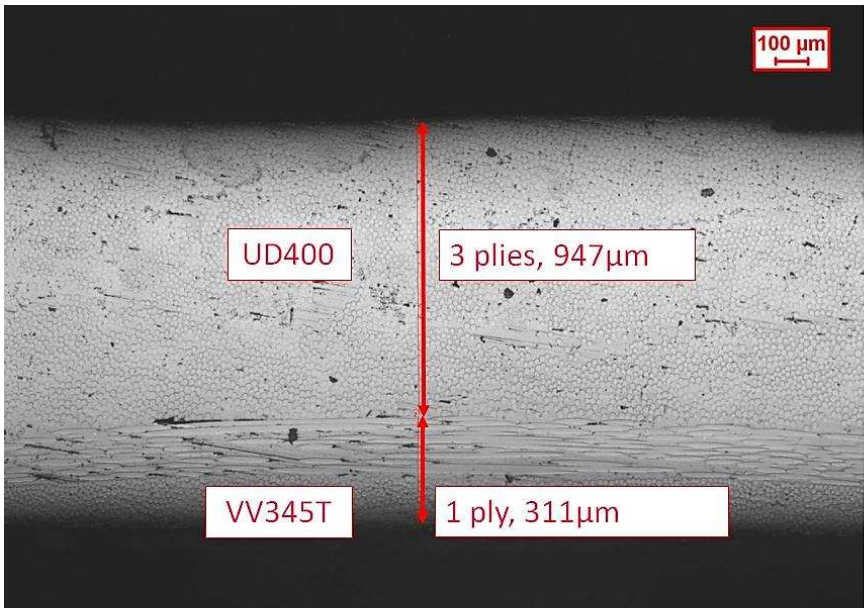

Figure 3-2. Section of tubular samples used in thesis work (2). It is possible to see the fabric and the UD layers and their corresponding thickness

Subsequently, a problem about the practical realization of this laminate comes out. In fact, the average thickness of a single layer of UD400-REM is approximately 0.315 mm and then with the chosen lay-up the final thickness of the laminate is about 11.34 mm. With this value of thickness the technology production with autoclave molding might not be very reliable, because the probability of porosity in the material is very high. Therefore it could be necessary to introduce some intermediate bags during the processes in order to divide the material and reduce the probability of porosity; however this solution is rather complicated and very expensive. To resolve this problem the chosen lay-up was reduced, resulting in two possibilities:

$[0/(+\vartheta)_3/0/(-\vartheta)_3]_s$ (I)

$[0/(+\vartheta)_2/0/(-\vartheta)_2]_s$ (II)

With the first solution (I) the total thickness of the laminate is about 5.04 mm, whilst with the second solution (II) it is about 3.78 mm. Both values are adequate for the autoclave molding technology, moreover with both possibilities the constraint condition on sides layers doesn't change and the off-axis layers are quite thicker to observe the damages.

A final consideration is that, looking at the conclusions of *Quaresimin-Susmel-Talreja* in (3) and reported in chapter 2, the combination of shear and transverse stress could have a significant effect on the fatigue behavior. Thus, the present project considers only λ_{12} as a parameter to replicate as in tubular samples. No coincidence, one of our main purposes is to investigate the effects of the shear component, which is well represented by the biaxiality ratio λ_{12}.

In the next paragraph it is presented the off-axis angle choice.

3.3 THEORETICAL PRE-ANALYSIS

As reported in chapter 2, the local stress state and consequently the biaxiality ratio λ_{12} are function of the off-axis angle. So now, the goal is to determine the angle that generates the desired stress state and biaxiality ratios.

The values of λ_{12} to obtain are the same used in the tests with tubular samples, and are:

$\lambda_{12} = 0.5$

$\lambda_{12} = 1$

$\lambda_{12} = 2$

Start with an analysis of how λ_{12} varies as a function of the off-axis angle ϑ, in this way is possible to determine the angle that generates the wanted values of λ_{12}. To do this was used a simple software named SACL, which allows to automatically deploy the Classic Lamination Theory of composite materials and to get the stress state ply-by-ply in material reference. SACL isn't a finite elements software but it is sufficient and useful to guide the search quickly. After this, it is possible to do a precise analysis, with finite elements, of the results obtained from this preliminary study.

The analysis was conducted for the lay-up $[0/(+\vartheta)_3/0/(-\vartheta)_3]_s$, assuming a sample size of 20 x 200 mm and the thickness of each layer of 0.315 mm. Only this lay-up was studied in this section, because the other possible lay-up leads to the same results in terms of biaxiality ratio; the differences between the two lay-ups are analyzed in the next paragraph through a more careful study. The load applied (F_y) is uniaxial tensile and equal to 10 MPa along the longitudinal direction, see Figure 3-3. The elastic properties of the individual lamina are those obtained from tests conducted in the previous thesis work (2) and are below reported.

$E_L = 34860 \quad [MPa]$ *3.1*

$E_T = 9419 \quad [MPa]$ *3.2*

$G_{LT} = 3193 \quad [MPa]$ 3.3

$\nu_{LT} = 0.326$ *3.4*

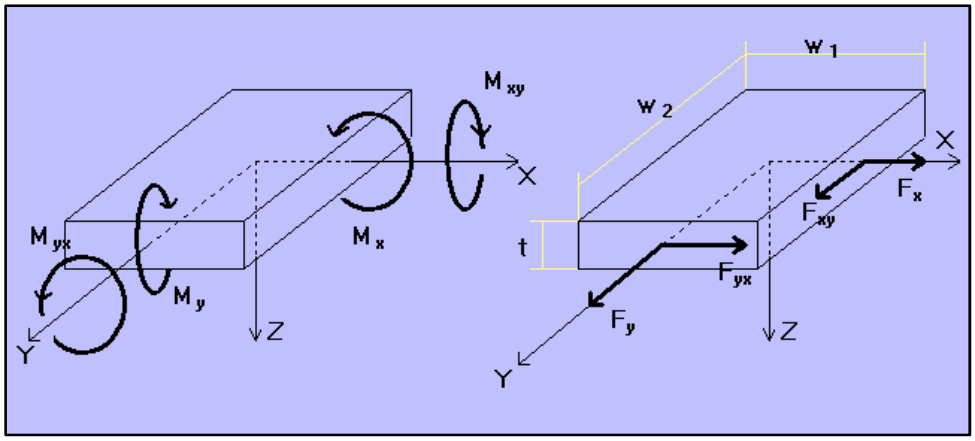

Figure 3-3. Summary of the reference system used for the loads and the geometry of the sample

Once these data were entered, the off-axis angle was varied from 90 to 0 degrees, recording for each time the values of the components of tension in material reference, and then calculating the values of λ_{12} with the equation 2.8; these are summarized in Table 3.1.

ANGLE	σ_{22}	τ_{12}	$\lvert\lambda_{12}\rvert$
[°]	[MPa]	[MPa]	-
90	5.883	0.000	0
85	5.849	0.389	0.067
80	5.745	0.785	0.137
75	5.558	1.192	0.214
70	5.268	1.610	0.306
65	4.848	2.032	0.419
62	4.522	2.278	0.504
60	4.272	2.434	0.570
58	3.995	2.580	0.646
55	3.529	2.772	0.785
50	2.647	2.984	1.127
45	1.714	3.005	1.754
42	1.186	2.913	2.456
40	0.867	2.810	3.240
35	0.234	2.437	10.402
30	0.134	1.972	14.694
25	0.274	1.503	5.496
20	0.263	1.086	4.127
15	0.183	0.739	4.041
10	0.091	0.455	4.986
5	0.024	0.216	8.954
0	0	0	0

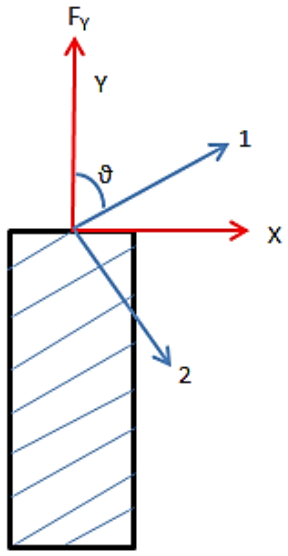

Figure 3-4. Material reference (1, 2) and structure reference (X, Y)

Table 3.1. Values of the biaxiality ratio λ_{12} by varying the off-axis angle for a laminated with lay-up $[0/(+\vartheta)_3/0/(-\vartheta)_3]_S$

Then, in Figure 3-5 the trend of λ_{12} is plotted in function of ϑ.

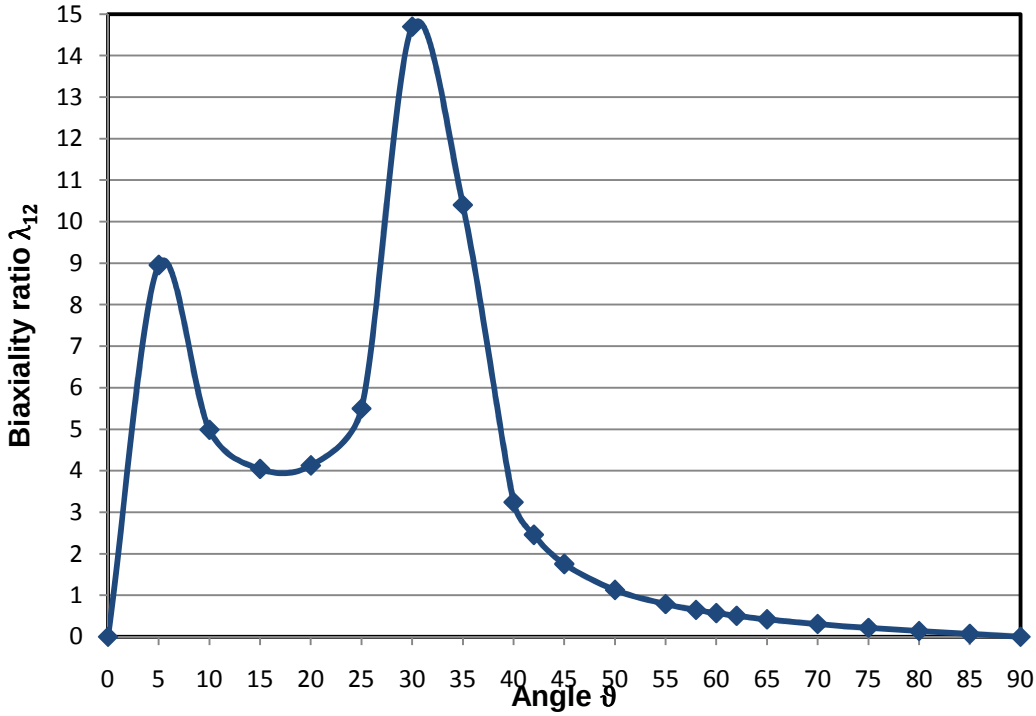

Figure 3-5. Trend of the biaxiality ratio λ_{12} respect to the off-axis angle ϑ with layup $[0/(+\vartheta)_3/0/(-\vartheta)_3]s$

Observing the trend of the biaxiality ratio, it is possible to note that there isn't an accurate correlation between λ_{12} and ϑ; however there is a strong sensitivity of λ_{12} especially for an angle between 0 and 50 degrees. This means that a small variation of ϑ causes a large variation of λ_{12}. This feature, in practice, leads to the fact that if during the production process the fibers change their orientation, the variation of the stress field (and hence of λ_{12}) will be very high. Looking at the values of the biaxiality ratio in Figure 3-5, the off-axis angles that allows obtaining the desired λ_{12} are the following:

$$\begin{aligned} \lambda_{12} = 0.5 \ &\rightarrow \ \vartheta = 60° \\ \lambda_{12} = 1 \ &\rightarrow \ \vartheta = 50° \\ \lambda_{12} = 2 \ &\rightarrow \ \vartheta = 42° \end{aligned} \qquad 3.5$$

However this choice is very risky, because the off-axis angles 42° and 50° leads to the zone of strong sensitivity of λ_{12}. Samples made with these two theoretical angles, could easily have a different off-axis angle because of the production process; thus the samples could have a biaxiality ratio very different from that desired. To work around this delicate problem, it was decided to consider only λ_{12}=0.5 and thus a corresponding angle of 60 degrees; so the sensitivity of λ_{12} is much less strong and therefore if the production

process changes the fibers orientation the value of the biaxiality ratio remains in any case very closed to that intended.

In the project concerning the fatigue behavior of tubular samples (2) it was necessary to introduce in the samples an intermediate fabric layer in order to reinforce the material. In fact, the samples were initially made of three layers of unidirectional prepreg at 90° respect to the tube axis; however with this configuration the samples stressed with a fatigue loading arrived to failure in an almost instantaneous way, and not giving any chance to observe a progressive damage and any fatigue behavior at high number of cycles. The presence of the fabric layer was studied with a finite elements analysis to verify how the stress state in the material was modified by the presence of the fabric. The result of this analysis was that the biaxiality ratio changes from 0.5 to 0.63, i.e. the fabric change the multiaxial stress field. After this consideration, it is a good choice in the present work to choose an off-axis angle of 60° to replicate the th eoretical value λ_{12} =0.5, because the real λ_{12} value is 0.57 and it is closer to the real value of the biaxiality ratio in the tubular samples (λ_{12}=0.63).

One more observation to do regarding the choice of the off-axis angle, is that the considered values must reflect the criteria for an industrial application; i.e. the angles must be equal to those commonly used in practice, such values widely used are: 30, 45, 60 and 90 degrees. Thus, the choice of the angle made in the present work is in line with this principle. In general, it would be meaningless to study a configuration that doesn't find any practical application. We reiterate that, in the analysis of composite materials, the practical point of view should not be forgotten, and we intend to pursue this principle.

3.4 FINITE ELEMENTS ANALYSIS

The chosen off-axis angle is 60°, thus the possible lay-up are:

$[0/(+60)_3/0/(-60)_3]_s$ (**A**)

$[0/(+60)_2/0/(-60)_2]_s$ (**B**)

At this point a careful analysis of this two options must be done, in order to verify the real stress state and therefore the real value of the biaxiality ratio λ_{12}. In fact, this subsequent analysis aims to consider the influence of the number of layers and the free-edge effects on the stress state.

The two lay-up were analyzed with the finite elements software ABAQUS 6.10®, and here the various steps of this study are reported. To simplify, only the steps for lay-up (B) are presented.

Model creation

The thickness of the laminate is fairly low so the modeling is done using the solid elements, also in this way it is possible get the stresses values across the entire thickness of a single element.

The dimensions of the laminate are:

Length: 200 mm

Width: 20 mm

Single layer thickness: 0.350 mm

Laminate thickness with lay-up (A): 5.60 mm

Laminate thickness with lay-up (B): 4.20 mm

ABAQUS has a well-developed solid modeler, which allows creating a solid model quickly using the extrusion function. Figure 3-6 shows the model of the laminate.

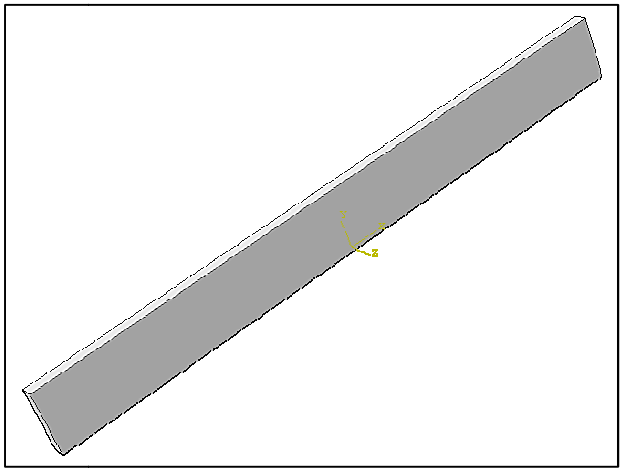

Figure 3-6. Solid model of the laminate

Meshing

The division model made allows having square elements with sides of 1 mm. In particular the length is divided into 200 parts, while the width is divided into 20 parts. The element used is C3D8R, 8-node linear brick. In Figure 3-7 the mesh obtained is shown. Along the thickness there is only one element.

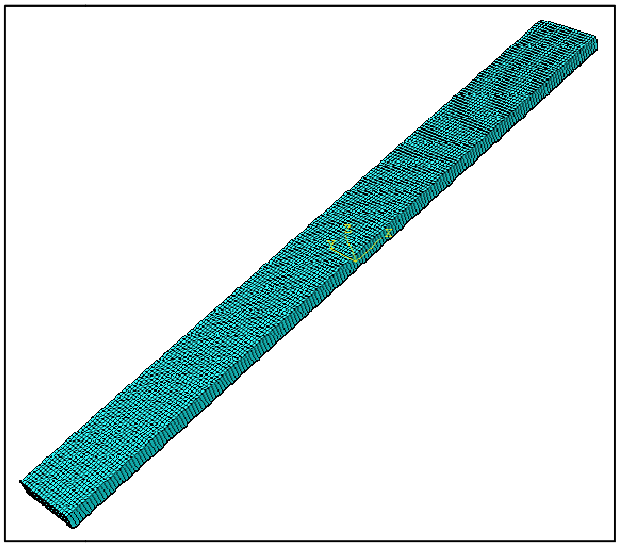

Figure 3-7. Example of mesh obtained

Composite Lay-up

ABAQUS has a very clear interface for the creation of lay-up. For each layer are required: layer name, in which model (region) is the layer, material, relative thickness respect to the other layers, system of reference, off-axis rotation angle and number of integration points along the thickness. The Figure 3-8 summarizes all the entered data.

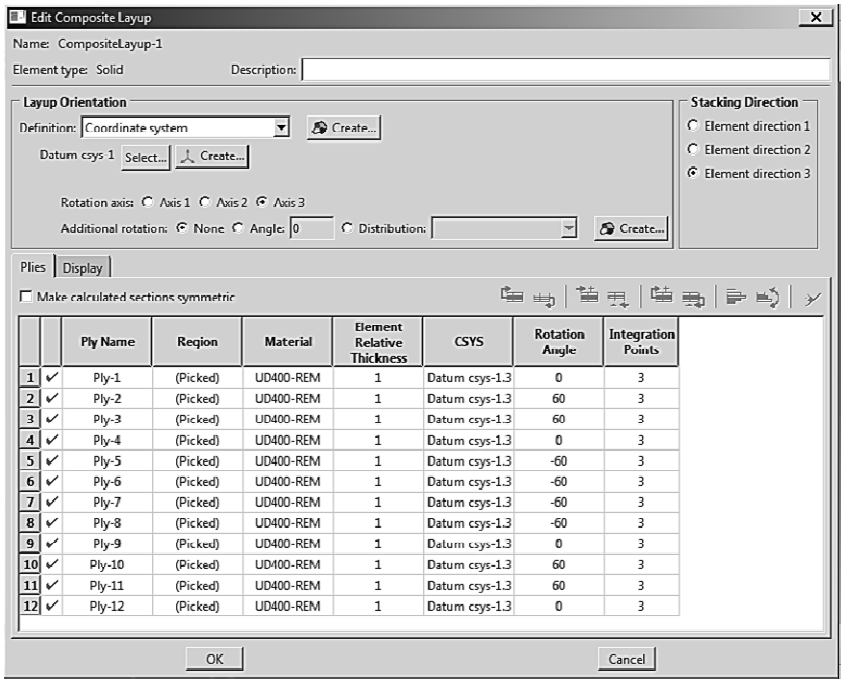

		Ply Name	Region	Material	Element Relative Thickness	CSYS	Rotation Angle	Integration Points
1	✓	Ply-1	(Picked)	UD400-REM	1	Datum csys-1.3	0	3
2	✓	Ply-2	(Picked)	UD400-REM	1	Datum csys-1.3	60	3
3	✓	Ply-3	(Picked)	UD400-REM	1	Datum csys-1.3	60	3
4	✓	Ply-4	(Picked)	UD400-REM	1	Datum csys-1.3	0	3
5	✓	Ply-5	(Picked)	UD400-REM	1	Datum csys-1.3	-60	3
6	✓	Ply-6	(Picked)	UD400-REM	1	Datum csys-1.3	-60	3
7	✓	Ply-7	(Picked)	UD400-REM	1	Datum csys-1.3	-60	3
8	✓	Ply-8	(Picked)	UD400-REM	1	Datum csys-1.3	-60	3
9	✓	Ply-9	(Picked)	UD400-REM	1	Datum csys-1.3	0	3
10	✓	Ply-10	(Picked)	UD400-REM	1	Datum csys-1.3	60	3
11	✓	Ply-11	(Picked)	UD400-REM	1	Datum csys-1.3	60	3
12	✓	Ply-12	(Picked)	UD400-REM	1	Datum csys-1.3	0	3

Figure 3-8. Edit composite lay-up in Abaqus

The coordinate system, 1-2-3 axes, used is shown in Figure 3-9; i.e. axis 1 along the longitudinal direction (Y), axis 2 along the transverse direction (X) and axis 3 in the perpendicular direction (Z). These axes correspond to the material reference.

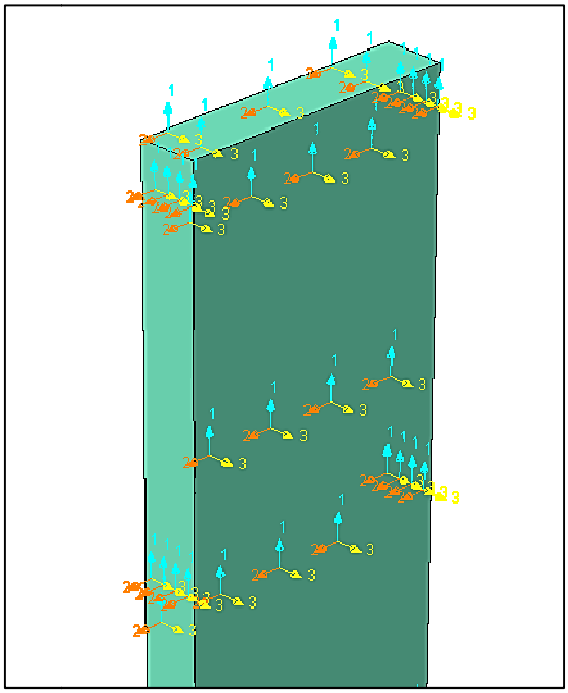

Figure 3-9. Local coordinate system imposed in the Abaqus model

Constraint and loading conditions

The samples are subjected to a tensile cycling loading with a load ratio *R* almost equal to zero, thus it is sufficient to apply a load equal to the amplitude of the solicitation. In this case the value of the load is 10 MPa applied in the longitudinal direction Y on the end section. Regarding the constraint condition, it is clamping on the other end section. Figure 3-10 shows the conditions imposed.

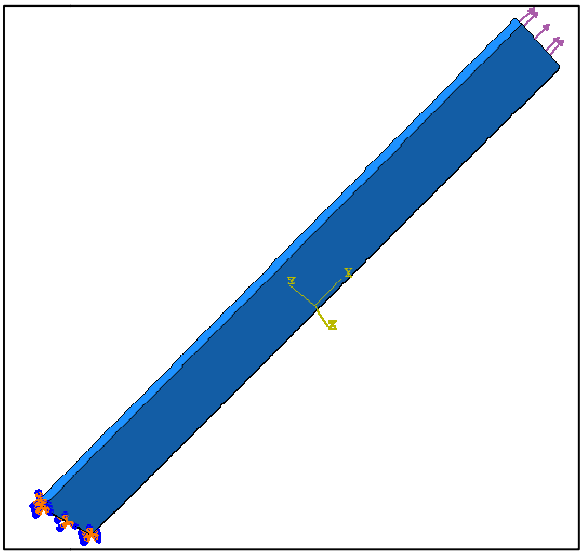

Figure 3-10. Constraint and loading conditions imposed in the Abaqus model

Model validation

Before analyzing the results a brief check was made to ensure the reliability of the implemented model. To do this, the following variables were analyzed:

1. Tensile stress in direction 1, along the longitudinal axis of the first layer. Figure 3-11.
2. Strain in direction 1, along the longitudinal axis of the first layer. Figure 3-12.
3. Displacement in direction 1, along the longitudinal axis of the first layer. Figure 3-13.

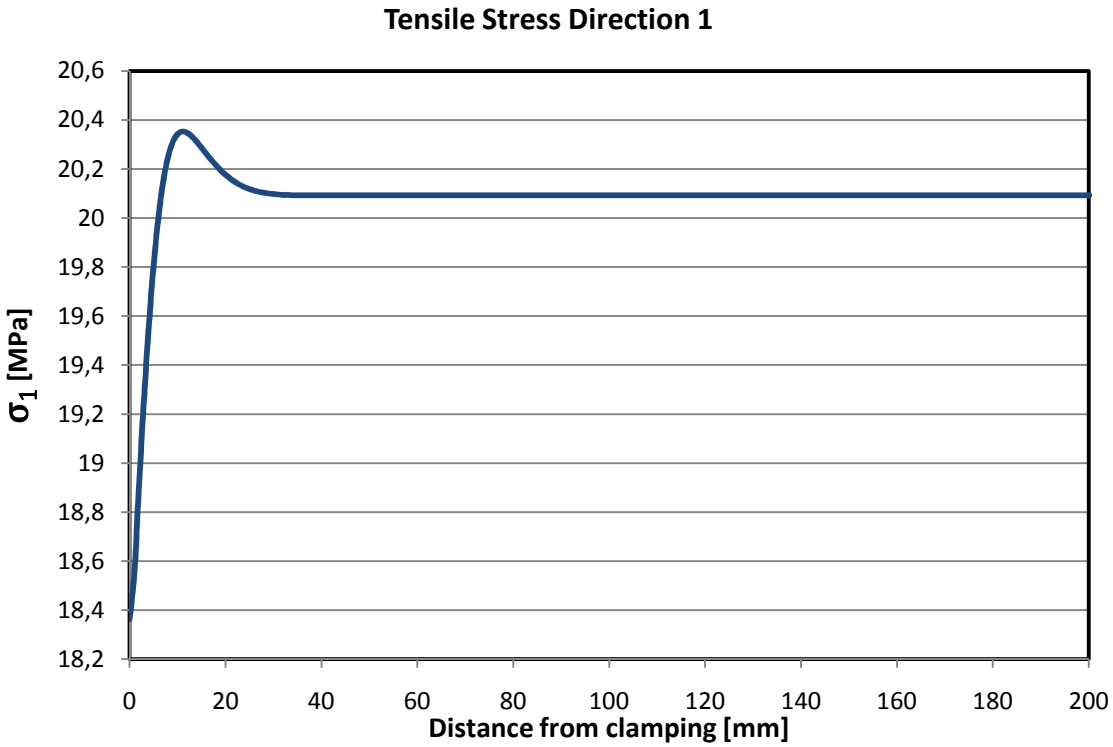

Figure 3-11. Tensile stress σ1 trend along the longitudinal axis

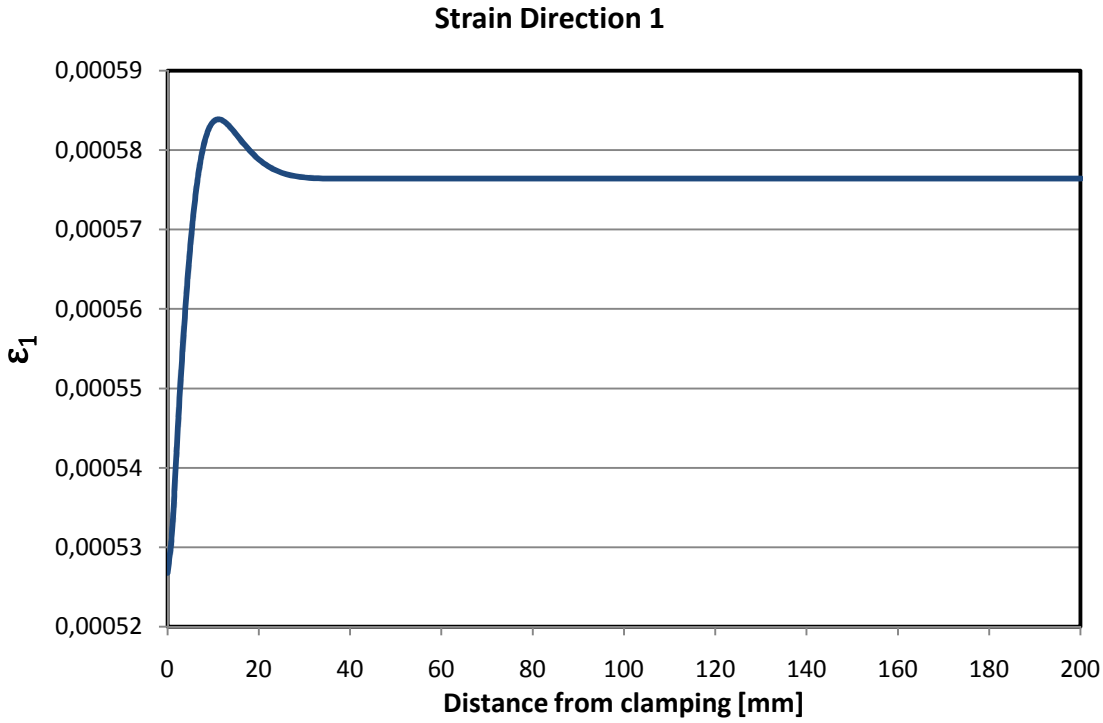

Figure 3-12. Strain ε1 trend along the longitudinal axis

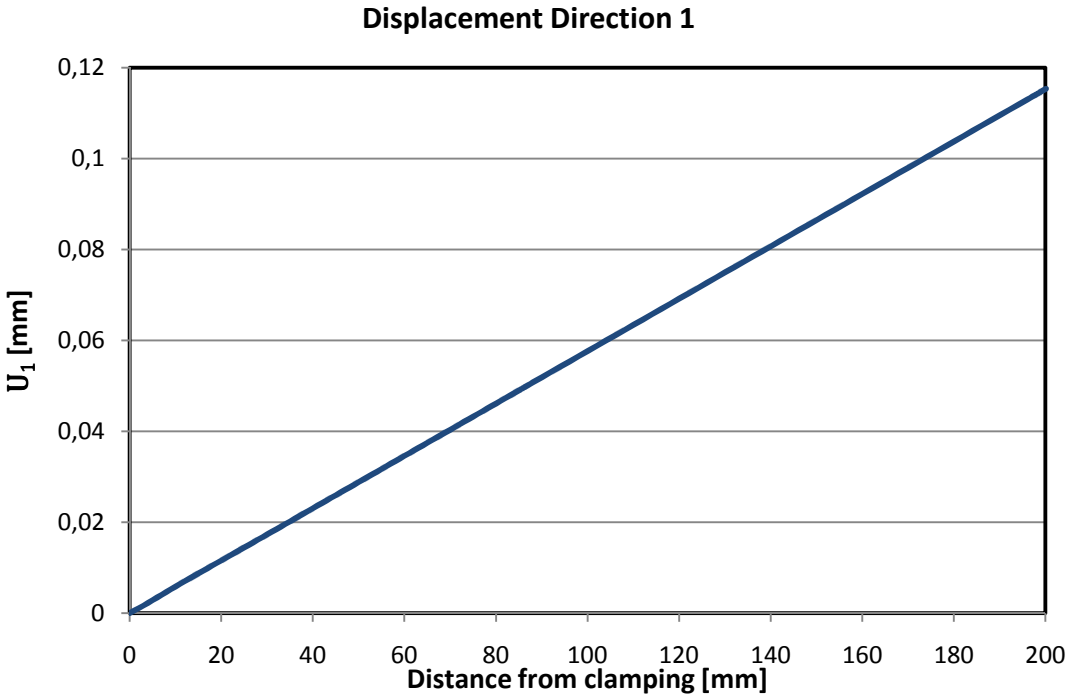

Figure 3-13. Displacement U1 trend along the longitudinal axis

As expected, the implemented model is correct. Looking at the above graphs:

1. The trend of tensile stress σ_1 is constant for almost the entire length of the sample, except in the initial part where there is a stress peak due to the effects of the constraint imposed. However, this variation is negligible.
2. The trend of strain ε_1 is equal to the stress one, thus the same considerations can be made.
3. The trend of displacement U_1 is correct, it is linear and starts from zero at the clamping, and stops to the maximum value in the opposite extremity.

3.4.1 Simulation results of $[0/(+60)_2/0/(-60)_2]_s$

The finite element model leads to obtain the stress state ply-by-ply along the thickness. In this way it is possible to determine the real value of the biaxiality ratio λ_{12} present in each layer, and then to verify whether it is exactly what was looked for. The FEM analysis shows that the stress components doesn't vary along the longitudinal direction of the samples, unless the area closed the clamping; for example Figure 3-14 shows the trend of the stress σ_1 on the first layer.

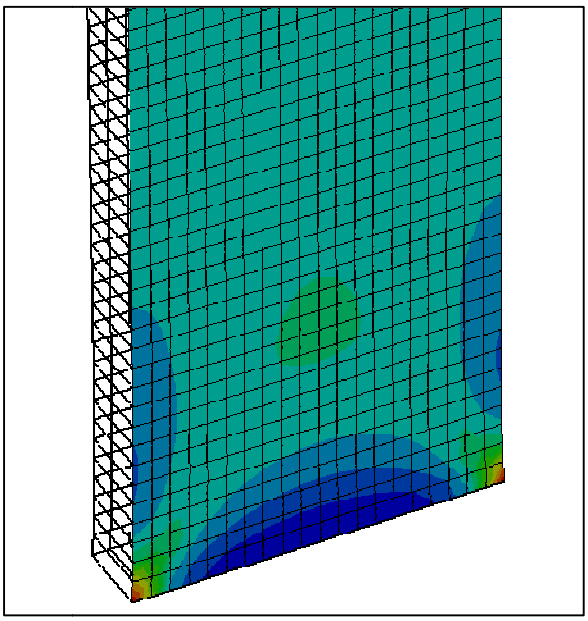

Figure 3-14. Zoom of stress σ1 trend on the first layer closed to clamping

For this reason, only one element of the model is analyzed, located in the central area of the sample, where the stress state is very constant. As mentioned, for each layer there are three integration points along the thickness, Figure 3-16, this means that the stress value can get on top, on bottom and in middle of each layer.

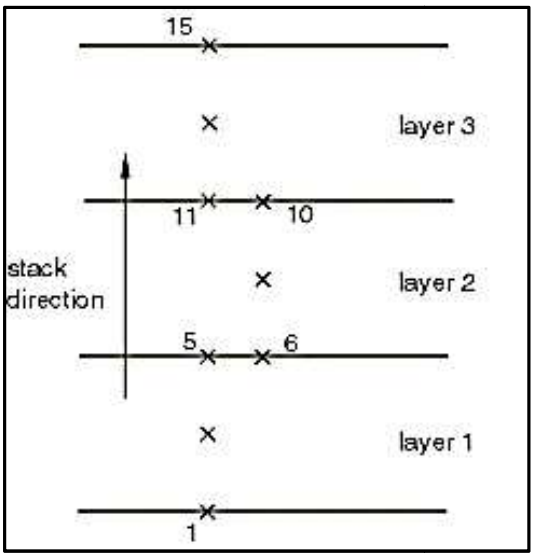

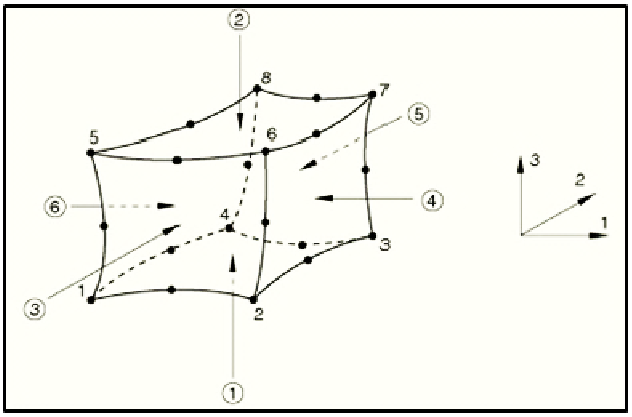

C3D8R

Figure 3-16. Integration points along the thickness

Also, the element C3D8R in Figure 3-15, has four nodes on the top and four on the bottom and the single value of solution that we consider, for the top and for the bottom, is the average of the solutions in the four nodes. Then for the middle plane added (because there are three integration points), the stress values are given by the average of the solutions in the four nodes in the middle.
The following Table 3.2 summarizes the stress state and the values of biaxiality ratio λ_{12}, for the configuration $[0/(+60)_2/0/(-60)_2]_s$.

The stress state indicates that the biaxiality ratio on off-axis layers is equal to 0.513. This is the real value of λ_{12}, since it takes into account the influence of the layers number and the free-edge effects. The value is very similar to the λ_{12} determined in the previous analysis of the planar samples in Table 3.1 (0.57), but it's not very closed to the real value in tubular samples (0.63) that we want to replicate. However, in order to have an off-axis angle similar to the industrial application, we have to accept this configuration. For more clarity the plain stress state ply-by-ply is also plotted in Figure 3-17.

THICKNESS	σ_1	σ_2	τ_{12}	λ_{12}	ANGLE
[mm]	[Mpa]	[Mpa]	[Mpa]	-	[°]
0	20.093	-1.175	9.06E-10	0	
0.175	20.093	-1.175	9.04E-10	0	**0°**
0.350	20.093	-1.175	9.02E-10	0	
0.350	1.762	3.778	-1.939	-0.513	
0.525	1.762	3.778	-1.939	-0.513	
0.700	1.762	3.778	-1.939	-0.513	**$(+60°)_2$**
0.700	1.762	3.778	-1.939	-0.513	
0.875	1.762	3.778	-1.939	-0.513	
1.050	1.762	3.778	-1.939	-0.513	
1.050	20.093	-1.175	8.95E-10	0	
1.225	20.093	-1.175	8.93E-10	0	**0°**
1.400	20.093	-1.175	8.91E-10	0	
1.400	1.762	3.778	1.939	0.513	
1.575	1.762	3.778	1.939	0.513	
1.750	1.762	3.778	1.939	0.513	**$(-60°)_2$**
1.750	1.762	3.778	1.939	0.513	
1.925	1.762	3.778	1.939	0.513	
2.100	1.762	3.778	1.939	0.513	
2.100	1.762	3.778	1.939	0.513	
2.275	1.762	3.778	1.939	0.513	
2.450	1.762	3.778	1.939	0.513	**$(-60°)_2$**
2.450	1.762	3.778	1.939	0.513	
2.625	1.762	3.778	1.939	0.513	
2.800	1.762	3.778	1.939	0.513	
2.800	20.093	-1.175	8.77E-10	0	
2.975	20.093	-1.175	8.75E-10	0	**0°**
3.150	20.093	-1.175	8.73E-10	0	
3.150	1.762	3.778	-1.939	-0.513	
3.325	1.762	3.778	-1.939	-0.513	
3.500	1.762	3.778	-1.939	-0.513	**$(+60°)_2$**
3.500	1.762	3.778	-1.939	-0.513	
3.675	1.762	3.778	-1.939	-0.513	
3.850	1.762	3.778	-1.939	-0.513	
3.850	20.093	-1.175	8.66E-10	0	
4.025	20.093	-1.175	8.64E-10	0	**0°**
4.200	20.0934	-1.175	8.62E-10	0	

Table 3.2. Abaqus solutions for plain stress state and biaxiality ratio ply-by-ply for laminated with lay-up $[0/(+60)_2/0/(-60)_2]_s$

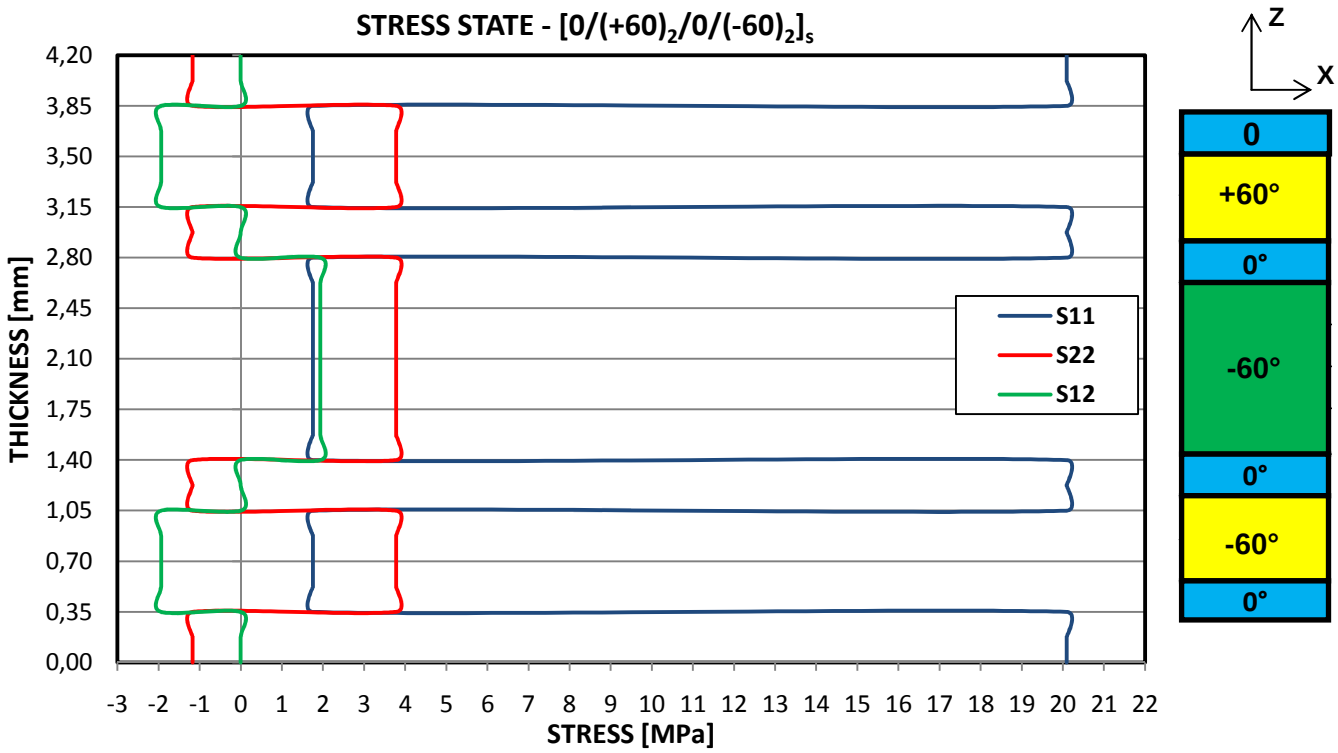

Figure 3-17. Abaqus solutions for plain stress state through the thickness, lay-up $[0/(+60)_2/0/(-60)_2]_s$ with 10 MPa of nominal stress

The chart in Figure 3-17 shows how stress components are influenced by layers interfaces, i.e. between one layer and an other one, stresses have an imbalance. However, this effect is small and also in off-axis layers there is a large zone in which the stresses are constant. To complete the information set on the stress state presents with this lay-up, the biaxiality ratio trend through the thickness is plotted in Figure 3-18 using the solutions from the ABAQUS model. As expected the values of λ_{12} remain constant along the off-axis layers, expect for the contact zones between layers with different orientation. In these points, where λ_{12} turns out to be unbalanced, there are slight peaks values. However, this phenomenon is rather limited and therefore it doesn't influence much the analysis done in this work.

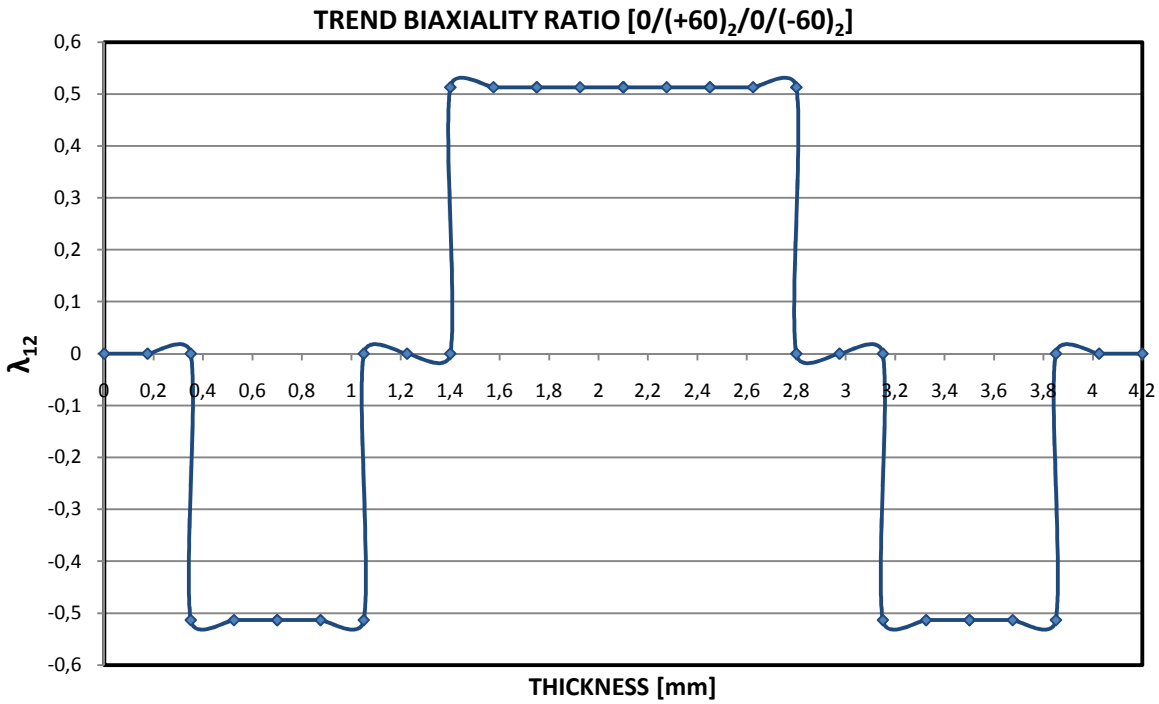

Figure 3-18. Biaxiality ratio λ_{12} through the thickness, with lay-up $[0/(+60)_2/0/(-60)_2]_s$

3.4.2 Simulation results of $[0/(+60)_3/0/(-60)_3]_s$

The analysis of this lay-up it's similar to the previous one, thus following the results about the ABAQUS model are directly reported in Table 3.3:

THICKNESS	σ_1	σ_2	τ_{12}	λ_{12}	ANGLE
[mm]	[MPa]	[MPa]	[MPa]	-	[°]
0.000	23.084	-1.432	-2.37E-09	0	0°
0.175	23.084	-1.432	-2.37E-09	0	
0.350	23.084	-1.432	-2.37E-09	0	
0.350	1.796	4.320	-2.251	-0.521	$(+60°)_3$
0.525	1.796	4.320	-2.251	-0.521	
0.700	1.796	4.320	-2.251	-0.521	
0.700	1.796	4.320	-2.251	-0.521	
0.875	1.796	4.320	-2.251	-0.521	
1.050	1.796	4.320	-2.251	-0.521	
1.050	1.796	4.320	-2.251	-0.521	
1.225	1.796	4.320	-2.251	-0.521	
1.400	1.796	4.320	-2.251	-0.521	
1.400	23.084	-1.432	-2.37E-09	0	0°
1.575	23.084	-1.432	-2.37E-09	0	
1.750	23.084	-1.432	-2.37E-09	0	
1.750	1.796	4.320	2.251	0.521	$(-60°)_3$
1.925	1.796	4.320	2.251	0.521	
2.100	1.796	4.320	2.251	0.521	
2.100	1.796	4.320	2.251	0.521	
2.275	1.796	4.320	2.251	0.521	
2.450	1.796	4.320	2.251	0.521	
2.450	1.796	4.320	2.251	0.521	
2.625	1.796	4.320	2.251	0.521	
2.800	1.796	4.320	2.251	0.521	
2.800	1.796	4.320	2.251	0.521	$(-60°)_3$
2.975	1.796	4.320	2.251	0.521	
3.150	1.796	4.320	2.251	0.521	
3.150	1.796	4.320	2.251	0.521	
3.325	1.796	4.320	2.251	0.521	
3.500	1.796	4.320	2.251	0.521	
3.500	1.796	4.320	2.251	0.521	
3.675	1.796	4.320	2.251	0.521	
3.850	1.796	4.320	2.251	0.521	
3.850	23.084	-1.432	-2.37E-09	0	0°
4.025	23.084	-1.432	-2.37E-09	0	
4.200	23.084	-1.432	-2.37E-09	0	
4.200	1.796	4.320	-2.251	-0.521	$(+60)_3$
4.375	1.796	4.320	-2.251	-0.521	
4.550	1.796	4.320	-2.251	-0.521	
4.550	1.796	4.320	-2.251	-0.521	
4.725	1.796	4.320	-2.251	-0.521	
4.900	1.796	4.320	-2.251	-0.521	
4.900	1.796	4.320	-2.251	-0.521	
5.075	1.796	4.320	-2.251	-0.521	
5.250	1.796	4.320	-2.251	-0.521	
5.250	23.084	-1.432	-2.37E-09	0	0°
5.425	23.084	-1.432	-2.37E-09	0	
5.600	23.084	-1.432	-2.37E-09	0	

Table 3.3. Abaqus solutions for plain stress state and biaxiality ratio ply-by-ply for laminate with lay-up $[0/(+60)_3/0/(-60)_3]_s$

The stress state as reported above (Table 3.3), indicates that the biaxiality ratio on off-axis layers is equal to 0.521. Also with this lay-up the real value of in the planare laminate is not very closed to the one obtained in the tubular samples. Anyway, for pratical reason it is accepted.

The chart in Figure 3-20, that shows the stress components trend through the ABAQUS model, has the same features as that the previous lay-up, thus the same consideration can be made. The only difference is that the zone in which the stress values are constant in this case is considerably higher.

Also for this configuration, the information set is completed with the biaxiality ratio trend plotted in Figure 3-20. The peaks values of stress along the interfaces are always present but in a limited way. With this lay-up the largest area, in which the stress state is constant, is further confirmed.

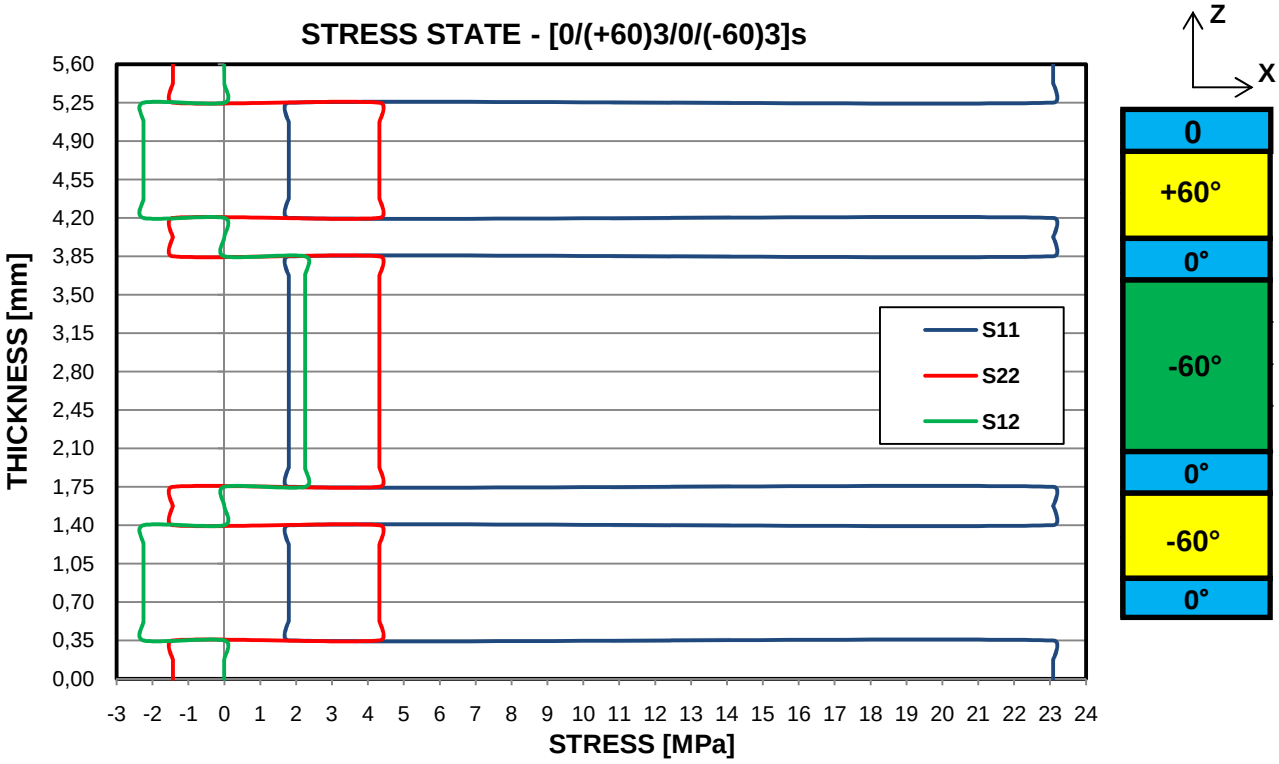

Figure 3-19. Abaqus solutions for plain stress state through the thickness, lay-up $[0/(+60)_3/0/(-60)_3]_s$ with 10 MPa of nominal stress

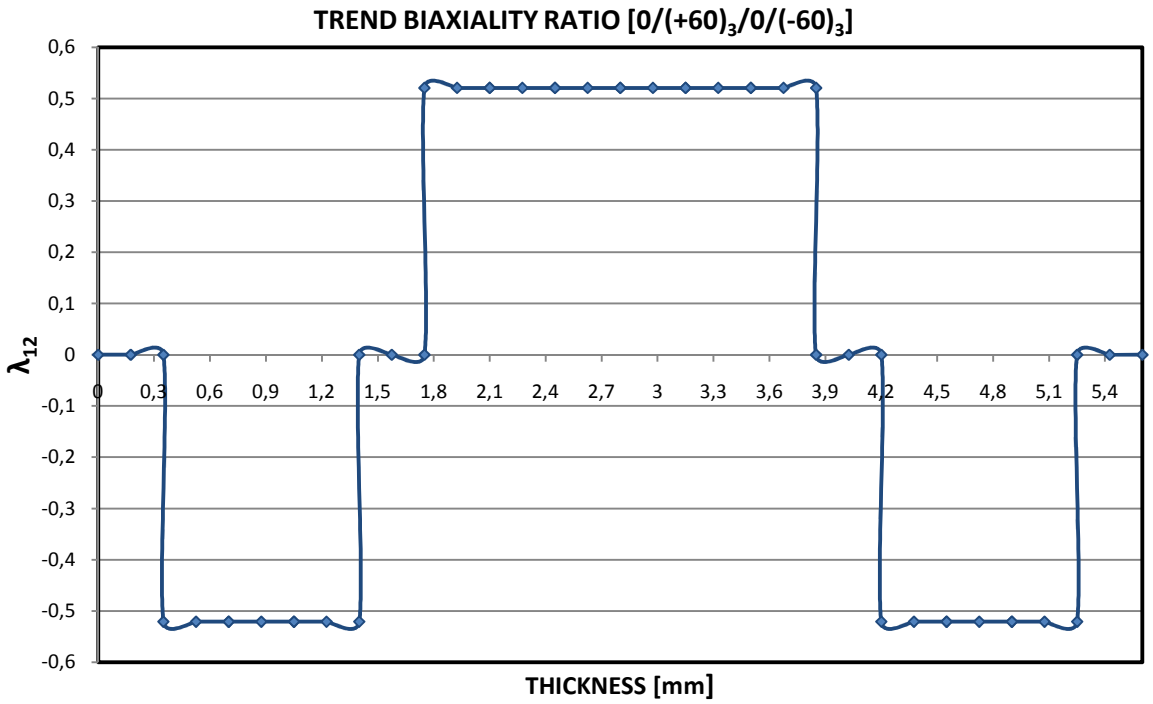

Figure 3-20. Biaxiality ratio λ_{12} through the thickness, with lay-up $[0/(+60)_3/0/(-60)_3]_s$

3.5 DISCUSSIONS

The analysis of the two possible lay-up lead to the conclusion that both are valid for the purpose of this work. In fact, for both configurations, the value of λ_{12} is sufficiently close to the desired one and also the stress state distribution is correct along the thickness of the sample. However, a technological consideration was made consulting with the manufacturer of composite materials and for the production of samples with the $[0/(+60)_3/0/(-60)_3]_s$ sequence, probably would be necessary to introduce an intermediate sack during the lamination (with the infusion sack process) in order to ensure the absence of porosity. So at this point, to speed up the production time and be able to save in economics terms, the final choice was the lay-up:

$$\mathbf{[0/(+60)_2/0/(-60)_2]_s}$$

Consequently, with the above configuration chosen, a panel with size 500x500 mm in UE400-REM (glass fiber / epoxy matrix) is started to manufacture in Italy at the laboratory of the University of Padova.

4 EXPERIMENTAL STATIC TEST

4.1 GENERALITY

This chapter discusses the static tests of the laminate with the chosen lay-up. In general, before performing the fatigue tests, it is always good to have information and data about the static behavior of the material such as tensile strength, strain at failure, stiffness and main mechanisms of damage. The material behavior under static loading is not the aim of this project but it can be very useful to calibrate the fatigue tests and to verify the material quality. In fact it is possible to highlight for example manufacture defects that can influence the future fatigue tests.

4.2 SAMPLES DESCRIPTION

A panel 500x500 mm of composite material UE400-REM, having the chosen lay-up $[0/(+60)_2/0/(-60)_2]_s$, was laminated in Italy at the laboratory of the University of Padova through the autoclave molding process and after a part was shipped to Denmark at the National Laboratory for Sustainable Energy.
Totally there was three panels with lay-up $[0/(+60)_2/0/(-60)_2]_s$ and dimensions 200 x 240 mm. At this point, the panels were prepared to obtain the samples that had been used for the tests. First the tabs with a length L_{TAB} of 60 mm were applied, and once the bond was completed panels were cut, Figure 4-2. For each panel nine samples with a width W of 24 mm, a total length L of 220 mm and a thickness t of 4.3 mm were obtained, Figure 4-1. Finally the samples for the static and fatigue tests were marked with a serial number, traced with a permanent marker, to facilitate the identification. The codification is composed with a letter that indicates the type of test *S*=static and with a serial number.

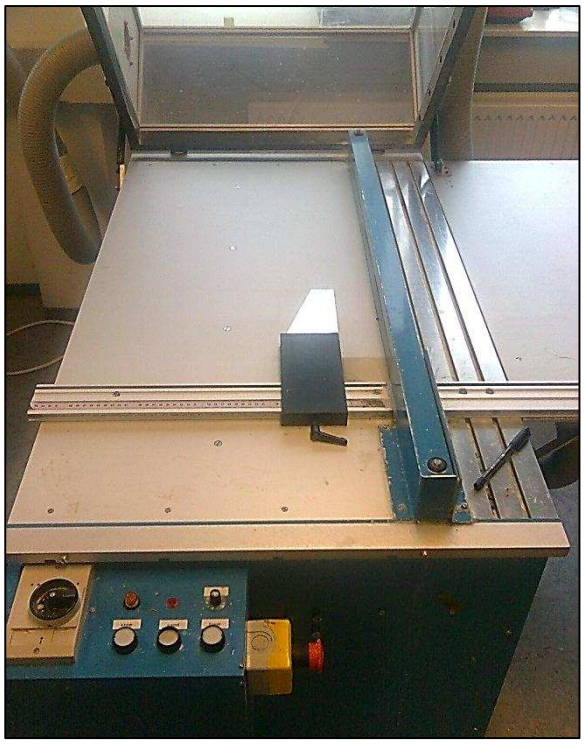

Figure 4-2. Machine circular saw for cutting samples

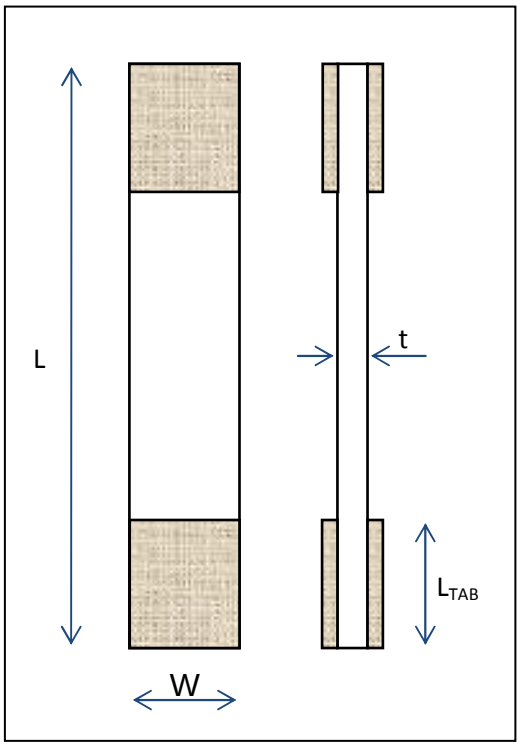

Figure 4-1. Sample for static and fatigue tests

4.3 TEST DESCRIPTION

The characteristics of the test system used for static tests are the follows:

- Machine hydraulically operated for uniaxial loading;
- Position transducer;
- Load cell of 200 KN;
- Uniaxial extensometers ±2.5 mm;

The tests were conducted with displacement control, the ramp speed was set as constant in the testing machine, the values of load and strain measured by the sensors were recorded. The value of the traction speed is 2 mm/min.
In Figure 4-3 a picture of the testing system is reported. The two uniaxial extensometers used allow obtaining more precise strain values, the software of the testing machine directly calculates an average value to use to trace the stress-strain curve of the material.

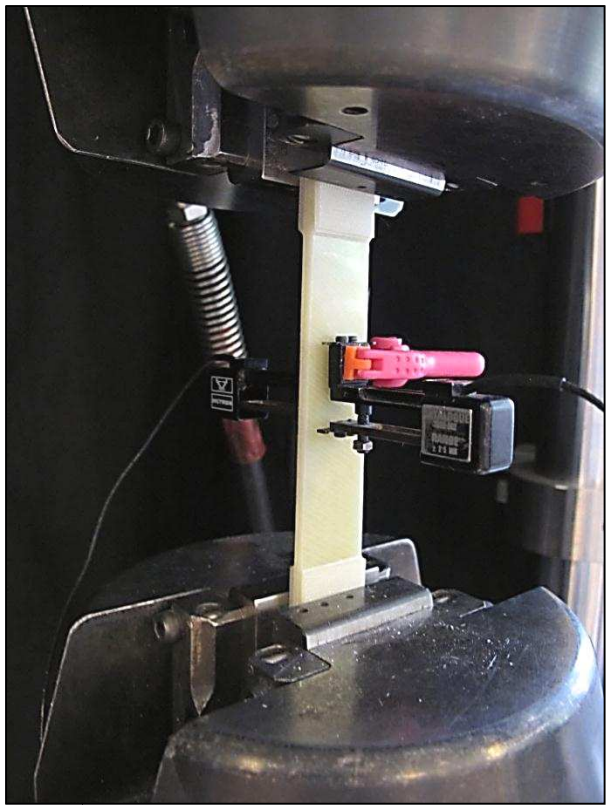

Figure 4-3. System used for static test

4.4 TEST RESULTS

In the Table 4.1, for each sample, are shown the values of the mechanical properties, recorded during the test.

Code	Gage Length [mm]	Thickness [mm]	Width [mm]	ε_R -	σ_R [MPa]	E [Mpa]
S-01	25	4.30	24.3	0.0210	316.5	17702.4
S-02	25	4.28	24.2	0.0279	320.3	17407.9
S-04	25	4.15	24.1	0.0240	326.4	18275.5
S-05	25	4.16	24.1	0.0257	337.9	18615.9
AVERAGE	-	-	-	0.0246	325.3	18000.4
STD DEV	-	-	-	0.00291	3.93	546.0

Table 4.1. Static tests results about four samples. The average values corresponds to the static mechanical properties of the composite laminate

After the tests, for each sample the stress-strain curve was constructed. In Figure 4-4 these curves are reported.

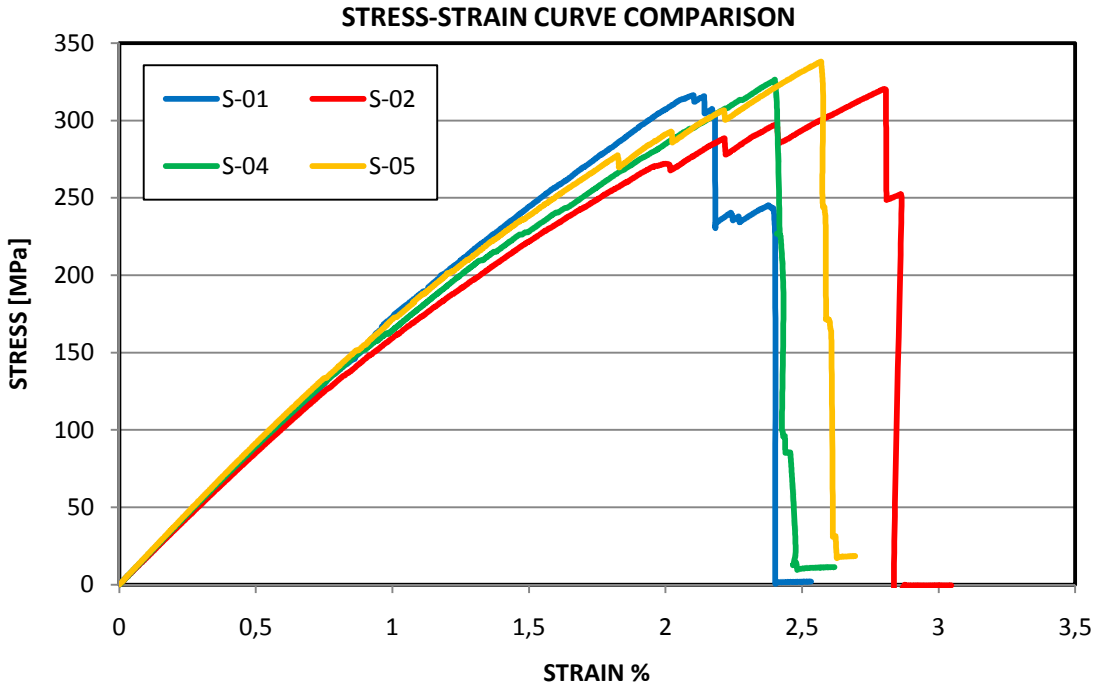

Figure 4-4. Stress-strain curves of static tests for each samples

Observing the previous chart, the stress-strain curves appear overlapped in the elastic region and all reach the same failure stress. The main difference is the strain value at failure. In order to better understand the static behavior of the material, a qualitative post-failure analysis of the samples is below reported.

4.4.1 Post-failure analysis of sample S-01

After the tensile stress the sample presents a very strong delamination which led to the separation into two parts along its longitudinal axis. Furthermore, the failure zone is located close to the tab, probably because of the influence on the stress state of the jaws clamping machine. At first sight with naked eye the delamination surface is very pronounced, see Figure 4-5 and Figure 4-6, almost has to suggest that it may be generated by the presence of a defect in the material that prevent two layers to be firmly attached.

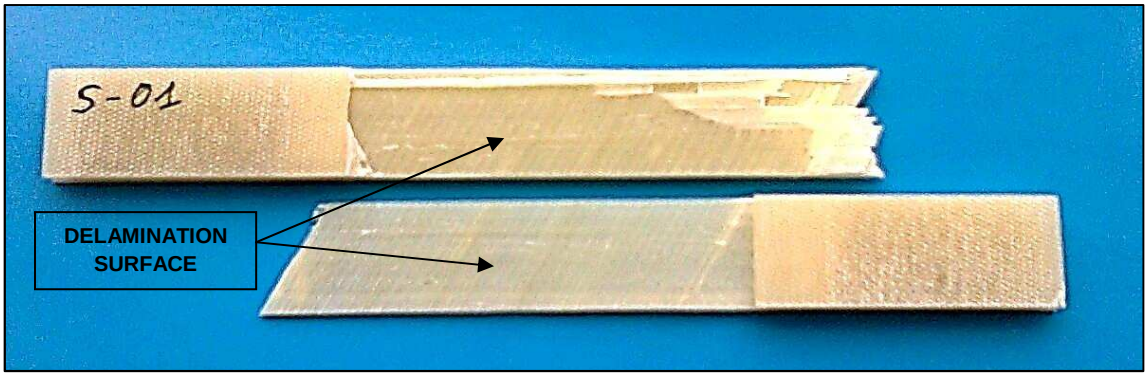

Figure 4-5. Sample S-01 after static failure

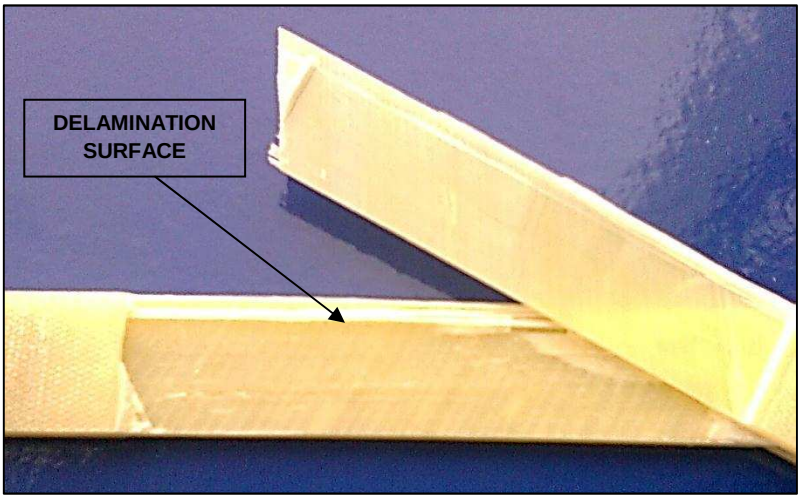

Figure 4-6. Sample S-01. Zoom on the delamination area

A subsequent microscopic analysis shows in details the surface of delamination. As reported in Figure 4-7 and Figure 4-8, on the surface fibers at zero degrees are marked and considering the thickness of the two halves in which the sample is broken, surely the failure surface is located on the interface between the first double layer at +60° and the second layer at 0° of the sample. Moreover, the 0° fibers appear also fairly clean without significant residual matrix attached. This feature suggests that could be some problems in the fibers-matrix interface, i.e. the fiber surface isn't well attached with the matrix. The cause of this might be the chemical deposition applied on the fibers surface during the production process.

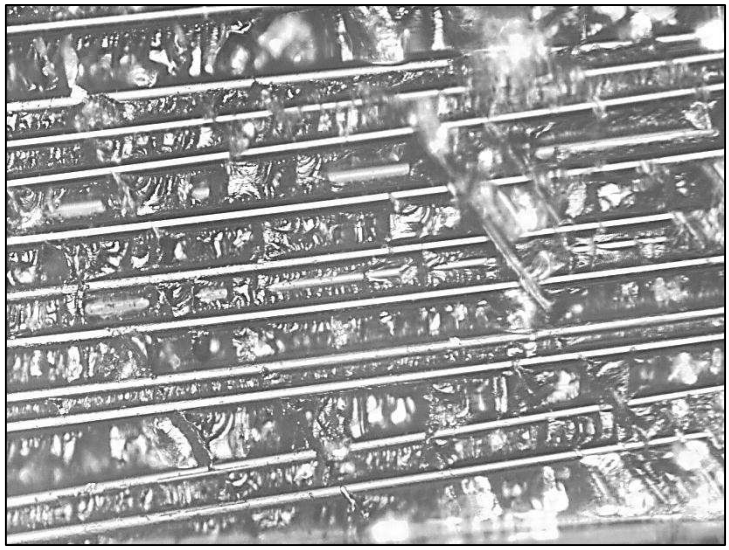

Figure 4-7. Optical microscope image of delamination surface of sample S-01. Zoom 20x

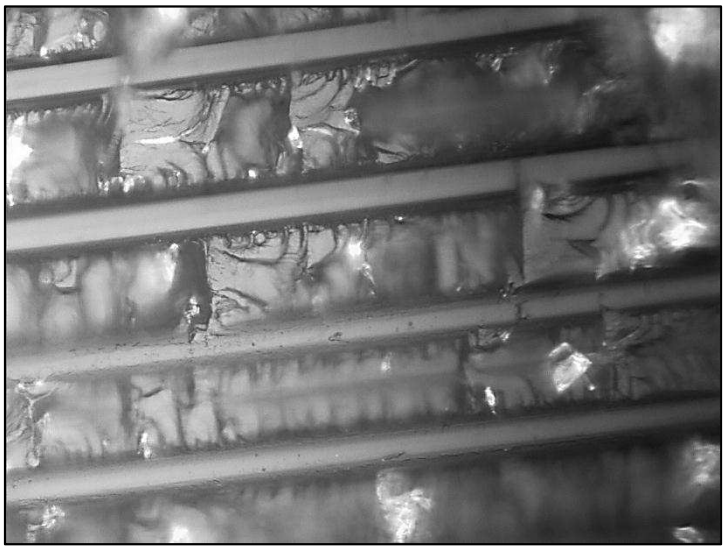

Figure 4-8. Optical microscope image of delamination surface of sample S-01. Zoom 50x

4.4.2 Post-failure analysis of sample S-02

Even this sample after static failure presents a delamination at the interface between the 0° layer and the 60° layers. However, t he extent of the delamination area is less than the S-01 sample but is still quite marked, Figure 4-9. The failure zone is located close to the tab, as in the previous sample.
The micrographic analysis of the delamination surface leads to the same results obtained for the sample S-01 and therefore also for this sample it is possible to assert that could be some problems in the fibers-matrix interface, although less extent.

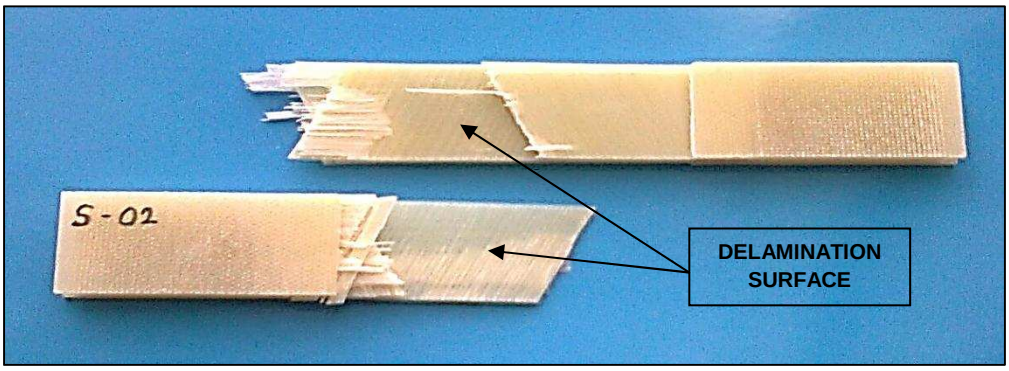

Figure 4-9. Sample S-02 after static failure

4.4.3 Post-failure analysis of sample S-04

The same delamination noted in the previous samples is still present in this specimen, see Figure 4-10. Thus the problem of bonding between the +60° and 0° layer exist even in this case.

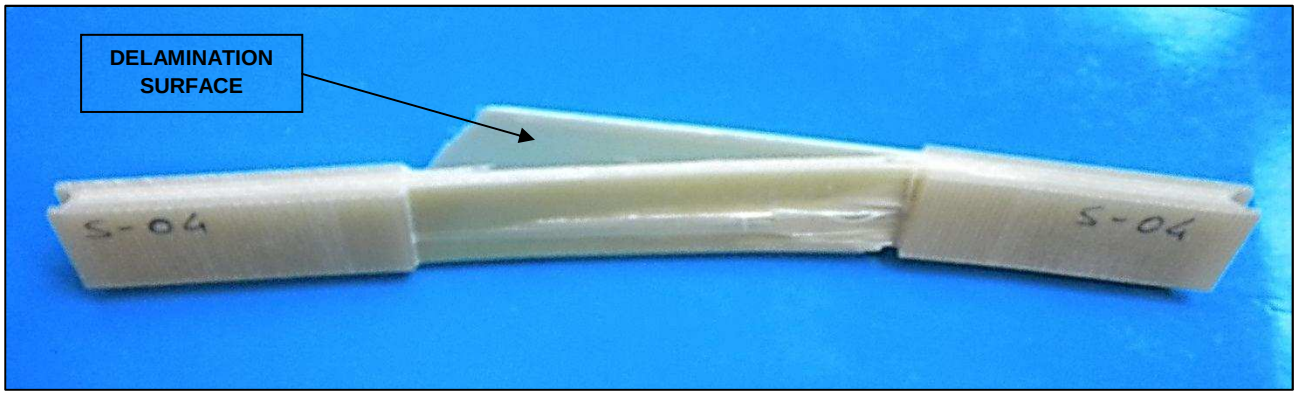

Figure 4-10.Sample S-04 after static failure

4.4.4 Post failure analysis of sample S-05

After static failure, Figure 4-11, the delamination seen in the previous specimens is absent, also the sample is not broken in two parts. The fracture zone is positioned in the center of the sample and is possible to glimpse the flat separation of the off-axis layer. This test doesn't highlights evident material defects due to the production process.

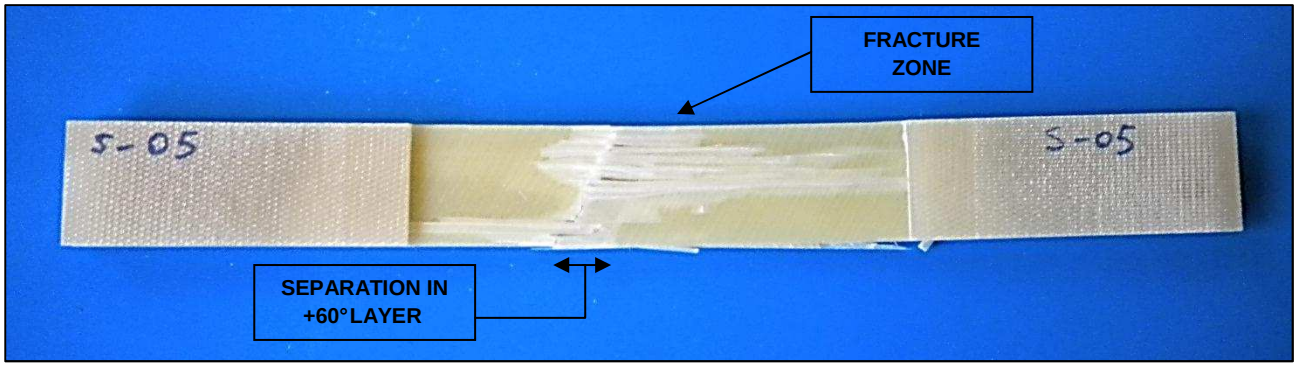

Figure 4-11. Sample S-05 after static failure

4.5 DISCUSSIONS

By the experimental static tests the material elastic properties has been found. In particular, considering the average value of the four tests:

Young's Modulus:	18000 MPa	
Ultimate stress:	325 MPa	*4.1*
Ultimate strain:	0.0246	

Moreover, the post-failure analysis has shown that under static loading the material has a non-perfect interface between the 0° and +60° layer with an extent delamination. This is could be connected with a production process defect or with a problem on the fibers-matrix interface. However, in the last test with the sample S-05 this problem disappears. Concluding, maybe a manufacturing defect exits in the material but is not extended to all samples. Anyway, taking into account this aspect all the other samples are considered suitable for the future testing.

Finally, for clarity, a stress-strain curve was compared with the picture of the sample taken during the test. In the point of view of the damage, the zone before the failure is the most interesting; the following chart in Figure 4-12 shows a zoom of the least part of the complete curve of the sample S-02. Each visible peak is in relation with a certain amount of damage in the materials (cracks) and the corresponding pictures are illustrated. The visible cracks are oriented at 60°, which means that with a static load the off-axis layers break first.

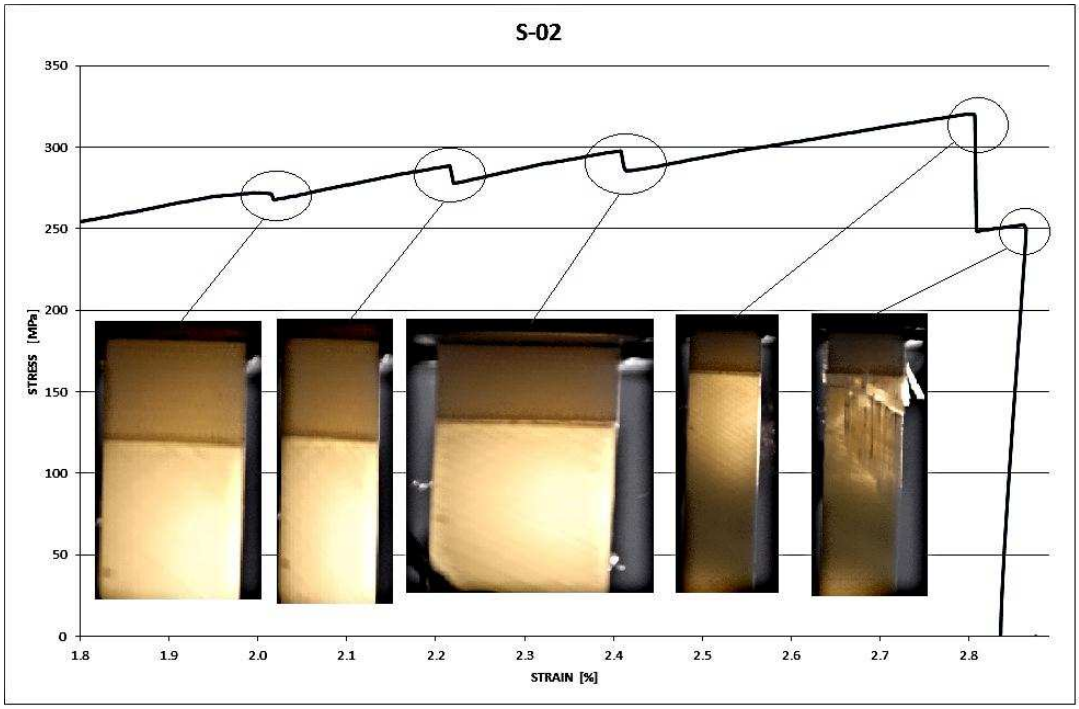

Figure 4-12. Part of stress-strain curve closed to failure of sample S-02. For each peak there is the corresponding acquired test image

5 EXPERIMENTAL FATIGUE TEST

5.1 GENERALITY

This chapter describes the experimental investigation on the fatigue behavior of the material UE400-REM with lay-up $[0/(+60)_2/0/(-60)_2]_s$. This is the most important part of the project, since the entire project is based on these tests. As already stated, a composite laminate under fatigue loading present a multiple cracking condition that increase until failure and consequently the elastic properties decay. This phenomenon regards in particular the off-axis layers in which cracks can easily initiate and propagate in the matrix along the fiber direction. In particular, cracks oriented at 60° respect to the applied load are subjected to a mixed Mode of cracking (I+II), although is prevalent Mode I. The aim is to determine the damage evolution of the off-axis layers, with respect to the number of cycles, in terms of crack density by varying the strain level applied. In practice, cracks are observed by two systems. The first consist in a continuous images acquisition of the sample during the test by a camera; after these images are analyzed to reconstruct the crack density trend. Instead, the second system consist in an analysis under microscope of the polished edge of the sample after the test, in this way it is possible to determine the final crack density with more accuracy. It is important to distinguish the layer with opposite orientation (+60° and -60°) in order to highlight a possible thickness effects. Moreover, the stiffness degradation will be monitoring during the tests to control the continuous decay of the elastic properties.

5.2 SAMPLES PRE-ANALYSIS

As explained in the previous paragraph, the damage analysis was conducted also through a microscope observation of the polished samples after each fatigue test. It is important to consider that if the polishing is done after the test (when the material is already cracked) the possibility to generate new cracks with this operation would be very high; consequently the results of final crack density could be altered. Thus, the polishing operation for all samples was done before to start the tests; Figure 5-1 and Figure 5-2.

Furthermore, in order to ensure that the material is free from defects due to the production process, before starting the fatigue tests one sample polished along the thickness were examined under the microscope. One of the main defects of composite materials is the presence of porosity that may lead to false the results of the tests, because the porosity indicates lack of material. The easiest way to see the presence of porosity is the micrographic analysis, which allows observing the number and extension of porosity.

Figure 5-1. Polishing machine used for the samples preparation

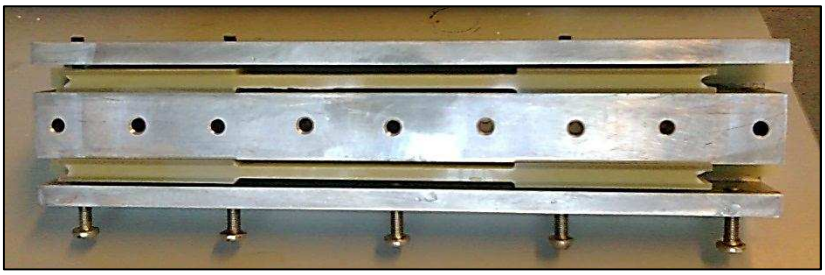

Figure 5-2. Detail of the gripping system of the polishing machine

5.2.1 Micrographic analysis

Through an optical microscope the polished edge of a sample was observed through the entire length to look for any defects and porosity. An example of image obtained is shown in Figure 5-3 and Figure 5-4.

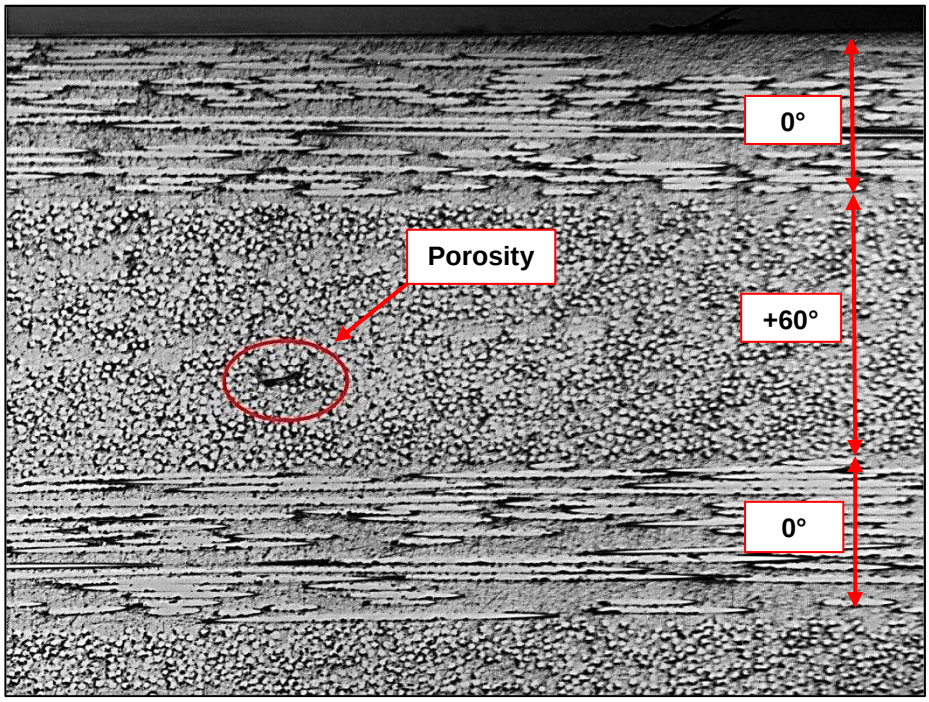

Figure 5-3. Optical microscope image of +60° layer. Presence of porosity is visible.

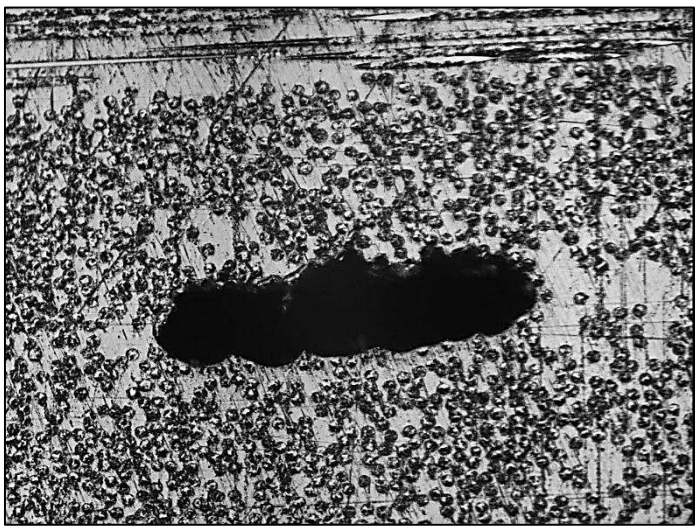

Figure 5-4. Enlargement of the porosity in the +60° layer

These images allow verifying that actually there is some porosity in the material. However, controlling the entire length of the sample, the number of porosity is very limited and therefore acceptable. This condition is related to a normal presence of defects due to the production process with infusion sack technology; then it is impossible to think of having

samples completely without defects. During the fatigue test shouldn't be any problems related to the material porosity.
Moreover, considering the delamination problem come out from the static tests (see paragraph 4.4.1) the interface between layers at 0° and +60° was controlled along the entire length of the sample. As can be seen from Figure 5-5, the interface is good and hasn't visible defects of no-bonding.

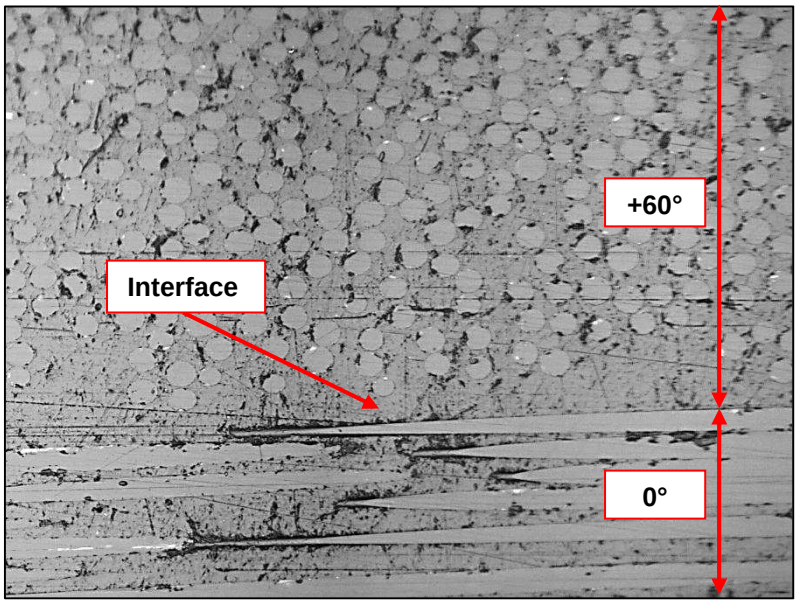

Figure 5-5. Microscope image of interface between the 0°and -60°layers

5.3 TEST DESCRIPTION

This section describes how the fatigue tests were conducted. The machine and equipment used are:

- Machine hydraulically operated for uniaxial fatigue loading INSTRON 8501
- Load cell of 200 KN INSTRON H0022
- Uniaxial extensometers INSTRON 2620-602 ±2.5 mm
- Camera NIKON D200

The codification used for the fatigue samples is for example: *F-01-P*. Where *F* indicates fatigue test, *01* indicates the serial number and *P* indicates that it is a polished sample.

The tests have been conducted by choosing the applied strain level as a varying parameter. Being the tests in load control, the load level was determined by the imposed strain and the elastic modulus. The starting strain value was 0.8%. Once it is set on the machine with the dimensions of the sample's section, the machine applies a static preload to estimate the stiffness of the specimen. The machine's software auto-calculates the max

stress and thus the max load, to be applied to achieve the chosen strain level. Then, through the load ratio imposed, the software calculates the minimum load to be applied.
The cycle frequency is set to 5 Hz, while the load ratio selected is 0.1. The machine stops automatically when a certain safety value of displacement is exceeded and when the number of cycle reaches 2000000.
Figure 5-6 and Figure 5-7 shows the system used in fatigue tests. The main system used in this project to evaluate the crack evolution is based on a continuous images acquisition of the sample during the test. To be able to see well enough the damages in the sample two concentrated lights are mounted behind the sample, thus the cracks are more visible taking advantage of the semi-transparent material.
The main system used in this project, to monitor the damage evolution, consist in a camera with automatic acquisition images mounted in front of the sample that at regular intervals (for example every five minutes) takes a picture of the component and records the corresponding time. The images have been used after the test to reconstruct the evolution of the damage with respect to the number of cycles.

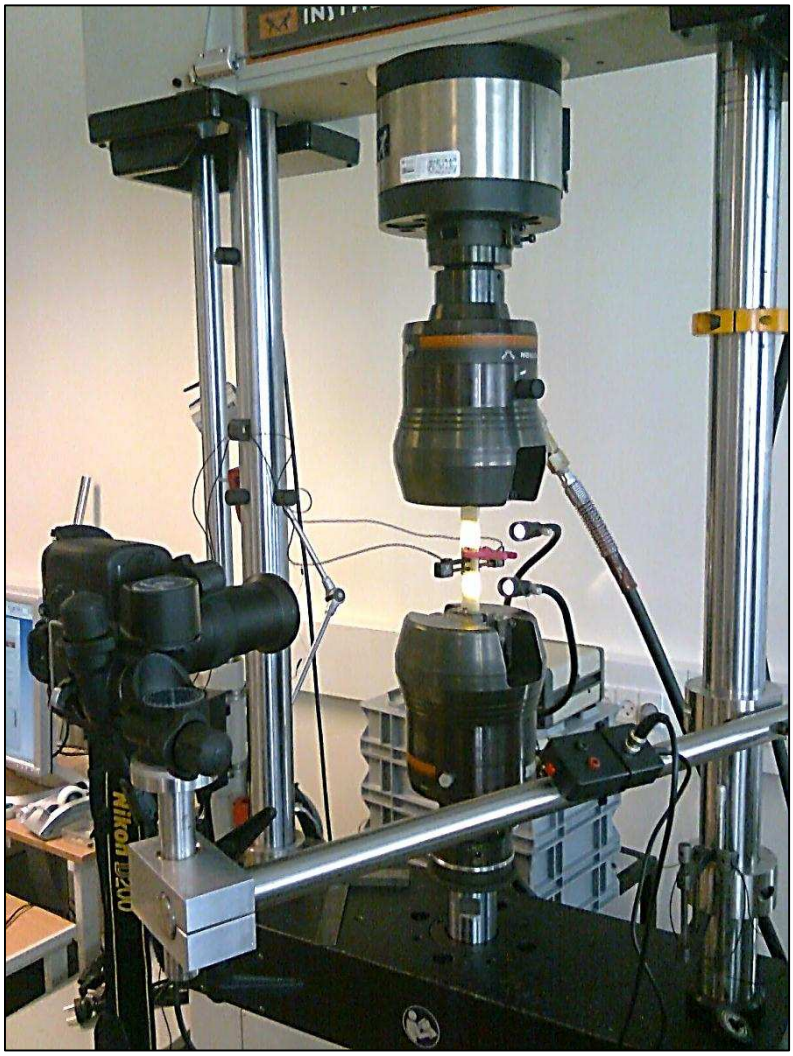

Figure 5-6. Equipment used for fatigue test

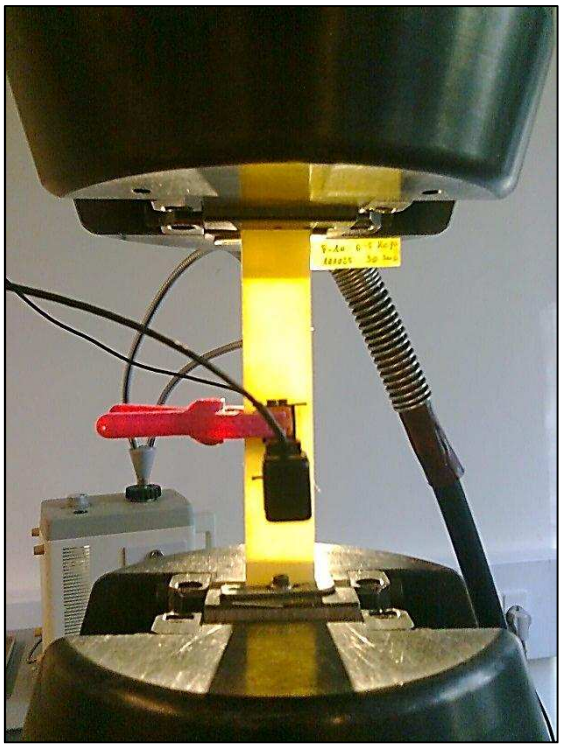

Figure 5-7. Lighted sample through the light system used during the tests

5.4 TEST RESULTS

In order to obtain more reliable results, every test was repeated twice, except for 0.4% strain level; in this way two test groups were identified. The results obtained from the fatigue tests are summarized in Table 5.1 and Table 5.2. For each sample the identification code, the initial strain value imposed, the maximum and minimum load level, the initial stiffness and the run out number of cycles are given.

FIRST TEST GROUP							
CODE	ε_{MAX} [%]	F_{MAX} [N]	F_{MIN} [N]	σ_{MAX} [MPa]	σ_{MIN} [MPa]	E_I [MPa]	$N_{run\ out}$ -
F-01-P	0.8	14288	1428	144.1	14.4	18010.3	2000000
F-02-P	1.0	15848	1584	166.4	16.6	16703.4	728796
F-03-P	0.9	15397	1539	158.0	15.8	17564.3	839410
F-04-P	0.5	8386	836	87.6	8.7	17540.2	772143
F-05-P	0.6	10550	1055	107.8	10.7	17995.5	1713924
F-06-P	0.7	12145	1214	124.1	12.4	17747.7	851807
F-07-P	1.1	18313	1831	190.8	19.1	17366.1	199334
F-08-P	0.4	7011	701	73.4	7.3	18364.8	2000000

Table 5.1. Fatigue tests results about the first test group

SECOND TEST GROUP							
CODE	ε_{MAX} [%]	F_{MAX} [N]	F_{MIN} [N]	σ_{MAX} [MPa]	σ_{MIN} [MPa]	E_I [MPa]	$N_{run\ out}$ -
F-11-P	0.8	13583	1358	139.4	13.9	17701.7	2000000
F-12-P	0.7	11855	1185	121.9	12.2	17742.3	861745
F-13-P	0.6	10540	1054	105.4	10.5	17716.8	750000
F-14-P	0.5	8861	886	89.5	8.9	17861.8	1321723
F-15-P	0.9	15479	1547	165.1	16.5	18435.3	516847
F-16-P	1.0	16641	1664	171.8	17.8	17254.1	887047
F-17-P	1.1	18255	1825	185.7	18.5	16999.5	452808

Table 5.2. Fatigue tests results about the second test group

5.4.1 DEGRADATION STIFFNESS

During the tests samples stiffness trend was obtained by continuous measuring of stress and strain. The first one was given by the load cell, instead the strain can be measured by the extensometers (Strain average slope) or by the displacement sensors of the machine (Position slope).The strain measured by the extensometers concerning only to the part of the sample included between their arms. This approach is very precise because the strain is measured directly on the sample, even if the controlled area is limited. On the other hand the strain measured by the sensor, placed on the gripping heads of the machine, leads to control the entire length of the sample. However this approach is less precise that the previous one, because the strain measured is the sum of that of the sample and that of the gripping heads. Of course, the stiffness of the heads is extremely high compared to that of the sample so its contribution is limited, although ever present.
Basing on that a crack generation produces a stiffness variation, it is possible to connect the presence of damages with the stiffness degradation. Considering this aspect, the strain measured by the extensometers allows to detect only the cracks that propagate in the area between to the arms with high accuracy. Instead, the strain measured by the sensors of the machine allows to detecting every cracks that propagate in the sample but with a low accuracy.

In general the two curves of stiffness degradation, constructed with the strain average slope and the position slope, are never overlapped, i.e. the value of stiffness measured is not the same. The number of damages detected (by a stiffness degradation) through the extensometers are less than those detected by the machine's sensors, because the control area is much smaller. But what matters is the fact that if the two curves are parallel with the same trend; i.e. the damages are evenly distributed along the entire length of the sample. Then, in this case to consider only the value measured by the extensometers (more precise) is the best choice.

The degradation stiffness of each sample can be gathered together to highlight the effect of the applied strain level; in the following charts the stiffness degradation comparison regarding the first test group is presented, Figure 5-8 and Figure 5-9.

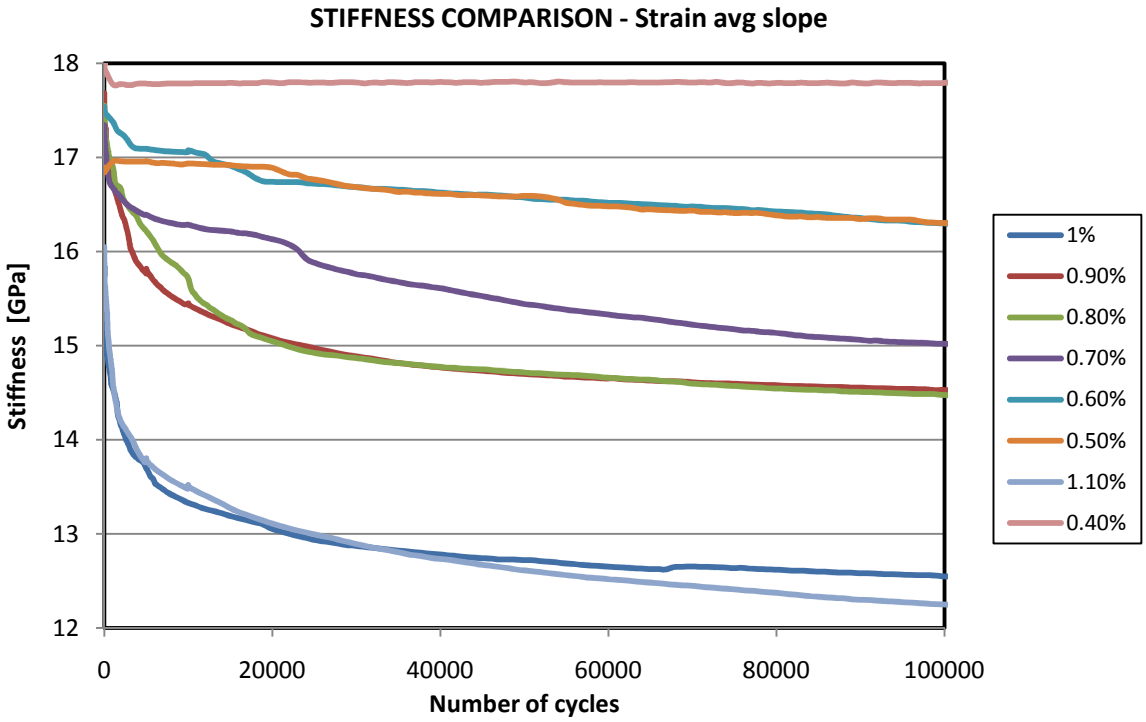

Figure 5-8. Stiffness degradation at various strain level through the strain average slope, regarding the first test group

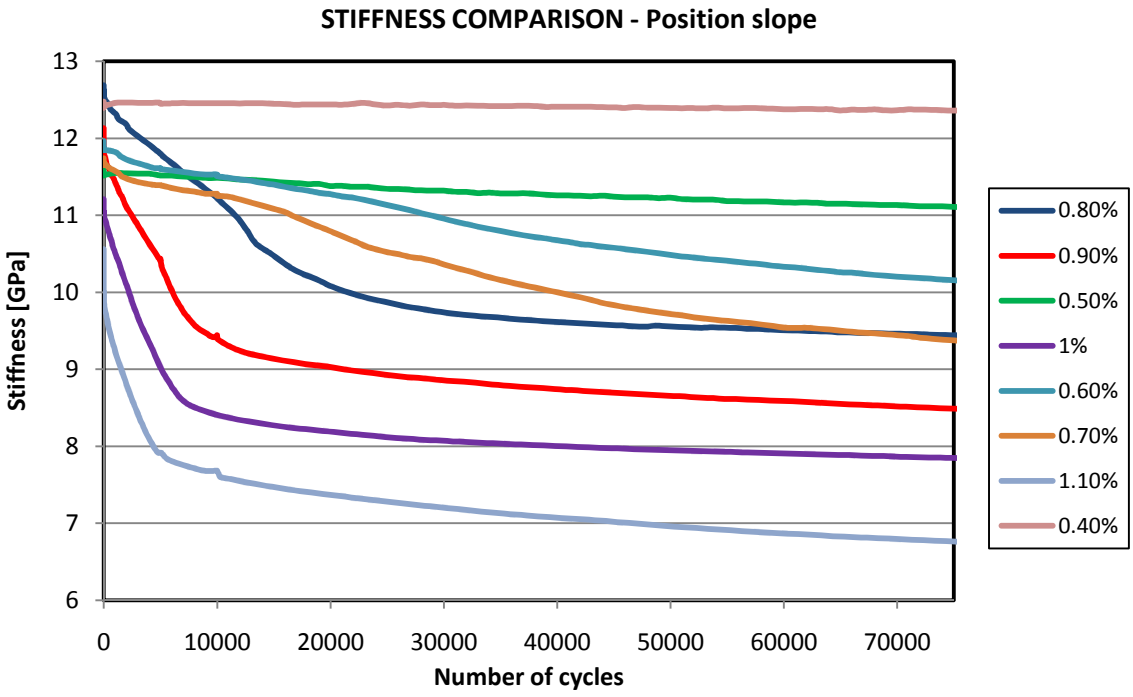

Figure 5-9. Stiffness degradation at various strain level through the position slope, regarding the first test group

Observing the previous charts, the stiffness has a different degradation by varying the strain level. For a high level of strain the degradation is very fast and as the level is reduced the speed degradation decreases up to the 0.4% of strain where the stiffness remains almost constant. Moreover, the stiffness reaches a constant value in all strain level after a certain number of cycles. By experimental observation as the number of damages (cracks) in the off-axis layers increases the stiffness decreases; after a certain number of cycles the layers are totally cracked and they don't carry the applied load. This condition, where only the on-axis layers carry the load, corresponds to the constant trend of stiffness and it remains until failure occurs. The purpose of the present work is focused on the off-axis layers damaging, for this reason the further analysis are going to be concentrated on the first interval of cycles where the stiffness reaches the constant condition as reported in the previous charts in Figure 5-8 and Figure 5-9. However, in order to observe the behavior of each sample until the end of each test, it is possible to normalize the stiffness respect to its initial value and to normalize the number of cycles respect to its final value. In this way the entire stiffness trends of each test can be gathered together in the same scale as reported in Figure 5-10. The reason of this normalization is that for every test the run out numbers of cycles are very different to each other especially for high and low applied strain level.

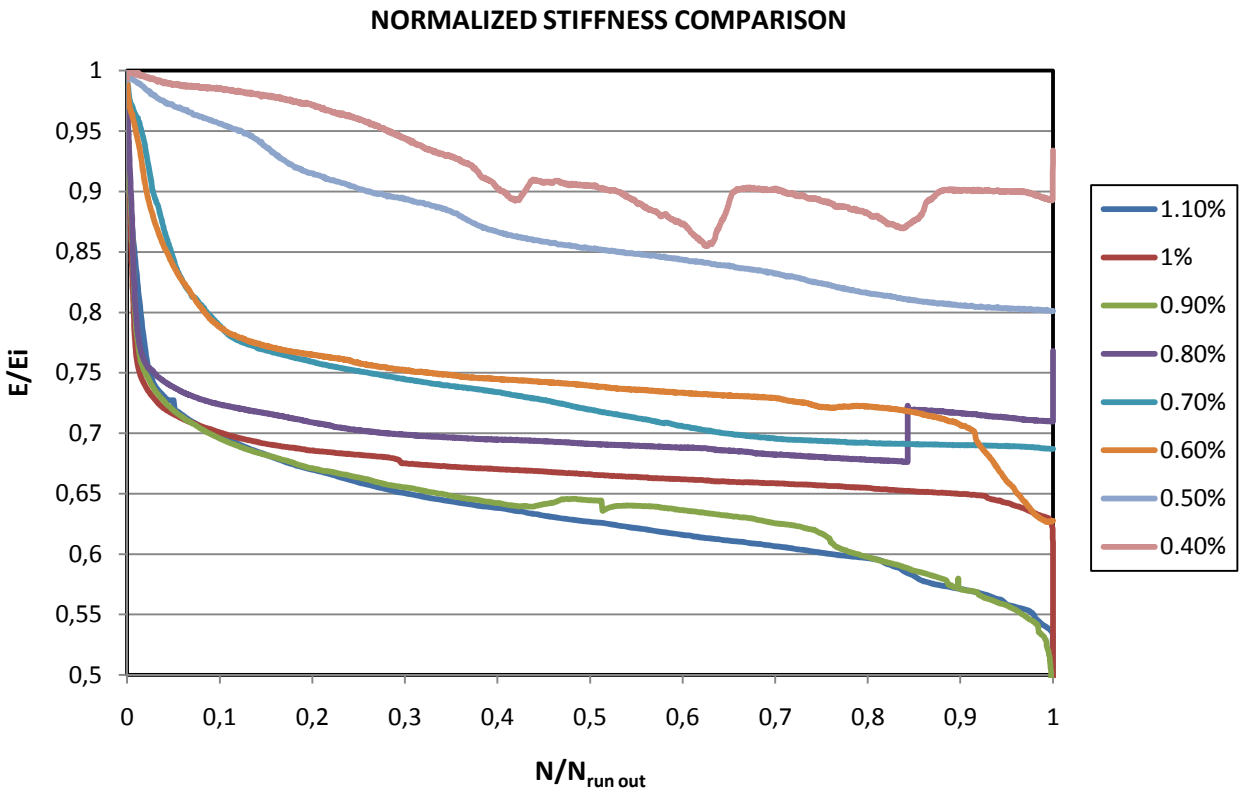

Figure 5-10. Normalized stiffness degradation comparison at various strain level through the strain average slope and regarding the first test group

5.4.2 CRACK DENSITY TREND

Regarding the damage evolution by observing the surface, through the system illustrated in the previous paragraph 5.3, crack density on the off-axis layers was monitored during the test. An example of acquired picture is in Figure 5-11, where it is possible to observe that cracks propagate in +60° and -60° layer; the opposite orientation is very useful in order to distinguish cracks that belong to different off-axis layers.

Figure 5-11. Example of acquired image during the tests at 0.8% strain level. The crack at +60° and -60° are distinguishable.

By the automatic images acquisition the damage evolution was reconstructed as the crack density with respect to the number of cycles. In particular the crack density was calculated as number of cracks per length. The following charts in Figure 5-12, Figure 5-13, Figure 5-14 and Figure 5-15, present the crack density trend in all strain level applied, distinguishing the two off-axis layers.

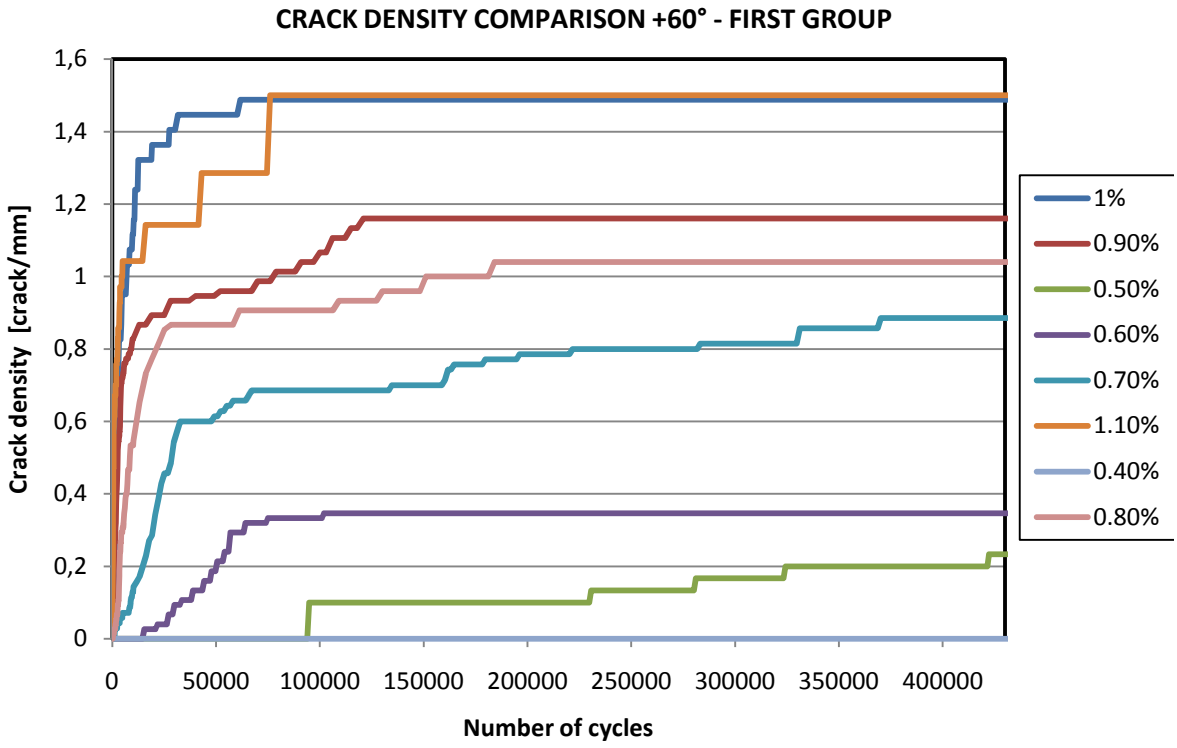

Figure 5-12. Crack density trend respect to the number of cycles in +60° layer regarding the first test group

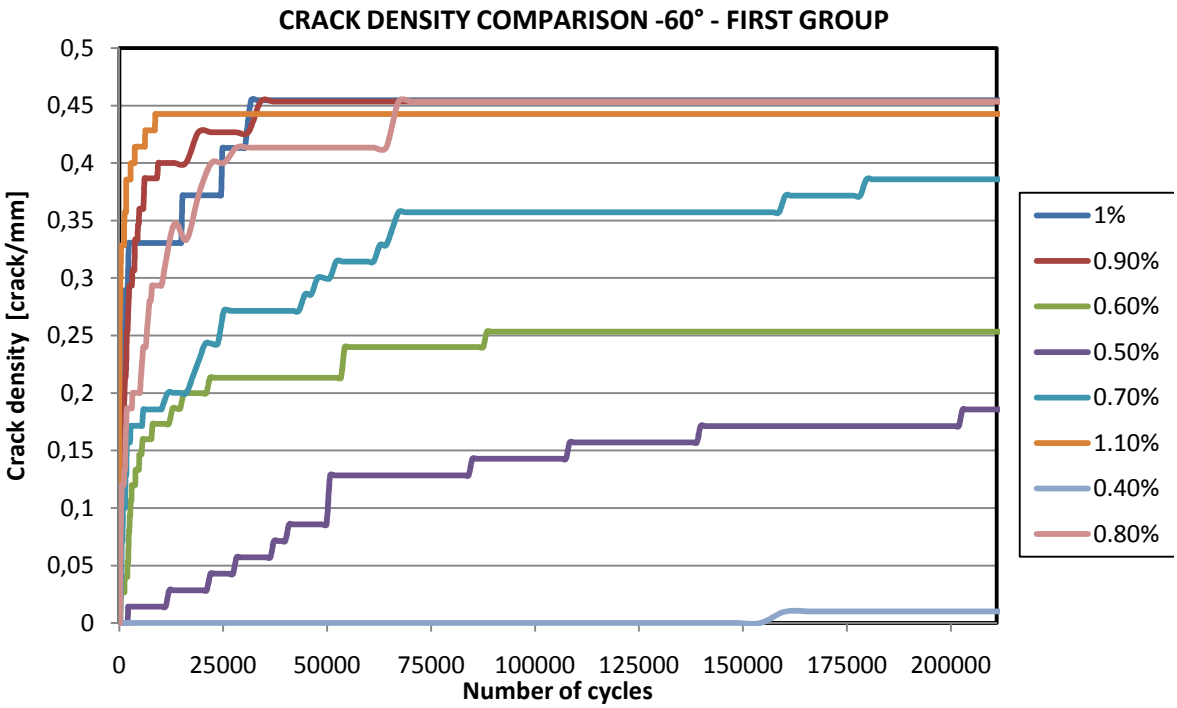

Figure 5-13. Crack density trend respect to the number of cycles in -60° layer regarding the first tes t group

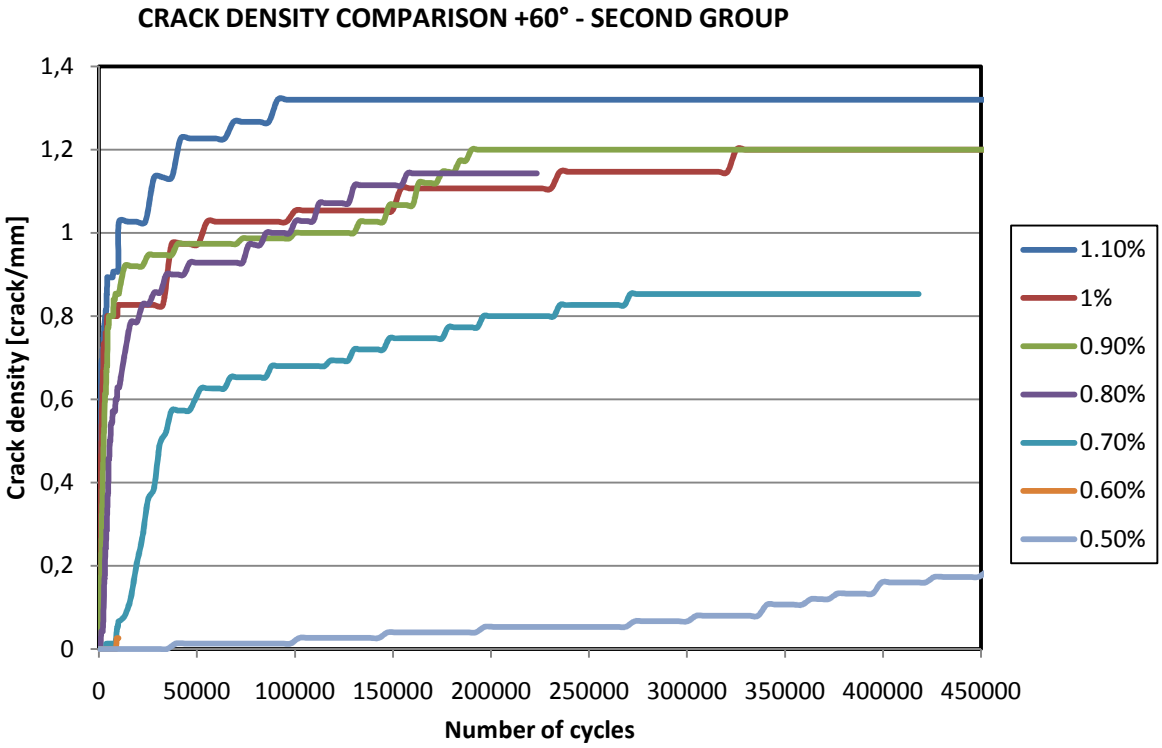

Figure 5-14. Crack density trend respect to the number of cycles in +60° layer regarding the second te st group

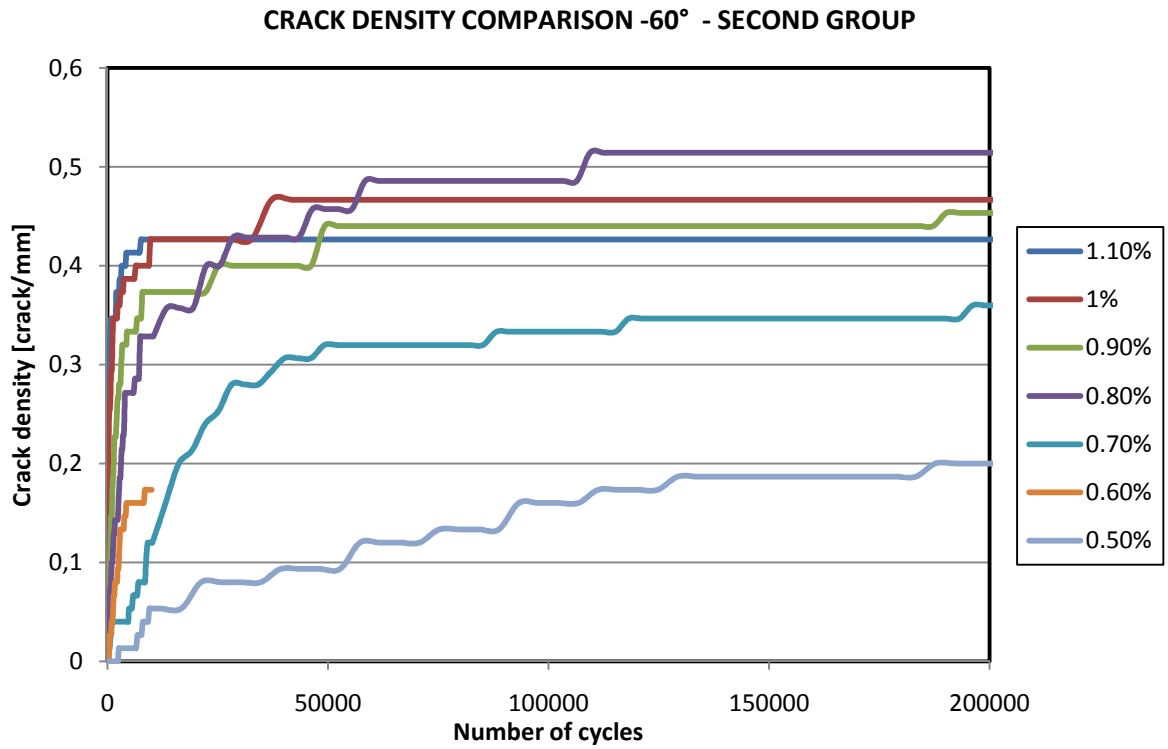

Figure 5-15. Crack density trend respect to the number of cycles in -60° layer regarding the second te st group

Observing the previous charts for both layers the higher is the strain level, the higher is the crack density and the higher is the curve slope. This means that with high strain level cracks propagate very quickly and so crack density increases very fast. Another important observation is that the crack density reaches a constant condition after a certain number of cycles that varies depending on the strain level applied. In this condition the number of cracks is saturated and doesn't increase more, this means that the layers are totally damaged and they don't carry any load.

Two important differences can be observed between +60° and -60° layers. The first one is that with all strain level the values of crack density in +60° layer is more or less double with respect to the one of -60° layer. The second one is that the condition of saturation in -60° layer is reached at a number of cycles double with respect to the +60 layer. These two differences can be due to the different thickness of the +60° and -60° layers. In fact, the constraint condition on the off-axis layers it is the same and also the load applied. Thus, the different behavior could be explained by a thickness effect.

Another experimental observation was that with almost all strain level applied the cracks in -60° layer propagates immediately through the entir e sample width. On the other hand, in +60° layer cracks need several cycles to propagate with the lower strain levels, instead with the higher levels cracks propagates immediately. Also this feature could be explained by the presence of a thickness effect.

Regarding the differences between the first test group and the second one, it is possible to assert that are negligible in an experimental point of view. In fact the values and the trend of crack density are comparable. In this way, the second test group confirms the results of the first one. For simplify, about the subsequent analysis that will be done using only the results from the first test group.

After every test, the polished edge of samples was analyzed under microscope in order to count cracks accurately. The crack density obtained in this way corresponds to the saturation condition because it is calculated when the test is ended, thus at a number of cycles where the number of cracks is constant. The chart in Figure 5-16 shows the results of this analysis.

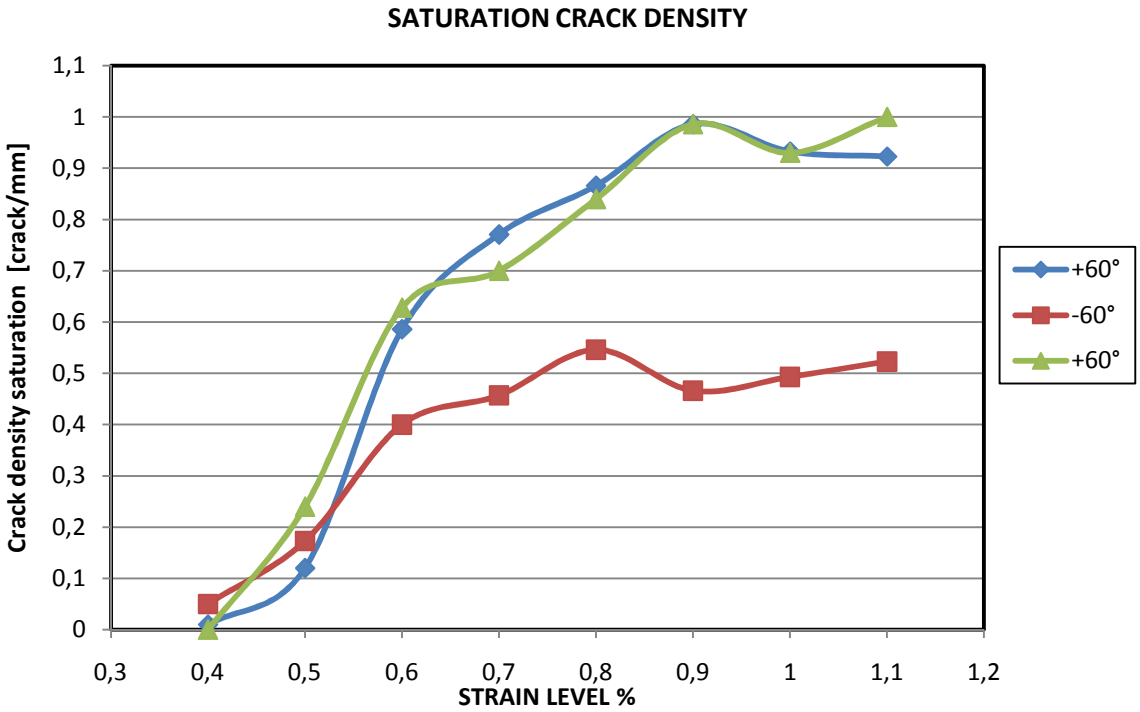

Figure 5-16. Crack saturation trend by the polished edge analysis. First test group

The previous chart highlights the strain level and thickness effects. Every point represents the value of saturation crack density at the corresponding strain level. With respect to the strain level all the layers have the same trend. As the strain level grows the crack density increases until to reach a constant value for high strain level. Also the crack density is very close to zero with 0.4% of strain level, this means that the load applied induces local stress state very closed to the critical value of the material for crack propagation.

The thickness effect is perceptible considering the difference between the +60° and -60° curves. At high strain level the -60° crack density value is almost half respect to +60°. This difference disappears at low strain level. Thus, the thin layer (+60°) presents a number of cracks per length double with respect to the thick one (-60°).
In order to consider the saturation crack density, regardless the thickness layer, the previous chart is plotted in Figure 5-17 normalized with the function *h/L*. Where *L* is the

crack spacing and *h* is the thickness. Only the strain level effect is now highlighted and as expected the three curves have the same trend.

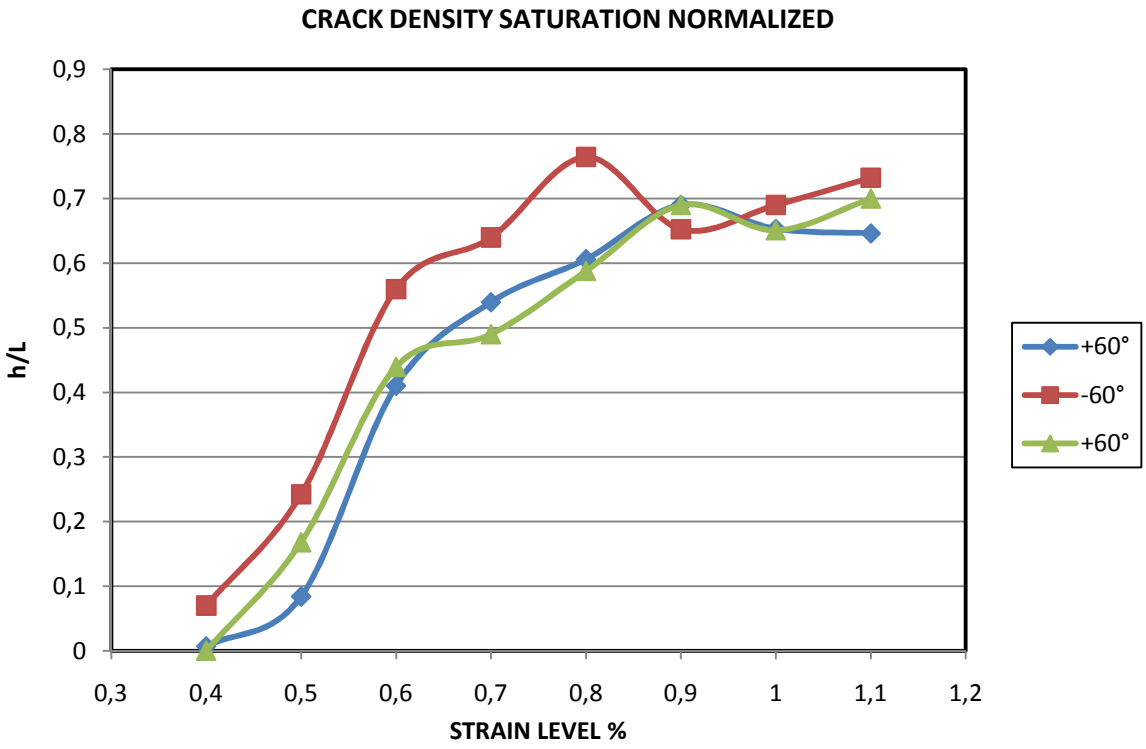

Figure 5-17. Normalized crack density respect to the corresponding off-axis layer thickness. First test group

5.4.3 Micrographic crack analysis

The polished edge of the sample was briefly analyzed under the microscope in order to understand how cracks propagate through the thickness. An image of the entire section of the cracked sample is illustrated in Figure 5-18; it is reported to case at 0.8% of strain level after 2000000 of cycles. First, it is possible to distinguish the different layers, how is indicate in the picture. The +60° layer has an higher number of cracks per length with respect to the -60° and this confirm the diffe rent crack density level obtained from the images analysis. It also interesting to observe that all cracks in the off-axis layers are propagate through the entire layer thickness. The 0° layers appear almost intact and their failure occurs at a very high number of cycles after the crack saturation condition of the off-axis layers.

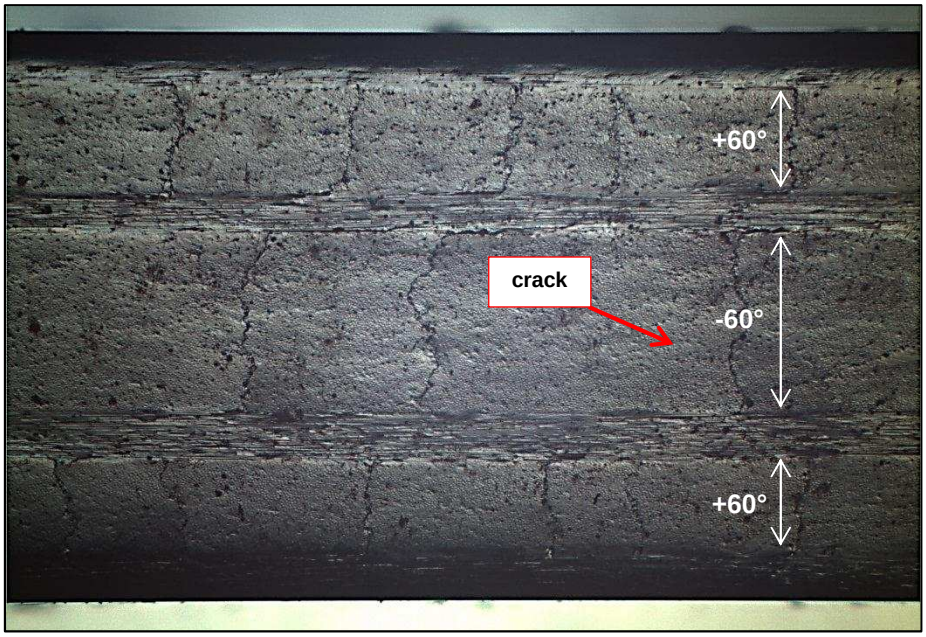

Figure 5-18. Microscope image of the entire polished edge of the sample with 0.8% strain level and at 2000000 cycles. Cracks in the various off-axis layers are distinguishable

In Figure 5-19, referring to the case at 0.9% of strain after 839410 cycles and zooming on the +60° layer, it is possible to observe a delamin ation between the 0° and the -60° layers. However, this delamination it is not present in all -60° cracks and relates more to the tests at high strain level. Another example of delamination between 0° and -60° layers is illustrated in Figure 5-20. Moreover, in Figure 5-19 it is possible to observe an internal delamination in the 0° layer that may be a sign of its initial failure.

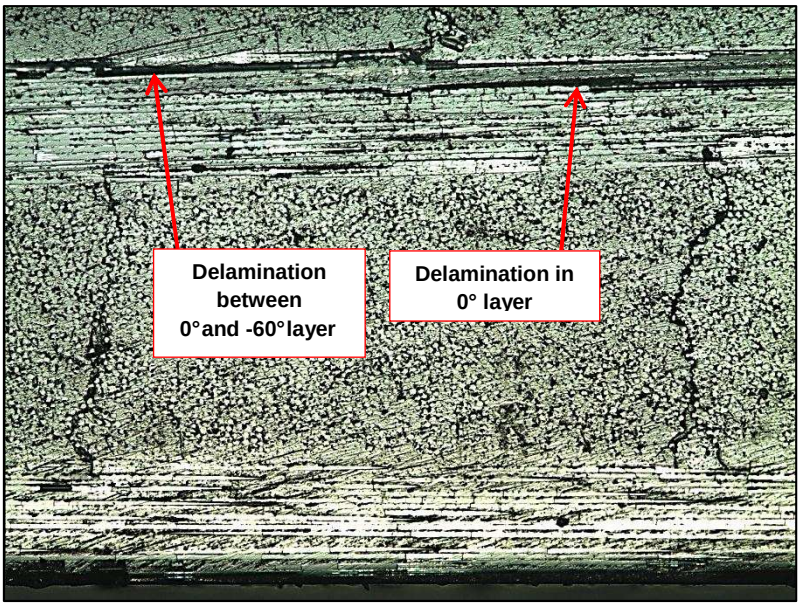

Figure 5-19. Microscope image of 0°and +60°layer with 0.9% strain level and at 839410 cycles. Different types of delamination are highlighted

Figure 5-20. Enlargement on the -60°layer. The del amination between 0°and -60°layer is highlighted

6 DAMAGE ANALYSIS

6.1 GENERALITY

In this chapter a damage analysis regarding the off-axis layers is presented in order to investigate the different effects that have been observed during the experimental tests and that are reported in the previous paragraph 5.4. This analysis is based on a theoretical model that could be useful to explain and to predict the damage evolution. In particular, wishing to focus on the cracks propagation, to conduct this analysis a fracture mechanics approach is used. The crack propagation condition is rather complicated because there is the presence of a mixed Mode cracking in orthotropic material; in particular cracks have a preferential propagation path along the fibers direction. Finally, a comparison with the experimental results was done in order to verify the reliability of the theoretical model.

6.2 TUNNELING CRACKS ANALYSIS

The samples consisted of four groups of layers with different orientation. Two at 0° with one ply, one at +60° with two plies and one at -60° with four plies; all doubled symmetrically. Analysis is focused on the off-axis layers which are bound externally by the 0° layers. For this reason, we speak of tunneling c racks in the off-axis layers. In agreement with the aim of this project, it is certainly important to understand which relations control the crack density and its evolution. To be precise, we'll talk about crack spacing to be consistent with the terminology used in the theoretical model that is now exposed.
The analysis for multiple tunneling cracks in layered material developed by Hutchinson and Suo (1) is considered, in order to analyze strain level and thickness effects on the crack density. To apply this model, the off-axis layers with opposite orientation are considered separately as an inner off-axis block between two 0° layers, see Figure 6-1. Considering a set of cracks in the inner layer with spacing *L* and with equal extension along the sample width, in fatigue case it is valid:

$$\frac{\bar{E} \cdot \Delta G_{ss}}{\Delta\sigma^2 \cdot h} = f_{(h/L)} \qquad 6.1$$

Where, h is the cracked layer thickness, $\Delta\sigma$ is the applied load range, $\bar{E} = E/(1-\nu)$ with E and ν are Young's modulus and Poisson's ratio respectively, L is the crack spacing. The function f is directly connected to the normalized crack density h/L and represents how

we want to find in order to correlate elastic properties, geometrical features and loading applied to the crack density.
It is important to consider that the present model was developed for cracks under static pure mode I with isotropy material; in this project cracks grow under cycling mixed mode (I+II) and the material is orthotropic. For this reason it is very important to calibrate the model with our conditions. In particular, Young's modulus was considered in direction perpendicular to the fibers (material direction 2) because cracks propagate in the matrix along fibers direction. Thus, elastic properties of the matrix control the crack propagation. For this project, a considerable approximation of the present model is that the material's shear elastic properties aren't considered and for sure this can influence the accuracy of the final results.

ΔG_{ss} is the steady-state energy release rate along the crack front; i.e. after the crack length exceeds few times the layer thickness, the crack front doesn't change its shape and the propagation reaches a steady-state condition. The expression of G_{ss} is the following,

$$G_{ss} = \frac{1}{2h}\int_0^h \delta(z)\cdot\sigma(z)\,dz \qquad 6.2$$

With σ is the nominal stress applied and δ is the displacement profile in plane strain condition, see Figure 6-1.

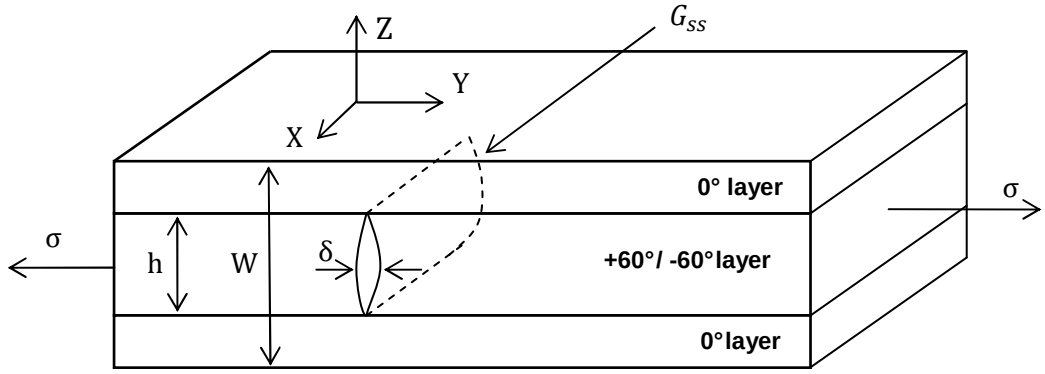

Figure 6-1. Crack opening scheme

How is well known, the steady-state energy release rate corresponds to the J-Integral when the crack length reaches a value equal to few times the layer thickness. This is very useful in order to evaluate G_{ss} in vary conditions by using a finite element model that gives directly J-Integral along the crack front. Thus, in the present project the damage analysis is conducted through the finite elements software ABAQUS 6.10. For more details see Appendix.

6.2.1 Generic application of the model

Initially, a validation of the simulations with ABAQUS is necessary in order to control if the modeling gives correct results in agreement with Hutchinson and Suo's model (1). To do this a crack under pure mode I must be considered, thus for example a 90° layer (with thickness of 0.7 mm) with a central crack between two 0° layers (with thickness of 0.35 mm). For the simulation the material used is UE400 REM with properties reported in the paragraph 3.3. The external stress level applied σ is set at 55 MPa, although this value it isn't important because, at this level what matters it is only verify the reliability of the finite elements analysis with a generic case. Moreover, the crack length is about 5 mm, so the crack is in a steady-state condition and the energy release rate corresponds to the J-Integral along crack front. The G_{ss}, found through the finite elements model, is equal to 0.168943 KJ/m^2; that corresponds to a factor f of 0.75. In Figure 6-2 the solutions of the Hutchison and Suo's model (1) is presented.

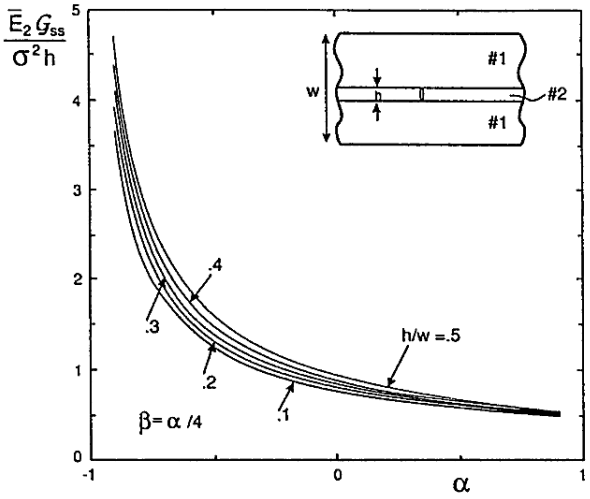

Figure 6-2. Hutchinson and Suo's solution of energy release rate for single crack at different elastic mismatch (1)

Where, α and β are two parameters that quantify the elastic mismatch between the different layers, in particular regarding this case they are defined as:

$$\alpha = \frac{\bar{E}_{1,0^\circ} - \bar{E}_{2,90^\circ}}{\bar{E}_{1,0^\circ} + \bar{E}_{2,90^\circ}} = 0.574 \qquad 6.3$$

$$\beta = \frac{1}{2} \cdot \frac{G_{12}(1-2\nu_{21}) - G_{12}(1-2\nu_{12})}{G_{12}(1-\nu_{21}) - G_{12}(1-\nu_{12})} = 0.033 \qquad 6.4$$

Observing the chart in Figure 6-2 and considering the α and β values in 6.3 and 6.4, the parameter f is about 0.7. Thus, the one found by the finite element model (f=0.75) is in

agreement with the one found by the Hutchinson and Sou's model (1); therefore the ABAQUS simulation is validate. More precisely, the solution in Figure 6-2 refers only for a case with fixed β=$\alpha/4$ and in the case here analyzed it isn't proper like this. However, the parameter β is less important with respect to the α because it represents the shear elastic properties and in the present case the Mode II is not the prevalent.

6.2.2 Model application with single crack in off-axis layers

After the initial and general analysis, the specific lay-up considered in the present project was studied in order first to demonstrate that the parameter f is not directly influenced by the stress applied σ and from the thickness h. An extensive series of finite element analysis was done considering the tick and the thin off-axis layers (-60° and +60°) separately and by varying the stress level applied. Moreover, with the presence of a crack in the off-axis layer, see Figure 6-3, the experimental test conditions were replicated. Naturally, the condition with only one crack corresponds to $^{h}/_{L} = 0$ where L is the crack spacing; this situation is not very realistic because also with static loading the material presents a multiple cracking. Nonetheless, at the moment this approximation is acceptable for the purpose and after the real process of cracking is considered.
The results of these simulations are reported below in Table 6.1 .

+60° LAYER (h=0.7)					-60° LAYER (h=1.4)			
Strain level	**Δσ**	**ΔGss**	**f**		**Strain level**	**Δσ**	**ΔGss**	**f**
%	**Mpa**	**KJ/m^2**	**-**		**%**	**Mpa**	**KJ/m^2**	**-**
0.4	66.06	0.127	0.44		0.4	66.06	0.247	0.43
0.5	78.84	0.180	0.44		0.5	78.84	0.351	0.43
0.6	96.84	0.272	0.44		0.6	96.84	0.530	0.43
0.7	111.69	0.362	0.44		0.7	111.69	0.705	0.43
0.8	129.69	0.488	0.44		0.8	129.69	0.950	0.43
0.9	142.2	0.586	0.44		0.9	142.2	1.142	0.43
1.0	149.76	0.650	0.44		1.0	149.76	1.267	0.43
1.1	171.72	0.855	0.44		1.1	171.72	1.665	0.43

Table 6.1. Finite elements solutions for the energy release rate and the parameter f with a single off-axis crack model.

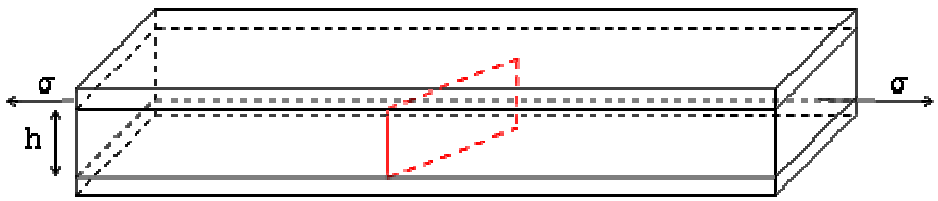

Figure 6-3. Scheme of the layered material in presence of one crack in the off-axis layer

Two important conclusions can be drawn by observing the previous results. First, the parameter f is not sensitive with respect to the applied stress, this is due to the fact that as

the $\Delta\sigma$ raise also the ΔG_{ss} increase and the ratio ${\Delta G_{ss}}/{\Delta\sigma^2}$ remains constant. Next, the parameter f doesn't change by varying the thickness h. This condition is consistent with the theory of Hutchinson and Suo's model (1), which is to express f as a function of the crack density normalized with respect to the thickness $\left({h}/{L}\right)$. For this reason it isn't possible to predict the thickness variation effect on the crack density (or crack spacing) through the parameter f because the two parameters are connected to each other; however the crack density normalized to the thickness $\left({h}/{L}\right)$ is analyzable.

6.2.3 Model application with multiple cracking in off-axis layers

In order to understand the damage evolution regarding the specific lay-up studied in this project, it is now necessary to determine the function f for this specific situation. In fact, as already explain, Hutchinson and Suo (1) calculated f with their model for a case with absence of elastic mismatch between the different layers, with isotropic material and with cracks under pure mode I. Because of the particular lay-up and properties of the orthotropic material, the case analyzed in the present work is different from that considered by Hutchinson and Suo (1).

The parameter f is a function of the crack density normalized with respect to the thickness. Thus, to determine this function some finite elements analysis, by varying the crack spacing, are requested. In this way, for each value of normalized crack density it is possible to determine G_{ss}, and consequently the parameter f, along the crack front of one of the present cracks. As already found, f isn't influenced directly from the external stress applied and from the cracked layer thickness, so these analysis are done only for the +60° layer and with the strain level fixed to 0.8% (that correspond to Δσ=130 MPa). The normalized crack density varies from 0 to 1, and in Figure 6-5 an example of the used ABAQUS model is reported. The results of this analysis are summarized below in Table 6.2.

MULTI-CRACK +60°			
h/L	Δσ	ΔGss	$f_{(h/L)}$
-	MPa	N/mm	-
0	130	0.650	0.582
0.1	130	0.627	0.562
0.2	130	0.478	0.428
0.25	130	0.446	0.399
0.45	130	0.336	0.301
0.7	130	0.185	0.165
0.9	130	0.142	0.127
1.0	130	0.127	0.113

Table 6.2. Finite elements solution for model at different crack density levels

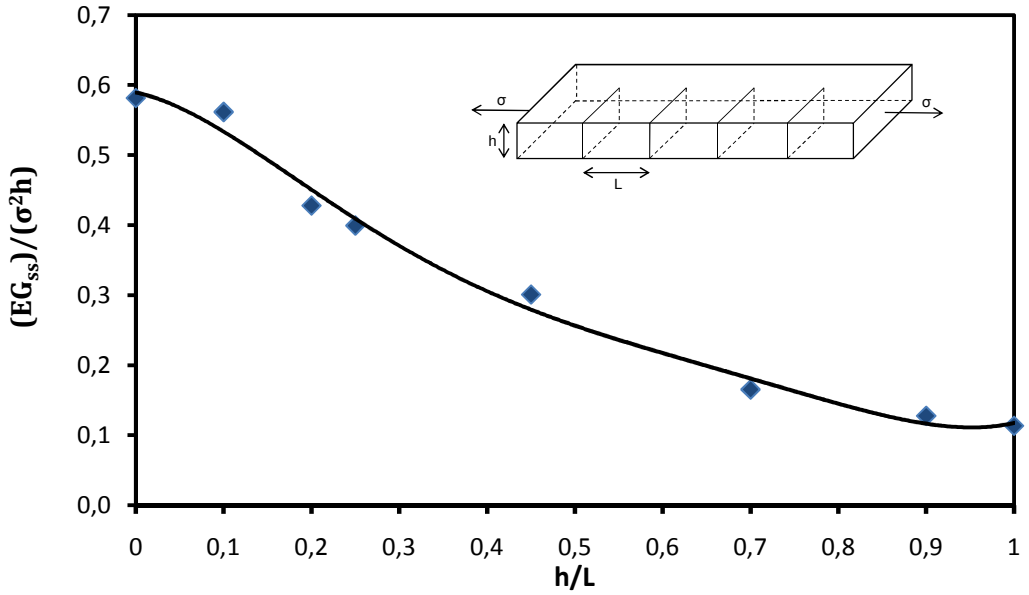

Figure 6-4. Function f trend by varying the crack density. Thickness and applied stress are fixed

In Figure 6-4 the function f, about the off-axis layers, is well known and in this way it is possible to correlate for example the normalized crack density with the energy release rate. It is important to underline that this approach assumes cracks equally spaced and equally extended.

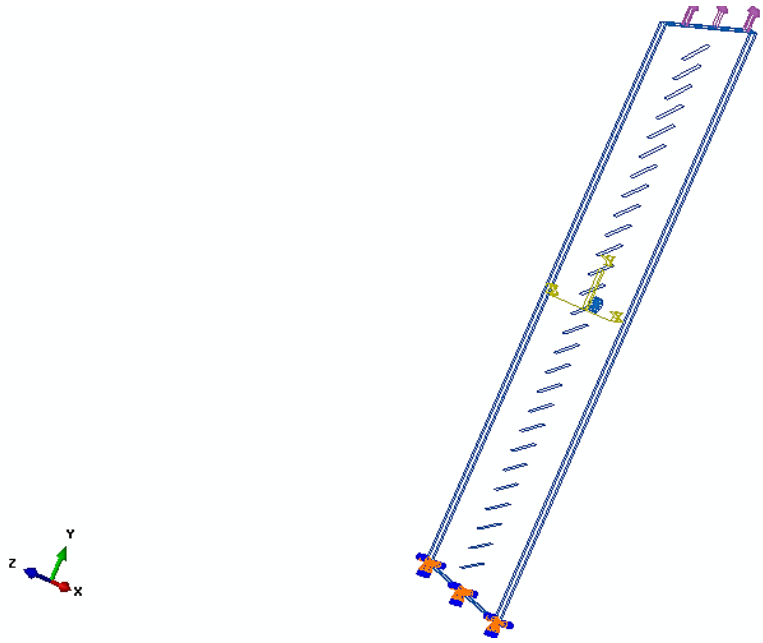

Figure 6-5. Example of Abaqus model with multiple cracking condition in the off-axis layer

A next step was to considering that new cracks can initiate between those already exist in order to replicate the experimental conditions in which the number of cracks increase. The Hutchinson and Suo's model (1) provides to modify the expression of f as below reported.

$$\frac{\bar{E} \cdot \Delta G_{ss}}{\Delta\sigma^2 \cdot h} = 2f_{(h/L)} - f_{(h/2L)} \qquad 6.5$$

This expression is based on the assumption that a new crack nucleate exactly in the middle of two existing cracks already initiated and propagated. For sure this is an approximation with respect to what happen in a real case, because during the experimental tests it was observed that new cracks didn't start exactly in the middle of those already existed and propagated. Anyway, this approximation was accepted in order to find just a correlation between the experimental data and the theoretical approach. This modified model in 6.5 can be used to find a relation between the stress necessary to nucleate a new crack and the normalized crack density. The previous formula 6.5 can be written explaining a dimensionless stress as:

$$\frac{\Delta\sigma \cdot \sqrt{h}}{\sqrt{\bar{E} \cdot \Delta G_{ss}}} = \frac{1}{\left[2f_{(h/L)} - f_{(h/2L)}\right]^{0.5}} \qquad 6.6$$

At this point, varying the crack spacing it is possible to find the corresponding value of the parameter f through the chart reported in Figure 6-4. The other parameters are already known. The desired relation is now calculable, as reported in Table 6.3.

h/L -	(h/2L) -	$f_{(h/L)}$ -	$f_{(h/2L)}$ -	$\Delta\sigma\sqrt{h}/\sqrt{(E\cdot\Delta G_{ss})}$ -
0	0	0.589	0.589	1.30
0.10	0.05	0.533	0.567	1.42
0.20	0.100	0.451	0.533	1.65
0.25	0.125	0.409	0.514	1.81
0.45	0.225	0.279	0.430	2.78
0.70	0.350	0.181	0.336	6.25
0.90	0.450	0.116	0.279	-
1.00	0.500	0.117	0.256	-

Table 6.3. Dimensionless stress by varying the crack density

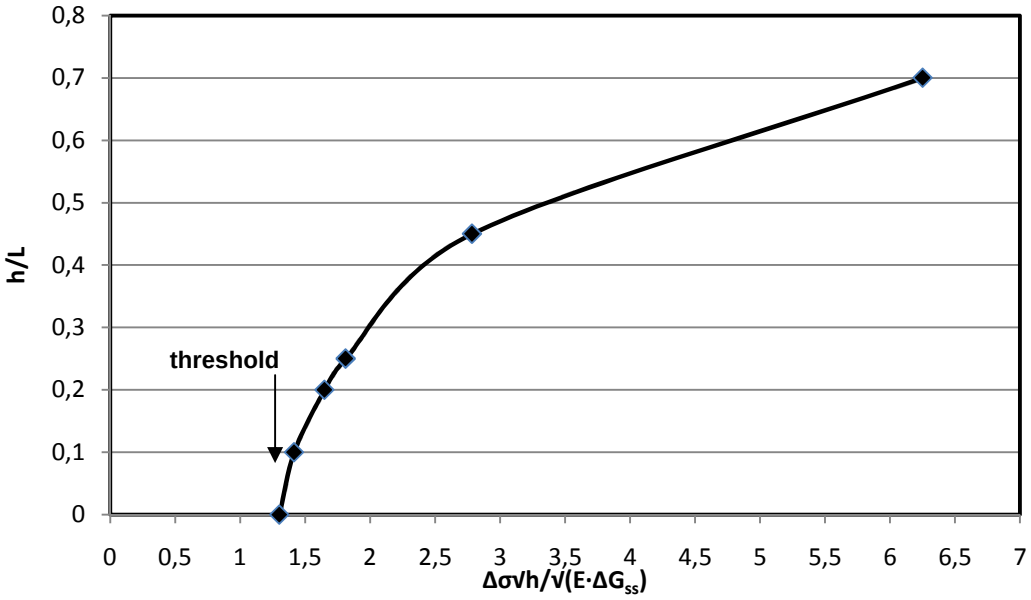

Figure 6-6. Dimensionless stress trend by varying the crack density

In Figure 6-6, plotting the dimensionless stress over the normalized crack spacing, it is possible to observe a threshold value that corresponds to the point at which a single crack can nucleate and propagate. This condition regards the first crack that initiates in the material, being the normalized crack spacing h/L equal to zero. Moreover, when the number of cracks increases this condition is no longer true, because cracks influence to each other by varying the stress state and the energy release rate. In fact, as h/L increase the threshold disappears.

The threshold condition for $h/L \to 0$, is $\Delta\sigma\sqrt{h} \Big/ \sqrt{\bar{E} \cdot \Delta G_{ss}} = 1.302$

This last relation could be useful if the G_{ss} is substituted with the toughness of the material (Γ_c) because in this way it is possible to determine the stress level necessary to generate the tunneling crack with a particular thickness and elastic properties. Specifically for the case analyzed, the previous expression gives:

$$\Delta\sigma = 1.302 \left[\frac{\bar{E} \cdot \Gamma_c}{h}\right]^{0.5} \qquad 6.7$$

It is important to specify that the toughness considered regards the static condition and for sure this introduces an approximation. Anyway, it is possible to consider the condition for the first fatigue cracks is very similar to the static case.

6.3 CRITICAL ENERGY RELEASE RATE

As already explained in paragraph 5.4, an important observation from the experimental tests is that the off-axis layers, with different thickness and opposite orientation (+60° and -60°), show a different crack propagation behavior. Precisely, in the thin layer (0.7 mm) oriented at +60° cracks need se veral cycles to initiate and to propagate through the entire width of the sample for almost all strain levels. As logical to think, at high strain levels the number of cycles requests for the crack propagation is lower than that at low strain levels. On the other hand, in the thick layer (1.4 mm) oriented at -60° cracks propagate immediately with high strain level, instead cracks take some cycles to propagate at low strain levels.

This different and particular behavior is now explained considering only the first crack that appears in the material, in order to bring back the analysis to a static case. The different crack propagation can be highlighted through the energy release rate along the crack front by varying the strain level applied and considering the different layers separately. To do this, it is possible to use the finite elements results from the analysis reported in Table 6.4. Being this analyses related to a static case, the max G_{ss} is considered instead of the ΔG_{ss}, even if these values are very similar being the load ratio equal to 0.1. The values of G_{ss} are now grouped for the +60° layer and for the -60° lay er as below reported in Figure 6-7.By the experimental observations, it is possible to attribute to the different layers the following features:

+60° layer (h=0.7 mm): in this layer only with 1.1% of strain there is an immediate crack propagation; for all the other strain level the crack takes several cycles to propagate through the entire sample width. This means that between 1.0% and 1.1% of strain there is a critical value closed to the condition of static crack propagation.

-60° layer (h=1.4 mm): in this layer with strain from 0.4% to 0.7% the crack propagation takes several cycles; instead with strain from 0.8% to 1.1% the propagation is immediate through the entire sample width. This means that between 0.7% and 0.8% of strain there is a critical value closed to the condition of static crack propagation.

+60°				-60°		
Strain level	**Gss**	**Thickness**		**Strain level**	**Gss**	**Thickness**
%	**KJ/m^2**	**[mm]**		**%**	**KJ/m^2**	**[mm]**
0.4	0.128	0.7		0.4	0.250	1.4
0.5	0.182	0.7		0.5	0.355	1.4
0.6	0.275	0.7		0.6	0.535	1.4
0.7	0.365	0.7		0.7	0.712	1.4
0.8	0.493	0.7		0.8	0.960	1.4
0.9	0.592	0.7		0.9	1.154	1.4
1.0	0.657	0.7		1	1.279	1.4
1.1	0.864	0.7		1.1	1.682	1.4

Table 6.4. Finite elements solutions for the energy release rate and the parameter f with a single off-axis crack model.

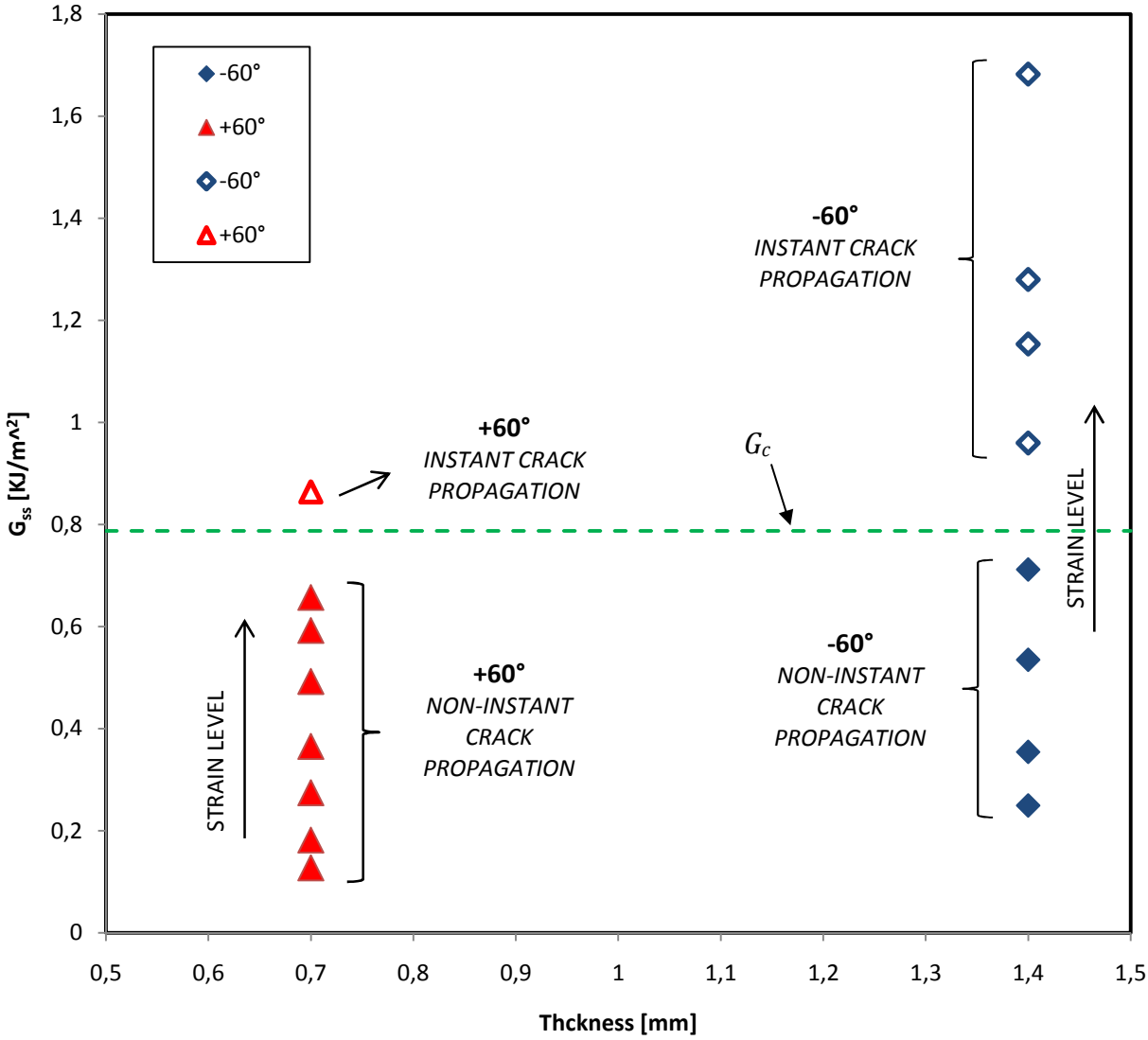

Figure 6-7. Comparison of the off-axis layer with different thickness respect to the energy release rate.

Observing the previous chart in Figure 6-7, it is possible to determine a critical value G_c that distinguishes the instantaneous propagation and the non-instantaneous propagation. This particular value corresponds to the horizontal line in the chart.
Precisely, G_c= 0.7876 [KJ/m^2].

A next step was to consider the relation 6.7 found in the previous paragraph. In particular, the critical stress of crack propagation for both layer could be now determine by replacing Γ_c with G_c. As usual, the critical value of energy release rate has been found with a static approach condition as assumed for the relation 6.7, anyway at the moment this approximation is accepted because we are referring to a condition closed to a static case (first cracks that are generated). In this way it is possible to write:

$$\Delta\sigma_{c,+60^\circ} = 1.302\left[\frac{\bar{E}\cdot \mathrm{G}_c}{h_{+60^\circ}}\right]^{0.5} = 141.8\ MPa \qquad 6.8$$

$$\Delta\sigma_{c,-60^\circ} = 1.302\left[\frac{\bar{E}\cdot \mathrm{G}_c}{h_{-60^\circ}}\right]^{0.5} = 100.2\ MPa \qquad 6.9$$

Where, as already specified, $\bar{E} = E_2/(1-\nu)$.
It is interesting to observe how doubling the thickness (from 0.7 to 1.4 mm) the critical stress decrease by 40%.

6.4 PARIS TYPE CHART

Regarding the non-instantaneous crack in the +60° and -60° layers, the different crack propagation rate by varying the strain level applied was analyzed. In fact, another influence of the thickness could be on the crack growth rate. The off-axis layers are now analyzed separately by observing the sequence of the images acquired during the test. For each strain level, the crack length a and the corresponding number of cycles N were measured step by step until the crack propagates through the entire sample width, see Figure 6-8. As already explained the samples are subjected to a multiple cracking condition, so the crack propagation rate can be influenced by the crack density. This aspect is very interesting but for simplicity it isn't considered in the present analysis. For this reason the crack analyzed by the images is one of the first that initiate in the material; also for each off-axis layers only the strain levels that gives a non-instantaneous propagation are considered. In Table 6.5, Table 6.6 and Table 6.7 the results from the images analysis are reported.

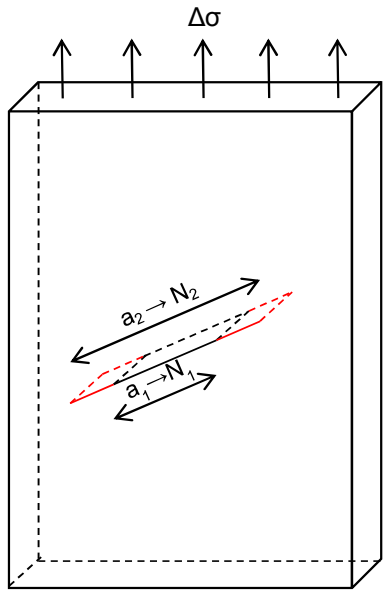

Figure 6-8. Crack propagation in the off-axis layer under cyclic loading

+60° LAYER							
STRAIN 0.4%		STRAIN 0.5%		STRAIN 0.6%		STRAIN 0.7%	
a	N	a	N	a	N	a	N
[mm]	[cycles]	[mm]	[cycles]	[mm]	[cycles]	[cycles]	[cycles]
3	0	4	0	3	0	3	0
4	6000	4	4500	7	3600	4	300
5.6	24000	4	13500	8	13500	4	600
8	30000	4	22500	16	22500	8	1500
9	36000	5	58500	25	40500	19	4100
19	156000	6	148500	30	49500	29	6500
33	456000	10	238500	41	58500	30	8200
35	669800	26	328500	44	94500	40	11200
-	-	32	418500	-	-	44	14200
-	-	37	508500	-	-	-	-
-	-	38	598500	-	-	-	-
-	-	40	688500	-	-	-	-

Table 6.5. Crack propagation in +60°layer with str ain level from 0.4% to 0.7%

+60° LAYER					
STRAIN 0.8%		STRAIN 0.9%		STRAIN 1.0%	
a	N	a	N	a	N
[mm]	[cycles]	[mm]	[cycles]	[mm]	[cycles]
4	0	4	0	6	0
8	450	11	2880	18	300
17	1950	15	4380	23	600
24	3300	25	4980	28	900
27	4400	32	5180	30	1200
31	6800	36	5780	44	2100
35	8300	39	6380	-	-
44	11500	41	8180	-	-
-	-	44	8980	-	-

Table 6.6. Crack propagation in +60°layer with str ain level from 0.8% to 1.1%

-60° LAYER							
STRAIN 0.4%		STRAIN 0.5%		STRAIN 0.6%		STRAIN 0.7%	
a	N	a	N	a	N	a	N
[mm]	[cycles]	[mm]	[cycles]	[mm]	[cycles]	[mm]	[cycles]
2	0	8	0	16	0	8	0
10	6000	18	2150	24	200	14	150
14	12000	21	3350	32	400	28	450
19	18000	34	7000	44	800	44	750
26	24000	44	16000	-	-	-	-
31	30000	-	-	-	-	-	-
33	36000	-	-	-	-	-	-
44	42000	-	-	-	-	-	-

Table 6.7. Crack propagation in -60° layer with str ain level from 0.4% to 0.7%

Through the results in the previous tables it is possible to plot the crack length over the number of cycles for each strain level, see Figure 6-9 and Figure 6-10. Subsequently, the slope of each curve is determined by graphical way and it corresponds to the crack propagation rate $^{da}/_{dN}$.

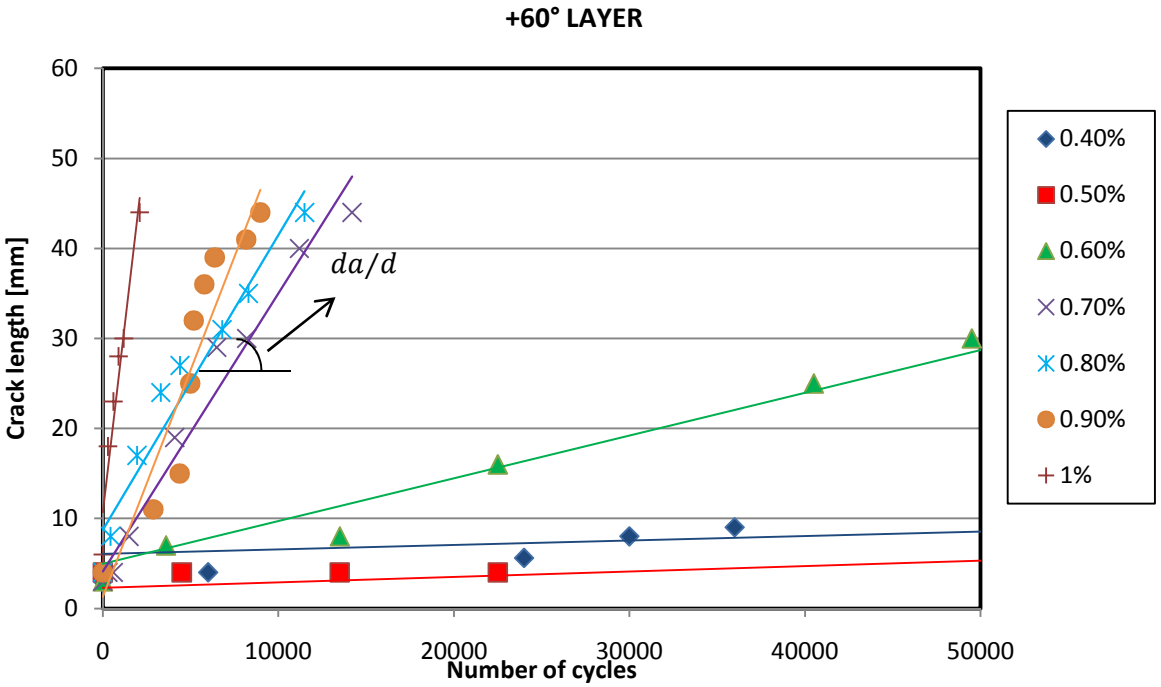

Figure 6-9. Crack length plotted respect to the number of cycles in order to establish the crack propagation rate in the +60° layer by varying strain level

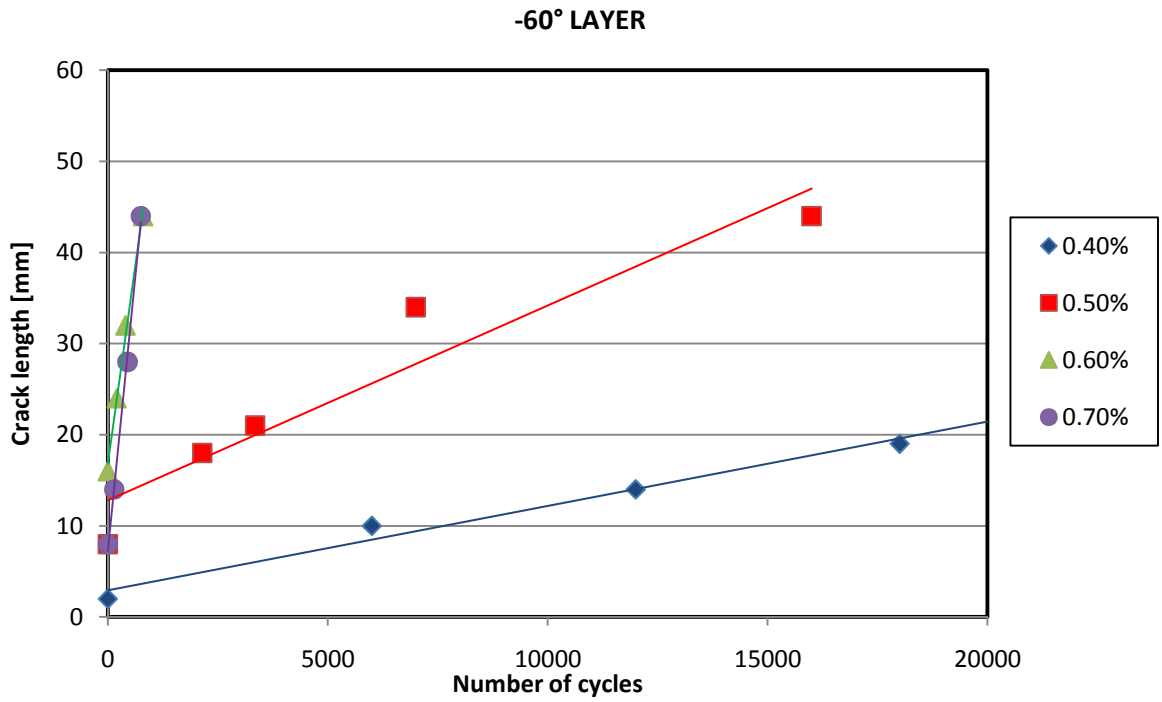

Figure 6-10. Crack length plotted respect to the number of cycles in order to establish the crack propagation rate in the -60°layer by varying strain level

Using the results of the finite elements analysis reported in Table 6.4 and the stress level corresponding to each strain level, the Table 6.8 summarized the crack propagation rate.

	+60° LAYER			-60° LAYER		
Strain level	**da/dN**	**ΔG_{ss}**	**Δσ**	**da/dN**	**ΔG_{ss}**	**Δσ**
%	**[mm/cycle]**	**[KJ/m^2]**	**[MPa]**	**[mm/cycle]**	**[KJ/m^2]**	**[MPa]**
0.4	5.00E-05	0.126532	66.06	0.0009	0.247368	66.06
0.5	1.00E-04	0.180249	78.84	0.0021	0.351074	78.84
0.6	0.0005	0.271951	96.84	0.0349	0.529655	96.84
0.7	0.0031	0.361746	111.69	0.0481	0.704543	111.69
0.8	0.0033	0.487753	129.69	0.2933	0.950242	129.69
0.9	0.005	0.586387	142.2	-	-	-
1.0	0.0166	0.650381	149.76	-	-	-
1.1	0.88	0.855093	171.72	-	-	-

Table 6.8. Summary of the crack propagation rate, the energy release rate and stress applied for every strain level and for both off-axis layer

With the available data it is possible to build a Paris type chart, $^{da}/_{dN}$ with respect to the ΔG_{ss}, see Figure 6-11. At this point, the relation between the energy release rate and the crack propagation rate is known for both off-axis layers.

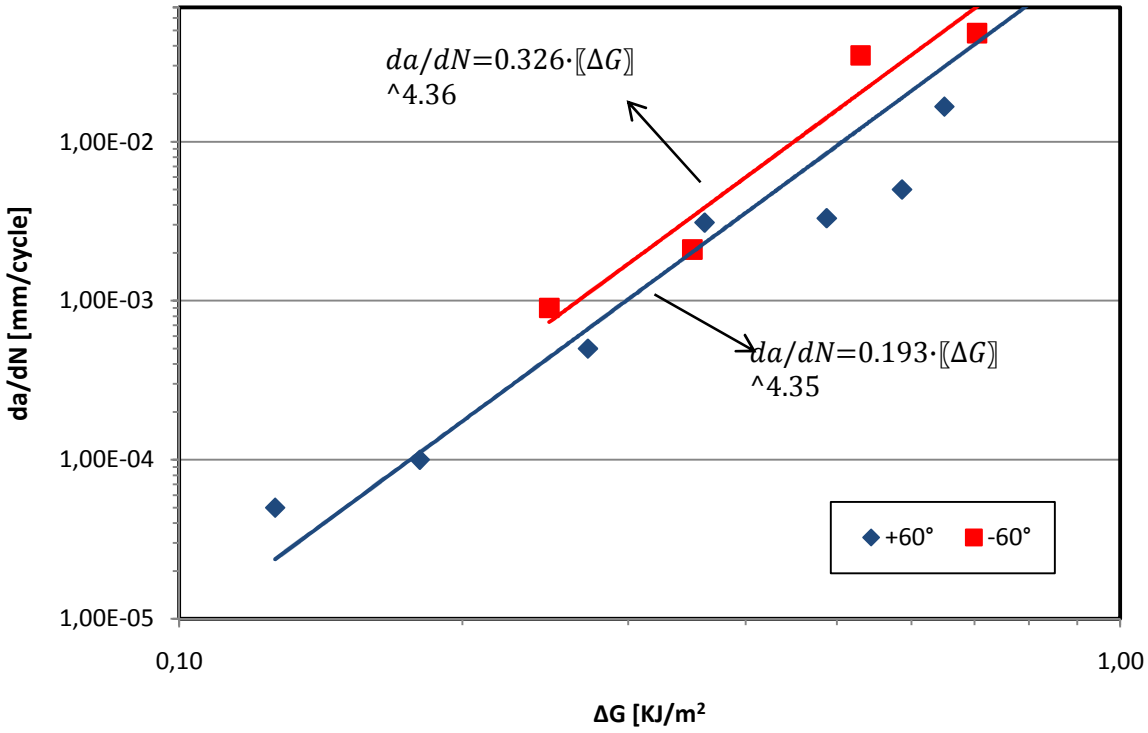

Figure 6-11. Paris type curve for both off-axis layers

Observing the chart in Figure 6-11 it is possible to assert that for both layers:

$$\frac{da}{dN} \propto \Delta G_{ss}{}^{4.3} \qquad 6.10$$

To verify the reliability of this result a comparison was done with similar analysis present in literature. With that has been found in (4), about crack growth in composite laminate at 45°, there is fully agreement.

The equation 6.10, that is valid for both off-axis layers, allows asserting that the relation between the energy release rate and the crack propagation rate is no sensitive to the layer thickness. Moreover, a damage evolution analysis in terms of crack growth rate can be done easily by using an energy approach (as the relation 6.10 has been found) because the thickness effect doesn't appear.

6.5 CRACK DENSITY PREDICTION

Considering what found in the previous paragraphs 6.2 and 6.4 it is now possible give the attention to the damage evolution in terms of crack density; being also one of the aims of this project. In particular, a prediction of the crack density trend with respect to the number of cycles was determined for each strain level applied and after a comparison with the experimental results was done. As has already been exposed, the crack density is considered normalized respect to the thickness, h/L.
The present model is based on the relation 6.5 , in order to calculate the ΔG_{ss} by halving the crack spacing L (i.e. doubling the number of cracks) from an initial value L_0 to a very small value. We have to consider that every new crack grows between two existing cracks. In this way the crack process of the material is replicated.

$$\frac{\bar{E} \cdot \Delta G_{ss}}{\Delta\sigma^2 \cdot h} = 2f_{(h/L)} - f_{(h/2L)} \qquad 6.5$$

For each value of crack density the energy release rate was known and through the Paris low found in Figure 6-11, the corresponding crack propagation rate was determine.

$$+60° \rightarrow \frac{da}{dN} = 0.193 \cdot \Delta G_{ss}{}^{4.35} \qquad 6.11$$

$$-60° \rightarrow \frac{da}{dN} = 0.326 \cdot \Delta G_{ss}{}^{4.36} \qquad 6.12$$

At this point, it was supposed that the cracks (for each value of crack density) have to propagate through the entire sample width W, consequently the range of number of cycles necessary for the propagation ΔN was calculated.

$$\Delta N = \frac{W}{\frac{da}{dN}} \qquad 6.13$$

After that, every ΔN (one for each value of crack density imposed) were added in sequence to determine the corresponding number of cycles N. The index n refers to the h/L level.

$$N_n = N_{n-1} + \Delta N_n \qquad 6.14$$

At this point, plotting the h/L respect to the number of cycles N, the crack density prediction was done.

Remains to determine the initial value L_0; this starting spacing must be proceeds by the experimental images taken observing when the first two cracks appear. There is also to

consider the initial number of cycles N_0 at which these initial cracks initiate; this value must be added to the number of cycles N.
It is important to consider that the function f is known for values of h/L from 0 to 1. This means that the prediction can be done until the crack spacing reaches a value equal to the thickness. For smaller crack spacing the model is inapplicable; a more extensive calculation of the function would be necessary.
For simplicity, this model of prediction was applied only for the +60° layer (h=0.7 mm) but it could be also applied for -60° layer with the same conclusions.

The application of the model to the specific case is now presented. The comparison with the experimental results was done considering the curves in Figure 5-12 only until saturation.

L_0=10 mm	+60° LAYER PREDICTION FOR 1.1% STRAIN LEVEL							N_0=200
L	**h/L**	**h/2L**	**$f_{(h/L)}$**	**$f_{(h/2L)}$**	**ΔGss**	**da/dN**	**ΔN**	**N**
[mm]	**-**	**-**	**-**	**-**	**[KJ/m^2]**	**[mm/cycle]**	**[cycles]**	**[cycles]**
10	0.07	0.035	0.554946	0.575605	1.046441	0.235185	187	200
5	0.14	0.07	0.501422	0.554946	0.877244	0.109108	403	603
2.5	0.28	0.14	0.385497	0.501422	0.527975	0.011956	3680	4283
1.25	0.56	0.28	0.232122	0.385497	0.154231	5.63E-05	782064	786348
0.625	1.12	0.56	-	-	-	-	-	-

Table 6.9. Crack density prediction at 1.1% of strain level in +60° layer

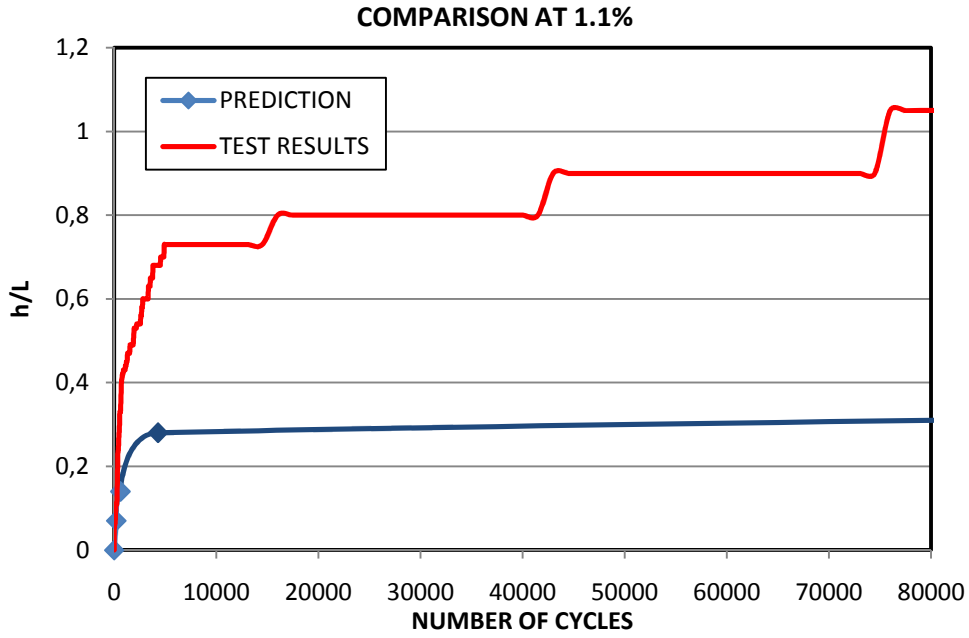

Figure 6-12. Crack density trend comparison between the experimental and the predicted values for +60° layer at 1.1% of strain level

L_0=15 mm	+60° LAYER PREDICTION FOR 1% STRAIN LEVEL							N_0=500
L	**h/L**	**(h/2L)**	**$f_{(h/L)}$**	**$f_{(h/2L)}$**	**ΔGss**	**da/dN**	**ΔN**	**N**
[mm]	**-**	**-**	**-**	**-**	**[KJ/m^2]**	**[mm/cycle]**	**[cycles]**	**[cycles]**
15	0.05	0.02	0.569365	0.581085	0.830708	0.086054	511	500
7.5	0.09	0.05	0.538455	0.569365	0.756075	0.057113	770	1270
3.75	0.19	0.09	0.461931	0.538455	0.574129	0.017222	2554	3825
1.875	0.37	0.19	0.32121	0.461931	0.268871	0.000633	69521	73346
0.9375	0.75	0.37	0.163726	0.32121	0.009299	2.74E-10	1.6E+11	1.6E+11
0.46875	1.49	-	-	-	-	-	-	-

Table 6.10. Crack density prediction at 1% of strain level in +60° layer

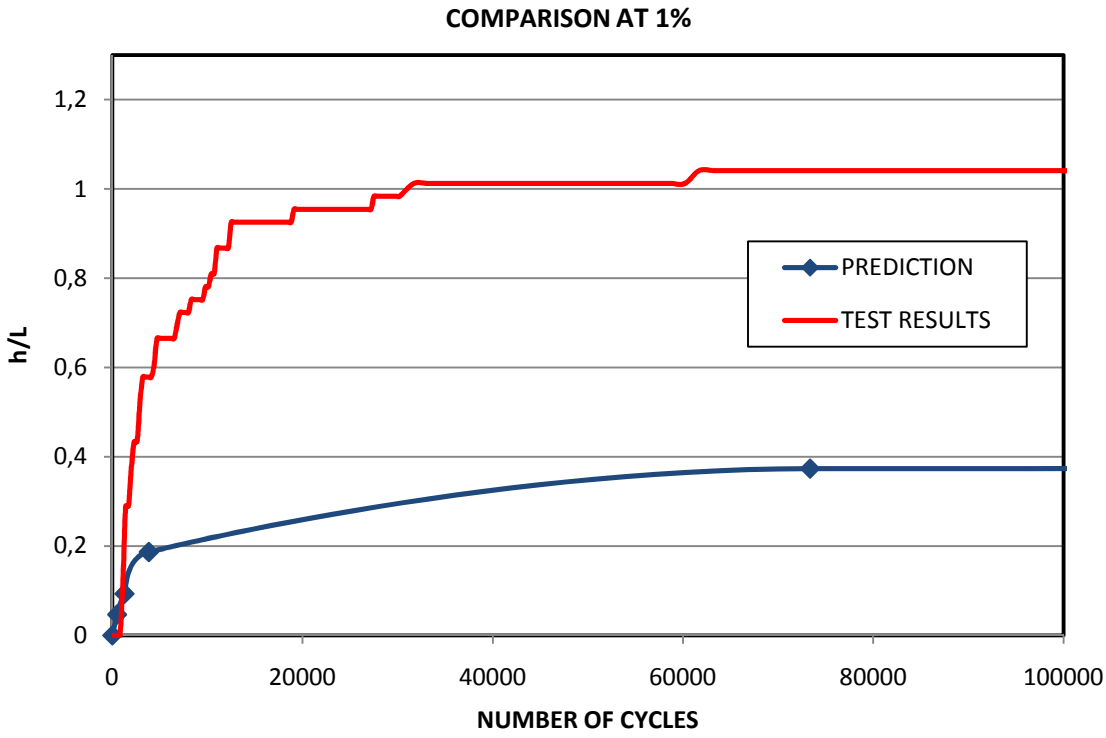

Figure 6-13. Crack density trend comparison between the experimental and the predicted values for +60° layer at 1% of strain level

L_0=41 mm	+60° LAYER PREDICTION FOR 0.9% STRAIN LEVEL							N_0=500
L	**h/L**	**h/2L**	**$f_{(h/L)}$**	**$f_{(h/2L)}$**	**ΔGss**	**da/dN**	**ΔN**	**N**
[mm]	**-**	**-**	**-**	**-**	**[KJ/m^2]**	**[mm/cycle]**	**[cycles]**	**[cycles]**
41	0.017	0.009	0.58368	0.58680	0.77973	0.065314	673	500
20.5	0.034	0.017	0.57603	0.58368	0.76338	0.059554	738	1238
10.25	0.068	0.034	0.55608	0.57603	0.72005	0.046174	952	2191
5.125	0.137	0.068	0.50425	0.55608	0.60764	0.022049	1995	4187
2.5625	0.273	0.137	0.39076	0.50425	0.37238	0.002614	16833	21020
1.28125	0.546	0.273	0.23742	0.39076	0.11293	1.45E-05	3038863	3059884
0.640625	1.093	0.546	-	-	-	-	-	-

Table 6.11. Crack density prediction at 0.9% of strain level in +60°layer

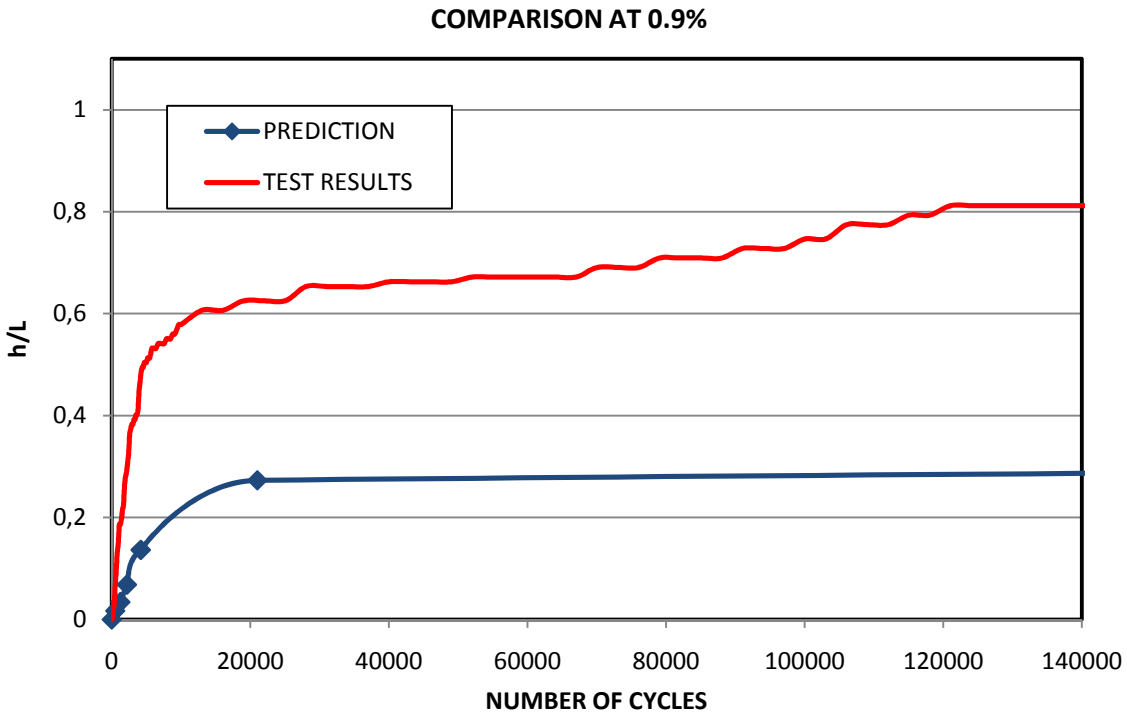

Figure 6-14. Crack density trend comparison between the experimental and the predicted values for +60° layer at 0.9% of strain level

L_0=40 mm	+60° LAYER PREDICTION FOR 0.8% STRAIN LEVEL							N_0=750
L	**h/L**	**h/2L**	**$f_{(h/L)}$**	**$f_{(h/2L)}$**	**ΔGss**	**da/dN**	**ΔN**	**N**
[mm]	**-**	**-**	**-**	**-**	**[KJ/m^2]**	**[mm/cycle]**	**[cycles]**	**[cycles]**
40	0.017	0.00875	0.58351	0.58673	0.64828	0.029229	1505	750
20	0.035	0.0175	0.57560	0.58351	0.63420	0.026565	1656	2406
10	0.07	0.035	0.55495	0.57560	0.59688	0.020398	2157	4563
5	0.14	0.07	0.50142	0.55495	0.50037	0.009463	4649	9213
2.5	0.28	0.14	0.38550	0.50142	0.30115	0.001037	42431	51644
1.25	0.56	0.28	0.23212	0.38550	0.08797	4.88E-06	9017131	9068775
0.625	1.12	-	-	-	-	-	-	-

Table 6.12. Crack density prediction at 0.8% of strain level in +60°layer

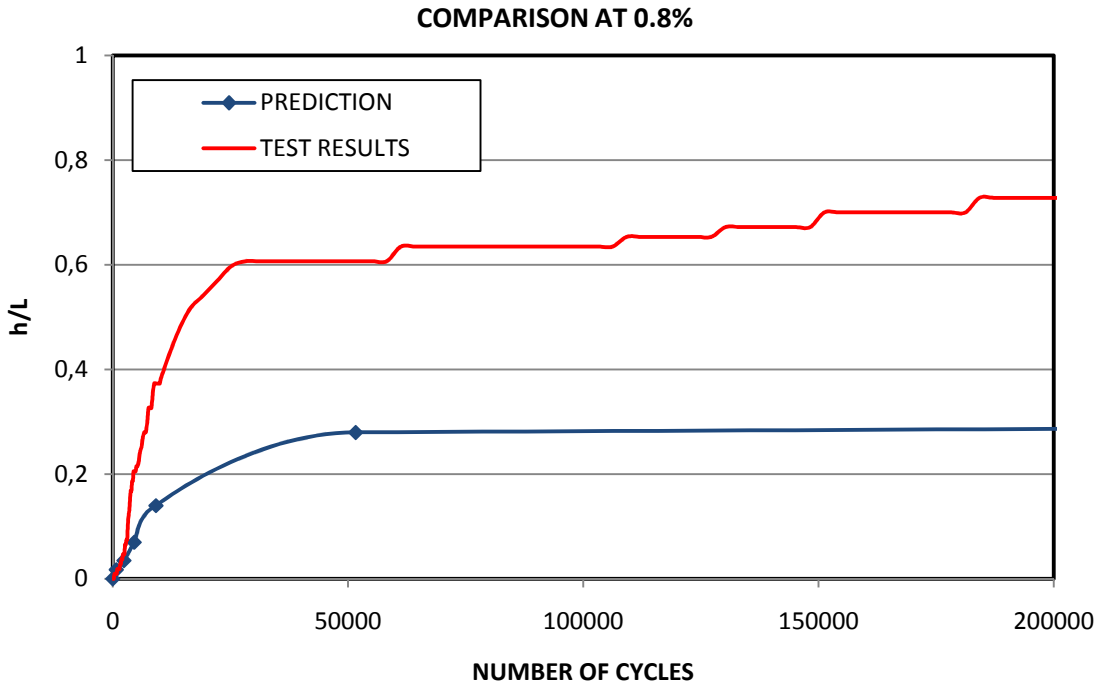

Figure 6-15. Crack density trend comparison between the experimental and the predicted values for +60° layer at 0.8% of strain level

L_0=40 mm	+60° LAYER PREDICTION FOR 0.7% STRAIN LEVEL							N_0=1000
L	**h/L**	**h/2L**	**$f_{(h/L)}$**	**$f_{(h/2L)}$**	**ΔGss**	**da/dN**	**ΔN**	**N**
[mm]	**-**	**-**	**-**	**-**	**[KJ/m^2]**	**[mm/cycle]**	**[cycles]**	**[cycles]**
40	0.0175	0.00875	0.58351	0.58673	0.48081	0.007955	5531	1000
20	0.035	0.0175	0.57560	0.58351	0.47037	0.00723	6086	7086
10	0.07	0.035	0.55495	0.57560	0.44269	0.005551	7925	15012
5	0.14	0.07	0.50142	0.55495	0.37111	0.002575	17084	32096
2.5	0.28	0.14	0.38550	0.50142	0.22336	0.000282	155908	188004
1.25	0.56	0.28	0.23212	0.38550	0.06525	1.33E-06	33132443	33320448
0.625	1.12	-	-	-	-	-	-	-

Table 6.13. Crack density prediction at 0.7% of strain level in +60°layer

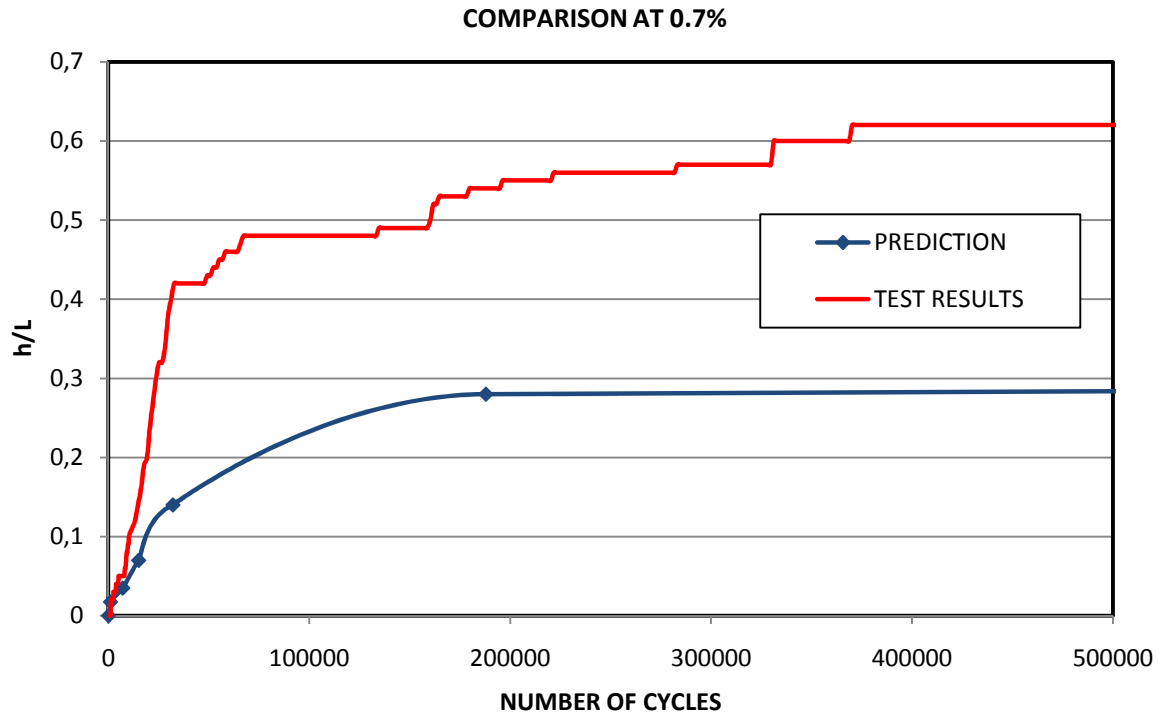

Figure 6-16. Crack density trend comparison between the experimental and the predicted values for +60° layer at 0.7% of strain level

L_0=20 mm	+60° LAYER PREDICTION FOR 0.6% STRAIN LEVEL							N_0=5000
L	**h/L**	**h/2L**	**$f_{(h/L)}$**	**$f_{(h/2L)}$**	**ΔGss**	**da/dN**	**ΔN**	**N**
[mm]	**-**	**-**	**-**	**-**	**[KJ/m^2]**	**[mm/cycle]**	**[cycles]**	**[cycles]**
20	0.035	0.018	0.57560	0.58351	0.43656	0.005224	8422	5000
10	0.070	0.035	0.55495	0.57560	0.41086	0.004011	10968	15968
5	0.140	0.070	0.50142	0.55495	0.34443	0.001861	23643	39612
2.5	0.280	0.140	0.38550	0.50142	0.20730	0.000204	215765	255378
1.25	0.560	0.280	0.23212	0.38550	0.06056	9.6E-07	45852875	46108253
0.625	1.120	0.560	-	-	-	-	-	-

Table 6.14. Crack density prediction at 0.6% of strain level in +60°layer

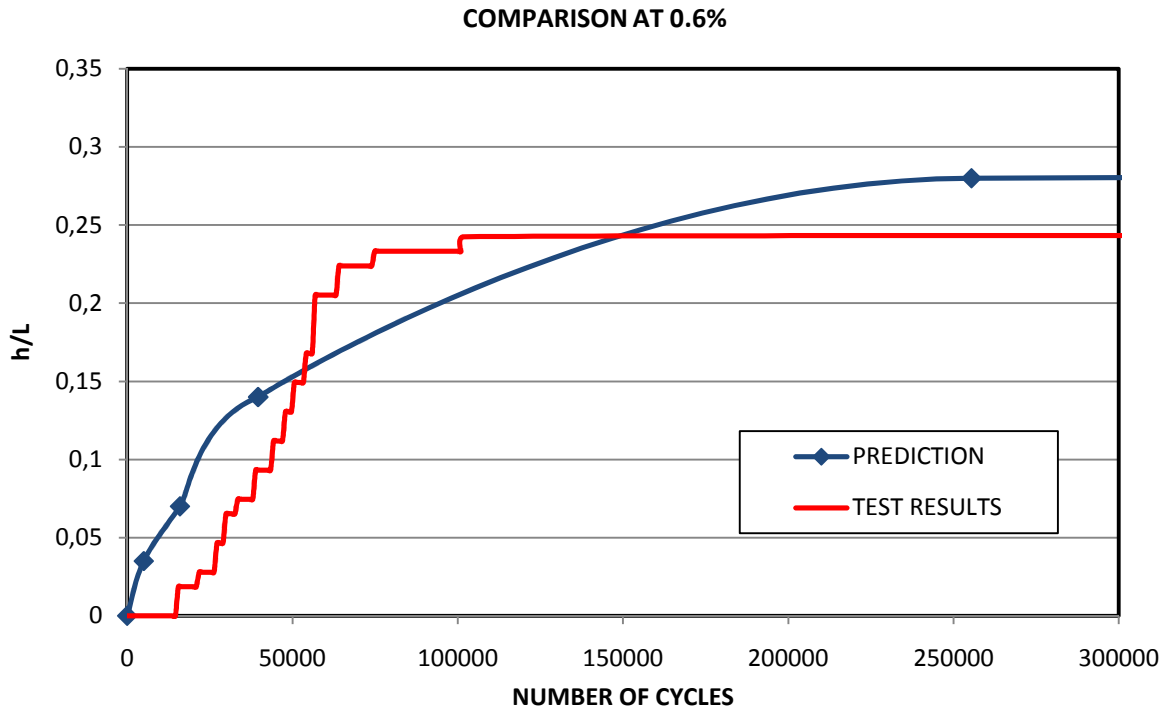

Figure 6-17. Crack density trend comparison between the experimental and the predicted values for +60° layer at 0.6% of strain level

L_0=30 mm	+60° LAYER PREDICTION FOR 0.5% STRAIN LEVEL							N_0=5000
L	h/L	h/2L	$f_{(h/L)}$	$f_{(h/2L)}$	ΔGss	da/dN	ΔN	N
[mm]	-	-	-	-	[KJ/m^2]	[mm/cycle]	[cycles]	[cycles]
30	0.0233	0.0117	0.58108	0.58572	0.29381	0.000931	47242	180000
15	0.0467	0.0233	0.56937	0.58108	0.28423	0.000806	54585	234585
7.5	0.0933	0.0467	0.53846	0.56937	0.25869	0.000535	82246	316831
3.75	0.1867	0.0933	0.46193	0.53846	0.19644	0.000161	272744	589575
1.875	0.3733	0.1867	0.32121	0.46193	0.09199	5.93E-06	7421857	8011433
0.9375	0.7467	0.3733	0.16373	0.32121	0.00318	2.57E-12	1.71E+13	1.71E+13
0.46875	1.4933	0.7467	-	-	-	-	-	-

Table 6.15. Crack density prediction at 0.5% of strain level in +60°layer

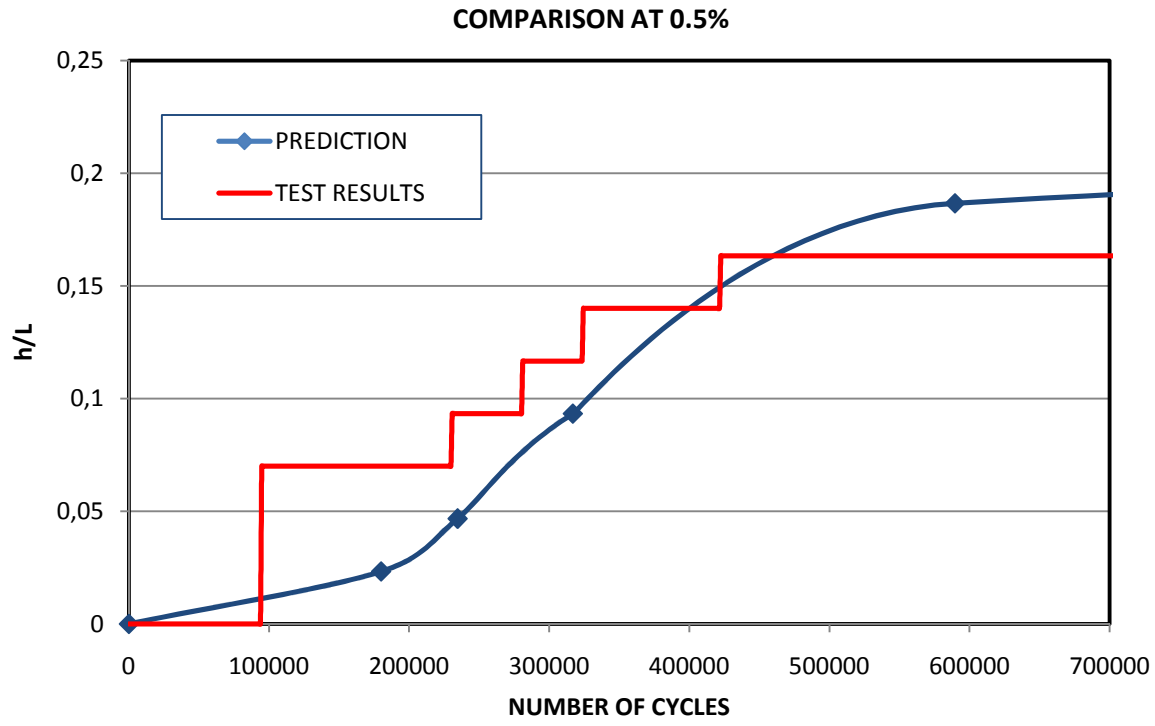

Figure 6-18. Crack density trend comparison between the experimental and the predicted values for +60° layer at 0.5% of strain level

With 0.4% strain level the experimental results showed the presence of only one crack in the +60° layer. For these reason in this case there was no point to apply the prediction model that is based on a multiple cracking condition.

Observing all results above it is possible to assert that in general the saturation level predicted is about half compared to the experimental one, except for the 0.5% and 0.6% strain level in which the results are in total agreement. In all cases the predicted curve is very closed to the experimental one for low number of cycles; this means that the model works well until the number of cracks is quite low. With high strain level the experimental crack density exceeds the unit value and therefore, in this region, it is impossible to make a comparison with the predicted curve because it isn't known, as previous explained.

The differences between the predicted and the experimental curves, especially for high number of cycles, can be explained considering that the model assumes a new crack propagation only after the previous ones are completely tunneled through the width of the sample. In fact, all ΔN calculated are added in sequence one by one so as to reconstruct the entire scale of the number of cycles N. By the experimental observations in the real case this condition is true only with a low number of cracks and thus when the number of cycles is very low. Instead when the crack presence raises and the cycles increase, cracks initiate before that the previous ones are completely tunneled. This means that the ΔN determined by the model should be overlapped as the crack density increase, in this way the scale of the number of cycles would be reduced. To find a general law that can explain this overlapping is not simple; a more accurate analysis of the images acquired is necessary in order to determine the number of cracks that initiate simultaneously at every number of cycles (or only at particulars values) and consequently to correct the model. With this correction the model would be calibrated and should be closed to experimental results also at high number of cycles.

6.5.1 Verification of the predicted crack propagation rate

How it has been explained, to verify a complete agreement of the prediction model with the experimental results it is necessary to find a law correction of the number of cycles, but it is very complicated and very long. Anyway, to validate in another way the model it is possible to verify if the crack propagation rates ($^{da}/_{dN}$) estimated are in according with the corresponding experimental values. Precisely, an analysis of the images acquired about the +60° layer was done in or der to calculate the propagation growth rate at various crack length and for each strain level. After, a comparison of these values with ones determined by the prediction model, Table 6.9 → Table 6.15, was done. The cases at high strain level were considered because only with these ones the accuracy of the images was high enough for the purpose. For low strain level, the number of cracks is very low and the propagation is slow thus it was difficult to well determine the propagation rate. Anyway, if the validation is correct at high strain level it is possible to expand the conclusions also for low strain level cases. The results of the present verification are now illustrated.

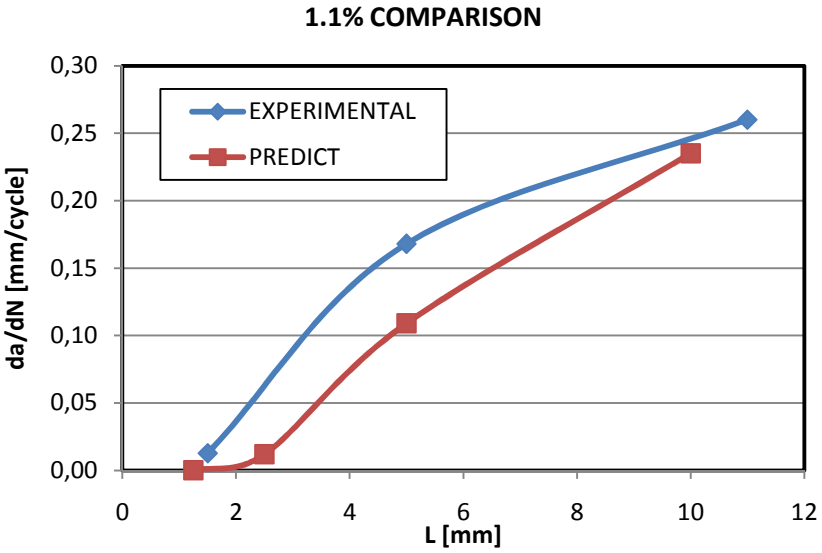

Experimental	
1.1% STRAIN LEVEL	
L	da/dN
[mm]	[mm/cycle]
11	0.2600
5	0.1680
1.5	0.0127

Figure 6-19. Crack propagation comparison between the experimental and the predicted values at 1.1% of strain level and for +60°layer. On the right are s ummarized the experimental values.

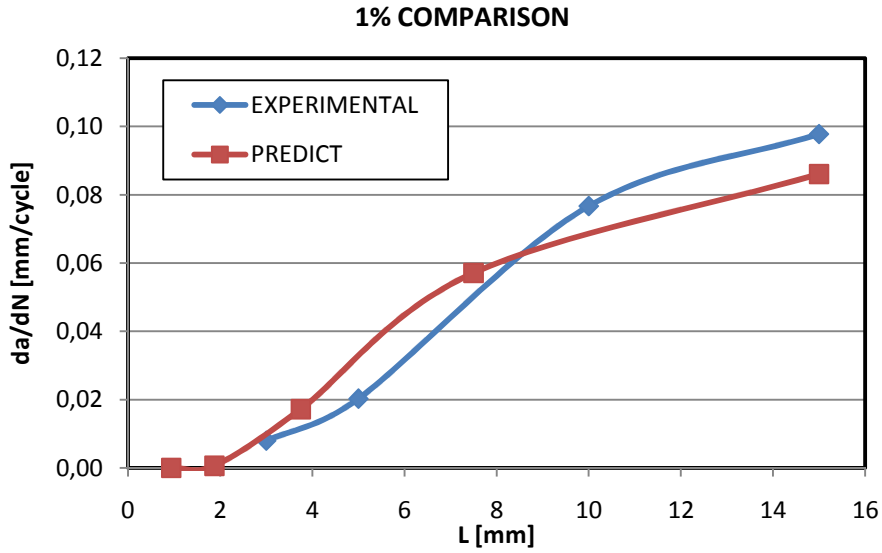

Experimental	
1% STRAIN LEVEL	
L	da/dN
[mm]	[mm/cycle]
15	0.0978
10	0.0767
5	0.0203
3	0.0080

Figure 6-20. Crack propagation comparison between the experimental and the predicted values at 1% of strain level and for +60°layer. On the right are s ummarized the experimental values.

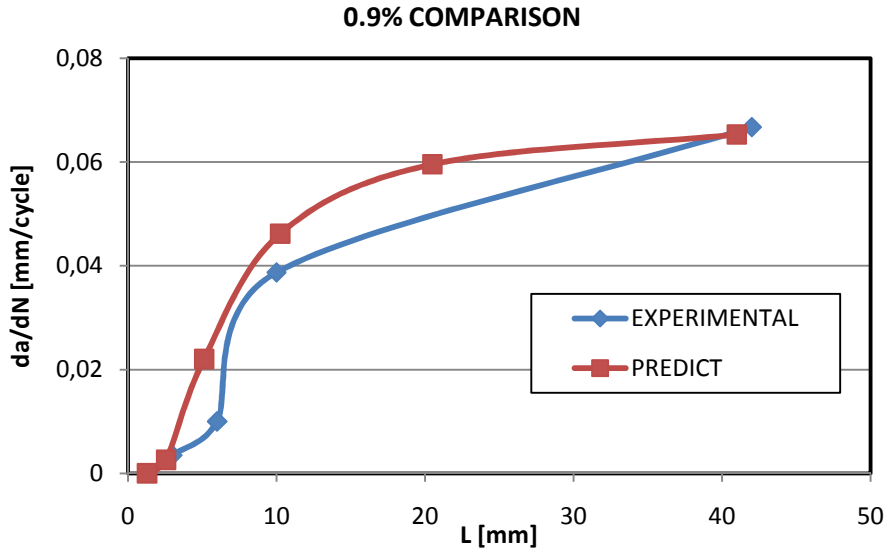

Experimental	
0.9% STRAIN LEVEL	
L	da/dN
[mm]	[mm/cycle]
42	0.0667
10	0.0387
6	0.01
3	0.0035

Figure 6-21. Crack propagation comparison between the experimental and the predicted values at 0.9% of strain level and for +60°layer. On the right are s ummarized the experimental values.

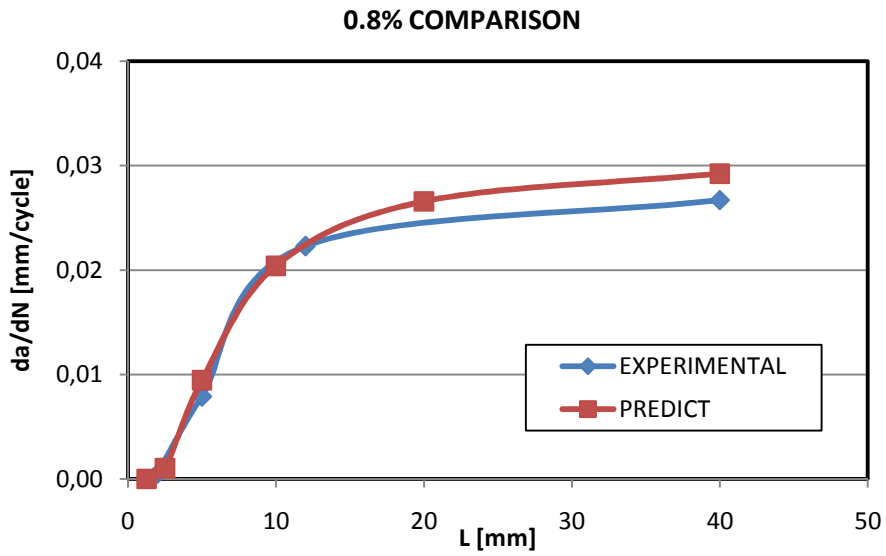

Experimental	
0.8% STRAIN LEVEL	
L	da/dN
[mm]	[mm/cycle]
40	0.0267
12	0.0223
5	0.0079
2	0.0005

Figure 6-22. Crack propagation comparison between the experimental and the predicted values at 0.8% of strain level and for +60°layer. On the right are s ummarized the experimental values.

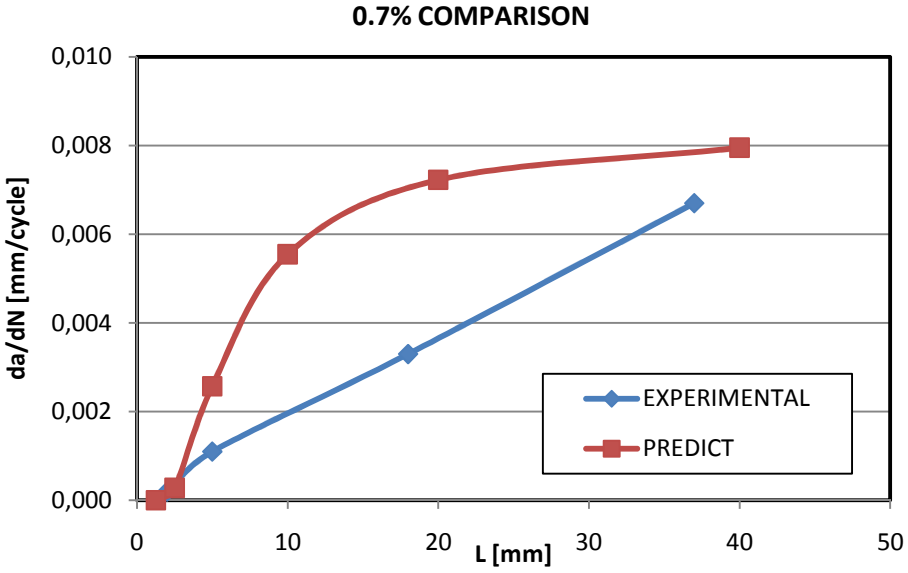

Experimental	
0.7% STRAIN LEVEL	
L	da/dN
[mm]	[mm/cycle]
37	0.0067
18	0.0033
5	0.0011
2	0.0002

Figure 6-23. Crack propagation comparison between the experimental and the predicted values at 0.7% of strain level and for +60°layer. On the right are s ummarized the experimental values.

Observing the results, the crack propagation rate predicted by the model is in agreement with the experimental results. At 0.7% strain level the curves aren’t very overlapped, this because the accuracy of the experimental images doesn’t permit to determine exactly the crack propagation rate. The results with the other low strain level aren’t reported because completely unnecessary. Anyway, it is possible to suppose that the model predicts a correct crack propagation rate also in those cases.

With this latest verification, it is possible to assert that the prediction model exposed in 6.5 works rather well considering all the approximations introduced. Thus, it is possible to assert that the different crack density predicted is due to simultaneous propagation of cracks at high number of cycles. By a more accurate calibration of the model this condition can be quantified, as already explained.

7 FATIGUE DAMAGE COMPARISON BETWEEN FLAT AND TUBULAR COMPOSITE LAMINATES

7.1 GENERALITY

In this chapter a damage evolution comparison is conducted between the $[0/(+60)_2/0/(-60)_2]_S$ flat laminates and tubular laminates $[0_T/90_{ud,3}]$ and $[0_T/90_{ud,3}/0_T]$, in order to assess by an experimental way a possible correlation among a global and a local multiaxial stress condition present in the material. Two types of tubular samples are considered to obtain the most similar constraint condition on the off-axis layers with the flat samples. The comparison is focused on the crack density trend as a parameter that well explains the damage evolution and on the first crack Wohler's curve. Both types of laminates are produced with the same glass/epoxy composite material and are loaded with a similar value of biaxiality ratio.

7.2 TUBULAR SAMPLES RESULTS

The project regarding the tubular composite laminates, reported in (2) and (5), consists in an extensive investigation on the damage evolution in composite glass/epoxy tubes subjected cyclic tension-torsion loading. In particular, S-N fatigue curves, stiffness trends and microscopic damage evolution for different values of biaxiality ratio are considered. Tubular samples to be tested under combined tension-torsion loading were considered as the optimum solution to avoid free-edge effects on the damage evolution. Moreover, by varying the ratio between external tension and torsion loading the mutual influence of stress components on the damage evolution can be investigated.

7.2.1 MATERIALS AND SPECIMENS

Tubular samples were produced by wrapping of 3 layers of glass/epoxy UD pre-preg at 90°, with respect to the longitudinal, axis plus a balanced fabric layer. In this way the lay-up is $[0_T/90_{ud,3}]$ and $[0_T/90_{ud,3}/0_T]$. The latter lay-up provides a constraint condition on the off-axis layers more similar to that of flat samples, because in this case the 90° layers are between two fabric layers. In general the presence of fabric layer in tubular samples facilitates a stable and measureable growth of fatigue damage. The following pre-pregs were considered: UD tape UE400-REM produced by SEAL-Italy and Balanced fabric VV345T-DT107A produced by Deltatech-Italy.

7.2.2 EXPERIMENTAL TEST RESULTS ON $[0_T/90_{ud,3}]$

The multiaxial fatigue behavior of the tubes was investigated by means of pulsating tension-torsion fatigue loading. Tests were carried out on a MTS 809 axial-torsional machine, under load/torque control at a frequency of 10 Hz. The combination between tensile and torsion loads was varied in order to obtain nominal values of biaxiality ratio λ_{12} equal to 0.5, 1.0 and 2.0. However, the real values of λ_{12} present in the material are different and in particular are 0.63, 1.25 and 2.51 respectively. During the tests, specimens were illuminated by an internal LED light system to better investigate the damage evolution and, in particular, the crack onset and growth. This is possible by the transparency of the glass/epoxy tubes.
The most useful results, for the comparison here considered, concern the crack density trend respect the number of cycles and the Wohler's curve of the material regarding the first crack appearance. Considering that with flat composite samples the tests were conducted only with biaxiality ratio equal to 0.57, it is important to assert that only the tubular test results closed to this particular value of λ_{12} are significant.

$[0_T/90_{ud,3}]$ SAMPLES

In Figure 7-1 the crack density trend for tubular samples with λ_{12} equal to 0.63 is reported and by varying the external stress applied σ_2 from 24 to 40 MPa, as showed in the legend. In Figure 7-2 the tubular samples first crack Wohler's curve is reported for the different biaxiality ratio values.

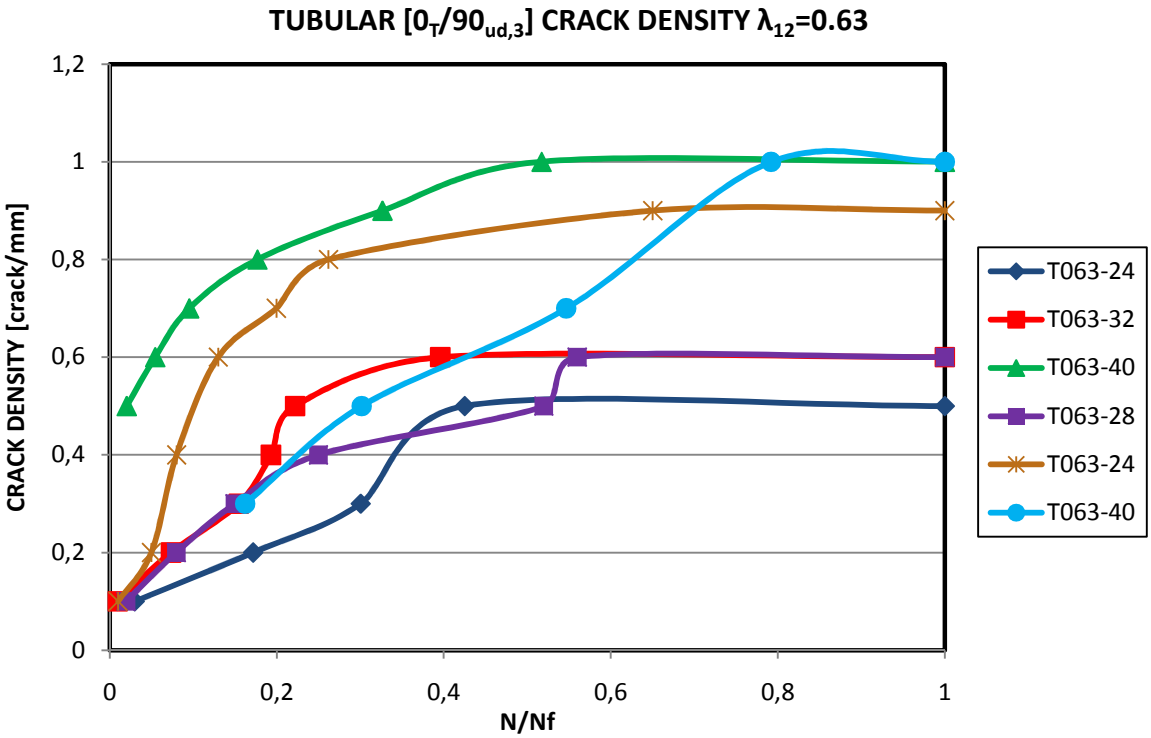

Figure 7-1. Crack density trend for tubular samples $[0_T/90_{ud,3}]$ with biaxiality ratio λ_{12} equal to 0.63 and by varying the external stress applied σ_2

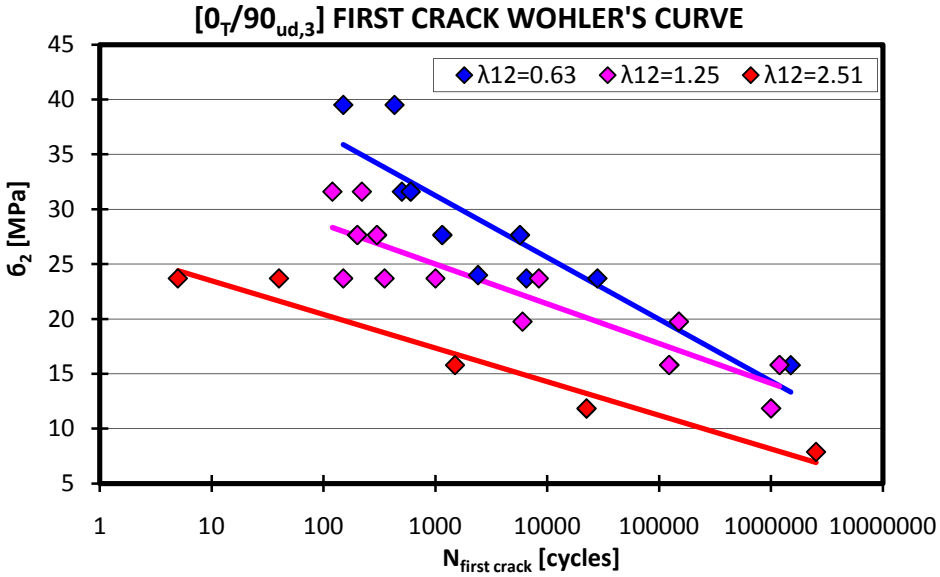

Figure 7-2. Wohler's curves of tubular samples [0_T/$90_{ud,3}$] regarding the first crack that appears in the material for different values of biaxiality ratio

[0_T/$90_{ud,3}$/0_T] SAMPLES

The experimental fatigue tests on [0_T/$90_{ud,3}$/0_T] samples were conducted considering only a biaxiality ratio λ_{12} equal to 1.0 and 2.0. During the tests was observed the presence of only one crack until failure. This means that there is not a multiple cracking condition of material and consequently it is not possible to speak of crack density. The only useful results for the comparison with flat samples regard the first crack Wohler's curve with λ_{12} equal to 1.0,

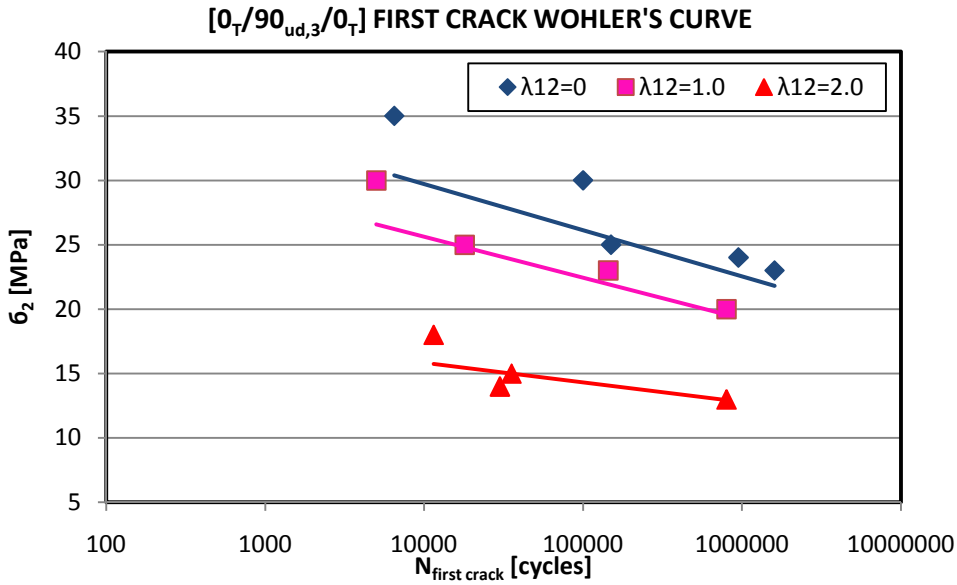

Figure 7-3. Wohler's curves of tubular samples [0_T/$90_{ud,3}$/0_T] regarding the first crack that appears in the material for different values of biaxiality ratio

7.3 FATIGUE TEST RESULTS COMPARISON

The comparison is focused on damage evolution and fatigue behavior of the material, in particular in terms of crack density and Wohler's curve under the same nominal value of biaxiality ratio. For flat and tubular samples the real value of λ_{12} present in the material is different with respect to the nominal one, because of the influence of the stacking sequence on the local stress state. In specific:

Flat samples $[0/(+60)_2/0/(-60)_2]_s$ → λ_{12}=0.57

Tubular samples $[0_T/90_{ud,3}]$ → λ_{12}=0.63

Tubular samples $[0_T/90_{ud,3}/0_T]$ → λ_{12}=1.0

As already stated, regarding the samples it is possible to do a comparison with flat samples only in terms of first crack Wohler's curve, because of there is not the presence of multiple cracking phenomenon.

7.3.1 CRACK DENSITY TREND COMPARISON

The experimental crack density curves for flat and tubular samples $[0_T/90_{ud,3}]$, at different load levels, can be gathered together in order to highlight a possible similar trend, as reported in **Errore. L'origine riferimento non è stata trovata.**. It is very important to consider that the off-axis layers in flat and tubular samples have a different thickness. Specifically, in flat samples the +60° group has two plies and the -60° group has four plies, instead in tubular samples the 90° group consists in three plies. The ply thickness has an important influence on the crack density value, for this reason it is necessary to normalize the crack density with respect to the layer thickness (as considered in chapter 6) in order to remove its effect and therefore be able to do a crack density comparison. The normalization consists to multiply the crack density for the thickness h, in order to obtain a dimensionless value; considering that the crack density is equal to the reverse of crack spacing L, it is possible to write the normalization as:

$$\frac{1}{L}\left[\frac{1}{mm}\right] \cdot h_{[mm]} = \frac{h}{L} \rightarrow \text{Normalized crack density}$$

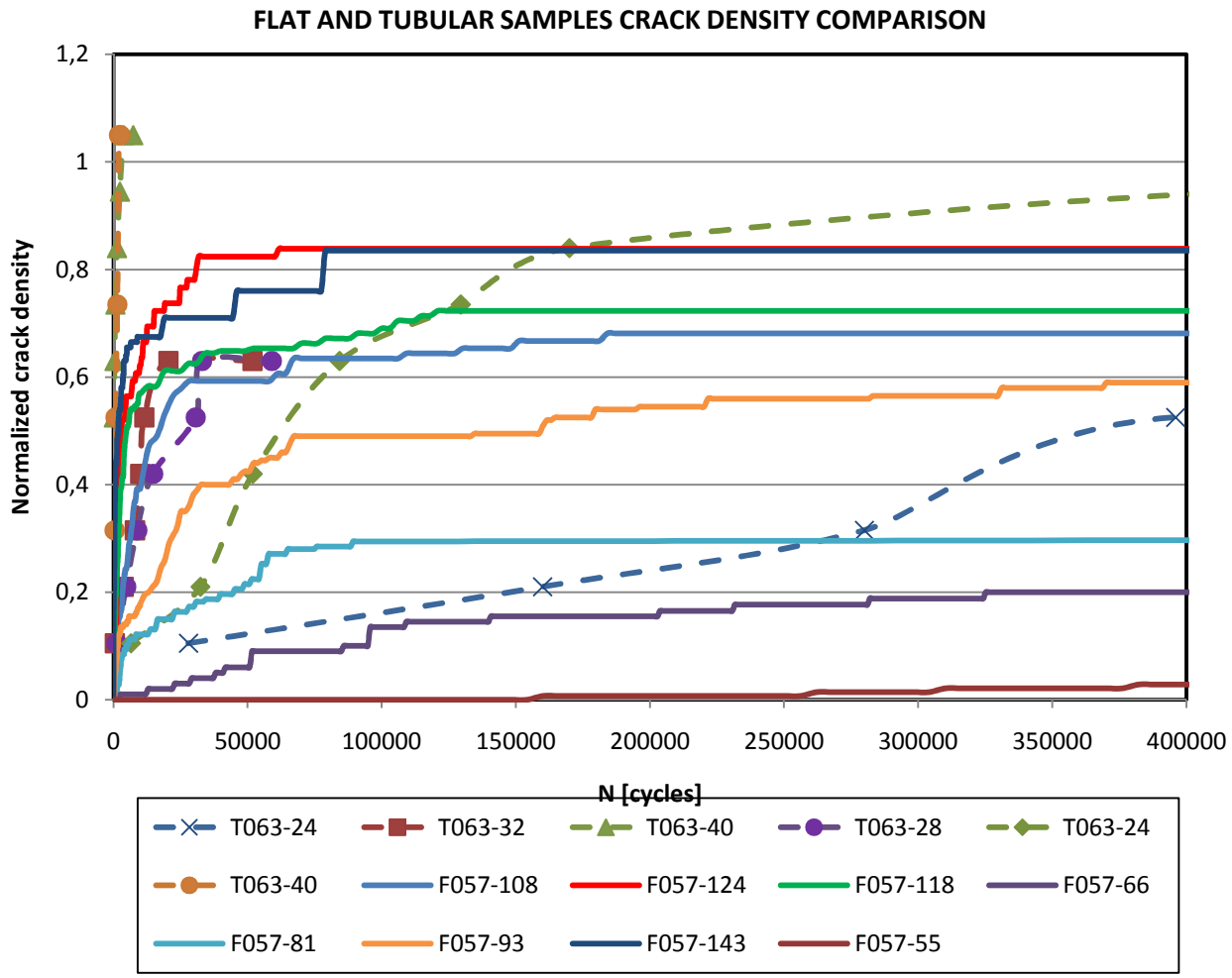

Figure 7-4. Crack density comparison between flat and tubular sample [0_T/$90_{ud,3}$] with same value of biaxiality ratio and by varying the external load applied. The legend distinguishes flat and tubular samples with F and T, identifies λ12 equal to 0.63 (tubular) or to 0.57 (flat) and reports the value of σ2 applied.

Observing the chart in **Errore. L'origine riferimento non è stata trovata.** it is possible to assert that the crack density trends of flat and tubular samples are not comparable and an important observation is that the values of applied stress σ_2 in flat samples are much greater with respect to the tubular, this means that in flat laminates the material strength is higher and then a larger value of applied stress is necessary to obtain a similar crack density value with tubular laminates. This condition is due to the different constraint level in the off-axis layers; in fact in flat samples the 60° layers are between two 0° layers, instead in tubular samples the 90° layer has only one fabri c layer on the internal side. The stiffness of 0° layer is almost twice than to the fabric laye r. Probably flat samples are characterized by the phenomenon of in-situ strength that provides to increase the off-axis layers strength by the 0° layers. This condition, present only in f lat samples could influence the experimental results and for this reason it is not possible to compare directly the crack density values for flat and tubular samples even if the biaxiality ratio it is the same.

7.3.2 WOHLER'S CURVE COMPARISON

During the experimental tests with flat and tubular samples the damage evolution was monitored by a system of images acquisition that allowed to identifying the number of cycles when the first crack appeared. In this way it was possible to construct the Wohler's curve of the material about the first crack considering the applied local transverse stress σ_2. In Figure 7-5 the Wohler's curves for flat and tubular samples are gathered together in double logarithmic scale. Regarding the tubular samples $[0_T/90_{ud,3}]$ is reported also the curve with λ_{12} equal to 1.25 in order to evaluate the influence of biaxiality ratio on the fatigue behavior.

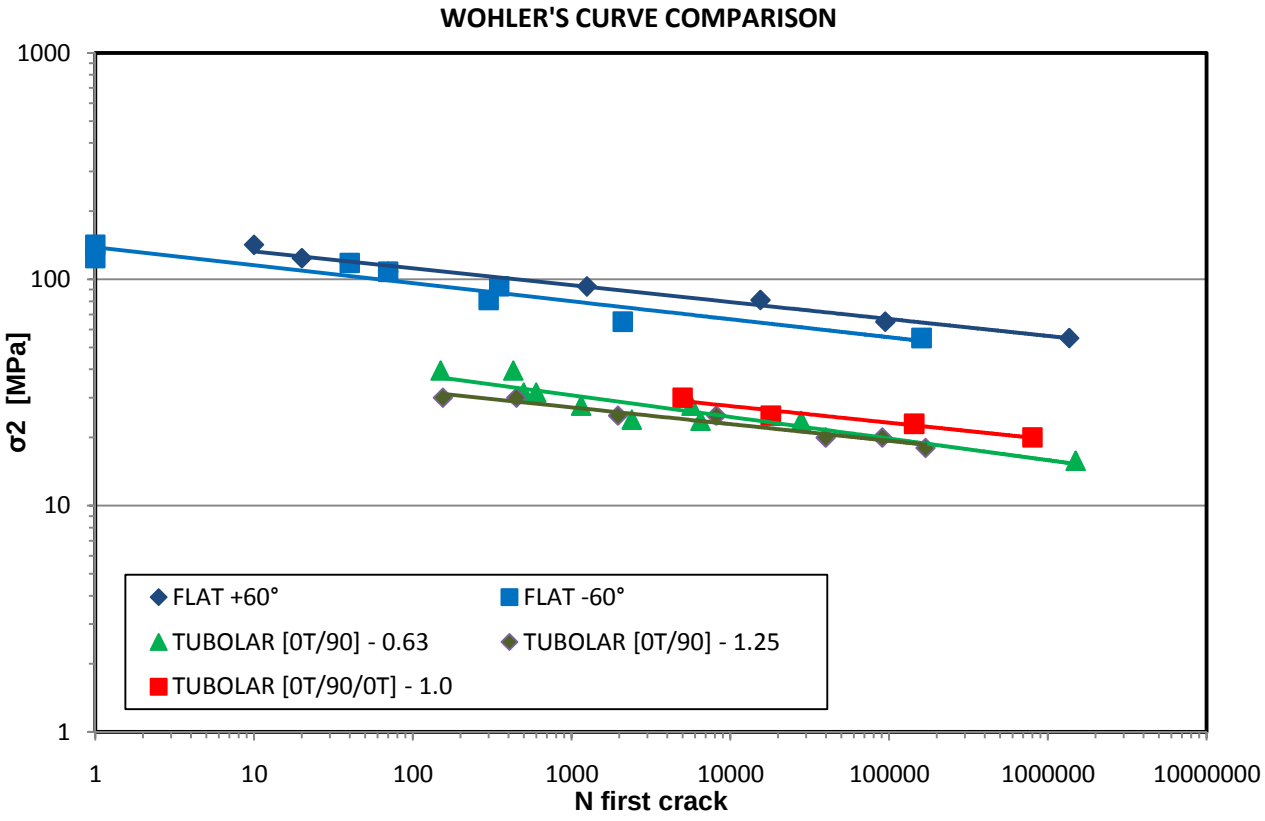

Figure 7-5. Comparison of Wohler's curve between flat and tubular samples regarding the first crack that appears in the material. For flat samples the curves are distinguished for +60° layer and -60° layer.

The chart in Figure 7-5 allows to observing that the curves about flat samples are overlapped to each other and thus the fatigue behavior it is the same being the ply thickness the only difference between +60° and -60° layers.

Between tubular samples at different biaxiality ratio there are no differences. This means that considering a biaxiality ratio equal to 0.63 or 1.25 it is same from the point of view of fatigue behavior. Moreover, considering the different tubular samples also in this case there is not a significant difference between the curves. Thus, introducing an external fabric layer on tubular samples the increase in fatigue strength is very low.

Regarding the comparison between flat and tubular samples it is possible to observe that there are no differences about the curve's slope but the lines of tubular results is shifted down with respect to the lines of flat samples. This difference highlights the effects of higher constraint of off-axis layers in flat samples with respect to the tubular ones. It is important to remember that the stiffness of 0° laye rs (in flat samples) is twice with respect to the fabric layer (in tubular samples). Probably the phenomenon of in-situ strength in flat samples can explain the reason why the tubular Wohler's curve is shifted down.

Concluding, the effect of different constraint condition on off-axis layers, between flat and tubular samples, does not allow to directly comparing the fatigue damage evolution. Further analysis are necessary in order to evaluate and to quantify what are the constraint condition effects on the crack density and fatigue behavior of the off-axis layers.

8 CONCLUSIONS

Planar glass-epoxy samples with lay-up $[0/(+60)_2/0/(-60)_2]_s$ were considered for a damage analysis under uniaxial fatigue loading. The attention is given on the off-axis layer where a multiaxial local stress state exists. The biaxiality ratio has been considered as a parameter that well summarizes the effects of a multiaxial stress field on the fatigue behavior; as explained in (3). In particular, the relation between the off-axis angle and the biaxiality ratio has been carried out, showing a high sensitive. Basing on this finding, the off-axis angle was determined in order to obtain a theoretical value of biaxiality ratio equal to 0.5. Next, a careful finite elements analysis of the chosen lay-up showed that the real value of biaxiality ratio present in the material was a little bit higher, but anyway closed to theoretical one.

Five static tests were done in order to determine the material properties and any presence of production process defects. The results showed the presence of few porosity and a net delamination between layers with different orientation. Anyway, the material were considered reliable and the static mechanical properties were used to calibrate the subsequently fatigue test.

The experimental fatigue tests were conducted by varying the strain level applied and monitoring the cracks evolution through an automatic system of images acquisition. The fatigue tests results showed that after a certain number of cycles the crack density reaches a saturation condition constant to failure; the values of this saturation raise as the strain level applied increases. At the same time the sample's stiffness decays until a constant value in which the off-axis layers are totally cracked and only the 0° layers carry the load. The off-axis layers (+60° and -60°) have a differen t behavior in terms of crack density, this means that the thickness has a significant effects. In particular the +60° layers have a double crack density value with respect to the -60° in each strain level. Moreover, the crack propagation rate observed during the experimental tests is different between the off-axis layer and depends on the strain level applied; in fact the +60° layers show in general an instantaneous propagation, instead in the +60° l ayers cracks need several cycles to propagate through the entire sample's width.

The damage analysis, developed by several ABAQUS simulations and based on the theoretical model of Hutchinson and Suo (1), were done considering a multiple tunneling cracks condition in the off-axis layers. The results allowed finding a relation between the normalized crack spacing and the steady-state energy release rate. Through this results the Paris type curve of the off-axis layers was constructed and finding no significant differences between these layers. After, a prediction of the crack density evolution was done in spite the theoretical model (1) was developed for cracks under pure mode I and for isotropic material. Comparing with the experimental results, the prediction works well only for low number of cycles because a more accurate calibration of the model must be done

in order to obtain a correct crack density prediction. However, the reliability of prediction model developed was verify through a comparison of the crack propagation rate with the experimental results finding almost a fully agreement.

The crack density trends obtained from the experimental tests were used to do a comparison with results of the project on tubular samples [$0_T/90_{ud,3}$] (2) that considers a global multiaxial stress state. This comparison could determine if the damage evolution is comparable between a local and a global multiaxial condition with the same biaxiality ratio. The results showed how a comparison in terms of crack density is not possible because of there are different constraint conditions on off-axis layers between flat and tubular samples that provide a different material strength and consequently a different damaging mode. Precisely, the off-axis layers of flat samples are probably characterized by the in-situ strength phenomenon through the 0° layers; this con dition could provide to increase the material strength and consequently to reduce the cracks initiation with respect to tubular samples where the in-situ strength is not present. Moreover, considering the Wohler's curve comparison between flat and tubular samples [$0_T/90_{ud,3}/0_T$], which have a constraint condition on the off-axis layers more similar to flat samples, it is possible to highlight again the increased material strength phenomenon in flat samples. These observations allowed to asserting that it is not possible to replicate the damage evolution under a global multiaxial condition through a local multiaxial condition considering tubular and flat samples respectively.

REFERENCES

1. **Hutchinson J.W., Suo Z.** *Mixed mode cracking in layered materials.* s.l. : Academic Press, 1992. Vol. 29.

2. **Marco, Piovesan.** Master thesis: Fatigue behaviour of composite tubes under multiaxial loading. s.l. : University of Padova, Italy, 2010.

3. Fatigue behaviour and life assessement of composite laminates under multiaxial loadings. **Quaresimin M., Susmel L., Talreja R.** s.l. : Int. J. Fatigue, 2010, Vol. 32, pp. 2-16.

4. *Off-axis fatigue crack growth and the associated energy relase rate in composite laminates.* **Tong J., Guild F.J., Ogin S.L., Smith P.A.** s.l. : Applied Composite Material, 1997, Vol. 4, pp. 349-359.

5. Fatigue behaviour of composite tubes under multiaxial loading. **M. Quaresimn, R. Talreja.**

6. **Ho S., Suo Z.** *Tunneling cracks in constrained layers.* s.l. : ASME, 1993. pp. 890-894. Vol. 60.

7. **AbaqusDocumentation.** http://127.0.0.1:2080/v6.9/books/usb/default.htm?startat=pt04ch11s04aus60.html#usb-anl-acontintegral. *http://127.0.0.1:2080/v6.9/.* [Online]

APPENDIX

DETERMINATION OF THE STEADY-STATE ENERGY RELEASE RATE THROUGH AN ABAQUS FINITE ELEMENTS SIMULATION

As reported in (6), considering a tunneling crack in a layer between two more stiff layers in Figure 0-1, if the external stress is sufficiently high it generates the propagation through the entire layer. The energy release rate, G_F, is different along the crack front point to point and depends on the crack length *a*. When the tunnel length reaches a value around few times the layer thickness, the crack propagates in a steady-state condition and crack front doesn't change its shape. In this condition we speak of steady-state energy release rate G_{ss}.

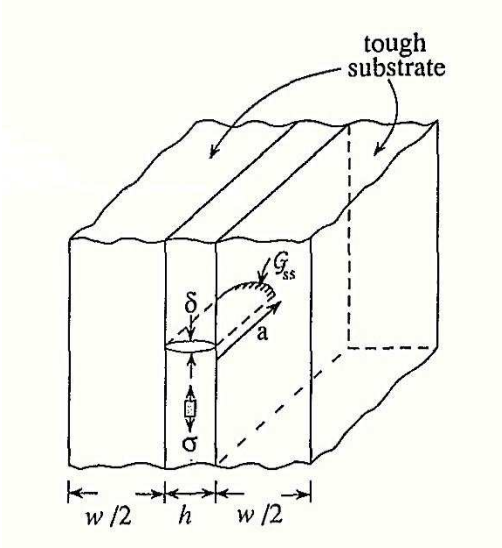

Figure 0-1. Tunneling crack in a constrained layer (6)

Basing on the ABAQUS Documentation (7), J-Integral is a parameter used in quasi-static fracture mechanics to determine the energy release rate associated with a crack growth. In fact, in a steady-state condition the two parameters correspond. As reported in Figure 0-2.

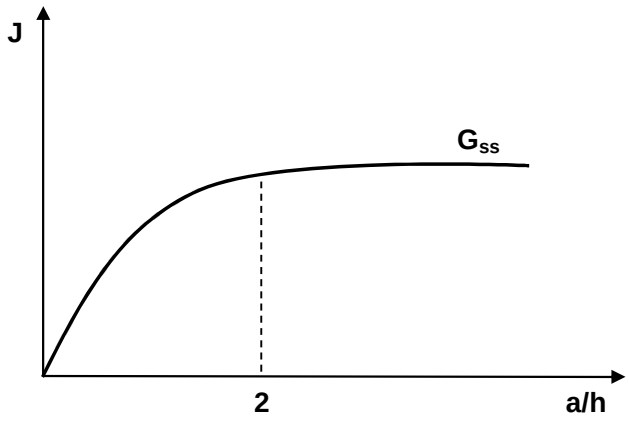

Figure 0-2. J-Integral trend by varying the crack length

J-integral is path independent so it doesn't vary in function to the considered direction respect to the crack tip. ABAQUS permit to calculate directly the J-Integral as an output results. In particular, it is based on a "contour integral evaluation" that generates a series of rings around the crack tip and through the crack front (in case of 3D modeling), after on each ring the solution is determine through an integral calculation. A representative images is reported in Figure 0-3.

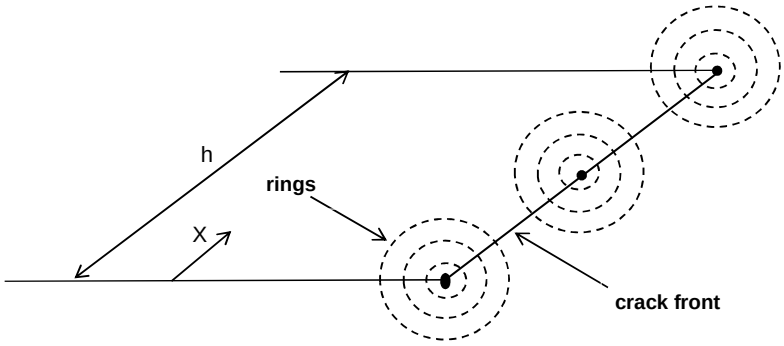

Figure 0-3. Contour Integral Evaluation of Abaqus

In the specific case of this project were defined 30 rings and 5 divisions along the crack front. A generically example of results obtained from ABAQUS model is in Figure 0-4.
For each group of rings the results converge to the final solution that is obviously approximated. This is due to intrinsic approximated nature of the finite element simulation and for this reason a very fine mesh around the crack tip is necessary. Considering the single convergent solution in every group it is possible to observe the curve that represents the J-Integral trend along the crack front. At this point it is necessary to consider the average value $\bar{J}$, that corresponds to the steady-state energy release rate.

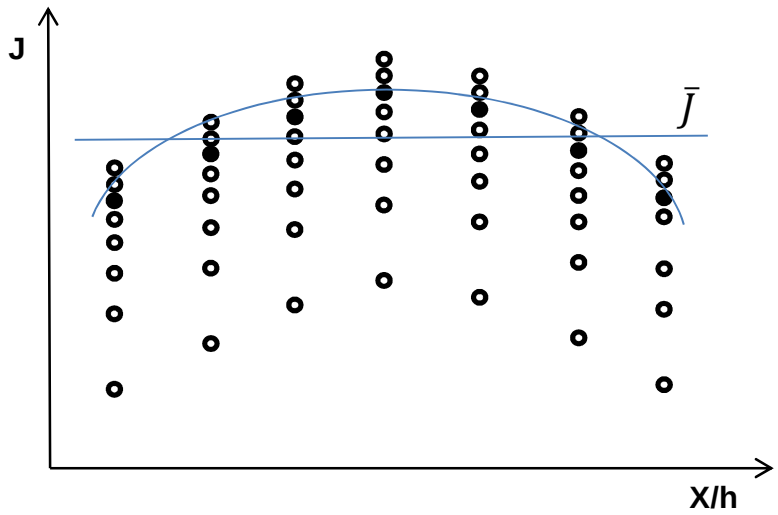

Figure 0-4. J-Integral trend along the crack front distinguishing the different rings groups